Review on water-hammer waves mechanical and theoretical foundations

Franck Plouraboué

Review on water-hammer waves mechanical and theoretical foundations

F. Plouraboué

Institut de Mécanique des Fluides de Toulouse, IMFT, Université de Toulouse, CNRS, Toulouse, France

Abstract

Water-hammer waves propagation is an important phenomenon arising in numerous applications. It is also a long-standing topic in the fields of mechanics, mechanical engineering and civil engineering. This review first presents the basic mechanism associated with water-hammer waves as well as a brief historical survey of the topic. It then develops along the twentieth century progress both regarding the Fluid-Structure-Interaction (FSI) influence and wave dissipation modeling. The second part of the review presents recent developments shading new lights on some aspects of the wave propagation with a fluid mechanical viewpoint. This review covers various aspects related to the influence of visco-elastic properties of the pipe's wall, asymptotic analysis as well as wave propagation within networks. Albeit discursive in many places, this review also tries to establish and derive many of the presented results from first principles, as well as emphasize the theoretical understanding of the topic.

Keywords: Water-hammer, Fluid–Structure–Interactions, acoustic waves in pipes, multiple time–scale analysis, asymptotic matching, dispersive waves, visco-elasticity, water hammer, blood hammer, Lamé–Clapeyron equations, wave propagation in networks, viscous dissipation, quantum graph

1. Introduction

1.1. Context of water-hammer wave

Water distribution networks, vascular system, irrigation networks, power-plant hydraulic circuits, geothermal extracting heat pipes, etc., are all complex hydraulic systems dedicated to flow distribution for their specific purpose. Within all these applications an incoming flow is needed to feed the needs. The incoming flow could be time-dependent so as to accommodate the possibly varying needs at various places, but the time-variation of the needs is not short compared to flow adaptation one. In other words, it is possible, in these systems to almost instantaneously adapt supply to demand. These systems are quasi-steady ones in normal use.

Nevertheless, if, for some reasons, either expected or not, a sudden change arises in the supply flow (whether due to pipe breakage, operational valve opening, heart valve closure, gate operation, incidental junction damage, etc..) then, a fast transient pressure wave is generated from it (Cf figure 1 for a real water-hammer wave signature inside a water distribution network). Since liquid incompressibility imposes flow conservation, any adjustment of a sudden flow change can only be due to compressible effects. Because liquids are much less compressible than gases, these sudden changes in fluid flow are much faster and much more intense in liquids than in gases even though also existing in the later. The less compressible the liquid, the faster the pressure wave having the highest amplitude. And since most liquids are very close to incompressible, the resulting pressure wave is very large in many cases, dramatic in some. This detrimental effect of water-hammer pressure waves has attracted interests in many applied areas in mechanical engineering and civil engineering [2, 3]. This is also why the first known scientists of the topic such as Résal [4], Michaud, [5], Korteweg [6], Joukowsky [7], belonged to the hydraulic's community. But this is only one part of the water-hammer story. Next section will provide much more details about the various modelling and analysis of it, but, since we believe the reader is, at this point, juvenile on the topic, we will pursue this discursive introduction by

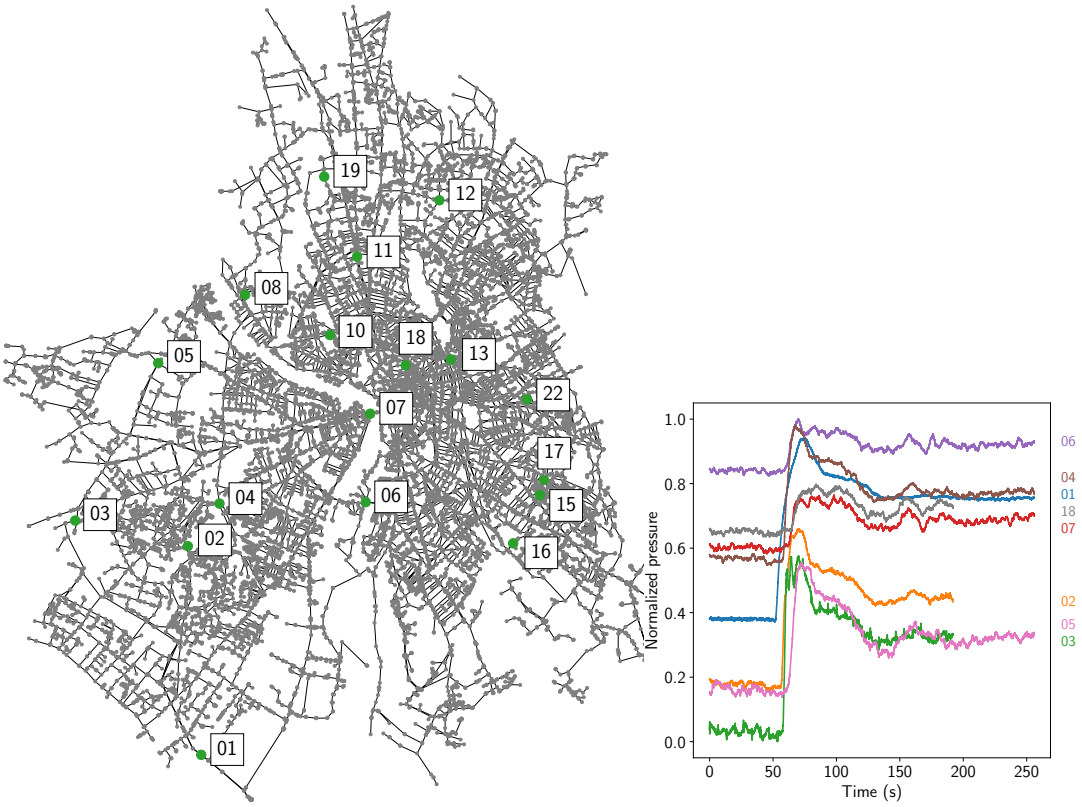

(a) (b)

Figure 1: (a) Illustration of a the water distribution network of Toulouse's town from [1] where pressure sensors have been distributed. (b) Water-hammer wave front passage signature at sensors placed in various locations.

some basic issues to introduce a second important aspect. As just mentioned, not only the pressure amplitude increases from the low compressibility of liquids. Also the wave's speed. In every fluid the isentropic compression law of fluid density variations ρ_f^* with fluid pressure P_f^* is given by $\partial\rho_f^*/\partial P_f^* = \rho_f^*/\mathcal{K}_f^*$. In the limit of infinite liquid bulk compressibility coefficient, i.e $\mathcal{K}_f^* \to \infty$, the incompressible limit, the water-hammer wave speeds goes to infinity. Nevertheless, this velocity cannot be infinite even for almost incompressible liquids. It is not necessary to invoke light's finite speed to avoid this inextinguishable sky, but another more down-to-earth fact that this pressure wave speed does not propagate freely into the liquid, being, on the contrary, confined within solid walls. Since the tube wall can expand —think of a blood vessel—, the pipe breathing resulting from the liquid over-pressure has a strong influence on the wave velocity propagation. Stress waves propagating within solids are known from a long-time to result from its elastic deformation. For pressure waves associated with compressive density waves inside one material, the speed is proportional to the elastic Young modulus. The harder the solid, the faster its compressive wave. Split-Hopkinson pressure tests are indeed using this effect to deduce the material property from the wave-speed measurement [8, 9]. Going back to the water-hammer pressure wave, since it is confined within solid walls, it can not move freely in the transverse direction of its propagation. The wave's pressure is indeed deforming the solid walls. This results in a coupling between the liquid pressure wave, and the solid one. This is the second key aspect of the water-hammer waves : they result from a Fluid-Structure Interaction (FSI) between the acoustic wave propagating within the fluid bulk and the elastic deformation of the solid surrounding the liquid. Furthermore, and not intuitively, FSI produces a double effect on water-hammer waves: first, as already mentioned, the propagating speed of the liquid pressure wave both depends on the liquid isentropic bulk modulus, i.e the compressibility coefficient of the fluid and the Young modulus of the solid. More precisely, on the ratio of both. Second, this water-hammer wave train hides another : a solid compressive elastic wave. Because it is faster in most cases, this secondary wave comes first,

and has been called the precursive wave [10, 11]. In some applications such as water distribution networks, and many other hydraulic contexts, this elastic wave is disregarded for being of small influence. This generally results from anchored mechanical conditions preventing the free-motion of the external solid wall (cemented, buried, or fit-in) weakening the elastic wave contribution. This is why most hydraulic modeling of water-hammer do not consider the coupled elastic wave. However, this coupling is very important when the solid walls are soft (e.g vascular system), when the conducts are free to move (e.g suspended), or when the solid walls are very thin.

Having now set the scene of the two main mechanical effects rooting water-hammer, i.e liquid compressibility and FSI, it is now appropriate to provide an historical survey of how modern understanding has emerged. Nevertheless before this, it is important to mention that various interesting reviews have previously discussed water-hammer [12, 13, 14, 15, 16, 17, 18]. Among those [12, 15] have focused their review on FSI aspects in simple pipes configurations. [14] has more focussed its interest into the historical perspective of the topic. On the other hand [13, 16] discuss hydraulic applications where FSI effects are generally neglected, whilst concentrating on water distribution networks purposes. [18]'s review consider more specifically blood-hammer within the arterial system whereby issues related to the visco-elastic response of arteries are deepened. Finally, it is important to stress what material is covered by this review and the about-face. This review focuses on water-hammer wave propagation surrounded by possibly complex solids including visco-elastic ones. This topic is of major practical relevance, since water-hammer waves are strongly dependent on the solid visco-elastic response, because these solids are encountered in many contexts. Concerning the fluid, this review considers water-hammer waves arising inside Newtonian compressive liquids, including viscous effects in the fluid. Nevertheless this review will not cover several aspects of water-hammer : cavitation [19], water-hammer in non-Newtonian liquids (e.g [20]), condensation-induced water-hammer (e.g [21]), thermally coupled water-hammer waves (e.g [22]), arc-discharge induced water hammer (e.g. [23]). Also, this review is not

going to discuss transient-based defect detection and water-hammer use for inverse problems which have been vivid areas of investigations over the last fifteen years, but deserve a review on their own. However it covers (some aspects) of water-hammer wave propagation in complex pipe networks. The specificity of this review, is to focus on water-hammer's mechanics, so as to emphasize how modern understanding can help in modeling simplification, concepts generality, and also, questioning and/or revisiting practical use. This review does not have the ambition to be exhaustive in every aspect, reflecting that the author's best knowledge of the topic is unfortunately neither objective nor complete. It also reflects the author's subjective interests on the topic, oriented toward future research directions dedicated toward tackling and simplifying various aspects of water-hammer complexity.

This review is organized as follows. Section (1.2) provides a brief historical description of the first understanding and modelling attempts of water-hammer.

Section (2) then provides a summary of the twentieth's century progress on the topic. Albeit discursive, this section also tries to establish many of the presented results from first principles.

The two following sections are devoted to the review of more modern issues. Section 3 is mostly concerned about modeling the influence of pipe's visco-elastic behavior onto the water hammer wave.

Section (4) develops on the twenty first century advances in the field. It covers both time and spatial asymptotic analysis, giving new perspective to the underlying understanding of yet unsolved water-hammer's specific aspects. Furthermore section (4) also covers recent modern issues associated with theoretical developments for water-hammer wave propagation within networks.

1.2. A brief historical survey of first water-hammer understanding

As previously mentioned the water-hammer research started from engineering concerns and viewpoints, at the end of the nineteenth century. The first noteworthy contribution can be credited to L. Menabrea [24] reporting the joint influence of fluid bulk modulus $\mathcal{K}_f^*$, and the solid wall Young's modulus E^*

in water-hammer waves. Thereafter Michaud [5] developed some protection devices guidelines for hydraulic systems. He focused his interest on plans for safety valves and water-hammer balloons but meanwhile, derives one of the first expressions for the propagation speed of water hammer waves, c_p^* (in the following all p subscript on all subsequent c_p^* velocities refers to "pulsed" wave speeds, not to be confused with possibly pipe's one; this pulse wave speed is a bulk liquid pressure wave), the same year as Korteweg [6]. Considering the solid wall as a successive axially independent concentric elastic rings, these authors found that

$$c_{p,K}^* = \frac{c_0^*}{\sqrt{1+\frac{2\mathcal{K}_f^*}{\alpha E^*}}}, \text{ with } \mathrm{c}_0^{*2} = \frac{\mathcal{K}_\mathrm{f}^*}{\rho_\mathrm{f}^*}, \tag{1}$$

c_0^* being the sound speed in the liquid bulk, $\alpha = e^*/R_0^*$ the dimensionless pipe wall thickness associated with solid tickness e^* having inner radius R_0^* and ρ_f^* the fluid density ($*$'s quantities are dimensional in the following, whilst on the contrary, dimensionless quantities do not have $*$). The approximate theory (1) brings out for the first time the cornerstone contribution of the liquid's bulk modulus to Young modulus ratio, i.e. ${\mathcal{K}_f}^*/E^*$, into water-hammer wave c_p^*. Since (1)'s denominator is larger than unity, the water-hammer wave speed is lower than the sound speed in bulk liquid c_0^*, as expected from the energy transfer of the wave into solid elastic deformation.

It is interesting to discuss the comparison of Korteweg and Michaud prediction with their contemporary Résal [4] who proposed a simpler expression for this velocity being based upon the wall's elastic wave speed $\sqrt{\alpha E^*/2\rho_f^*}$. As discussed in [19, 25] reorganizing (1) leads to

$$\frac{1}{c_{p,K}^{*2}} = \frac{1}{c_0^{*2}} + \frac{2\rho_f^*}{\alpha E^*}. \tag{2}$$

Result (2) can be interpreted as equivalent resistance of parallel electrical circuits or in a more mechanical frame, the equivalent stiffness of two sucessive springs. Korteweg's [6] wave velocity is the equivalent wave speed of the liquid bulk sound speed c_0^*, in parallel with the elastic wave speed $\sqrt{\alpha E^*/2\rho_f^*}$ (this point is discussed in more details in [25]). As mentioned in the introduction not

only the wave speed, but also the pressure amplitude is of major engineering importance. Few years after Korteweg, Joukowsky [7] focused on the mass equilibrium occurring during a transient event, so as to find the maximal reachable over pressure ΔP^*, which is related to the longitudinal velocity variation ΔW^* associated with the flow sudden change $\Delta Q^* = S^* \Delta W^*$ (in the following W_0^* will denote the steady-state reference velocity and ΔW^* will be considered as an order-one fraction of W_0^*)

$$\Delta P^* = \rho_f^* c_p^* \Delta W^*. \tag{3}$$

This fundamental relationship permits to improve the security design efficiency of water plants. The derivation of (3) is now discussed. Let us consider the mass

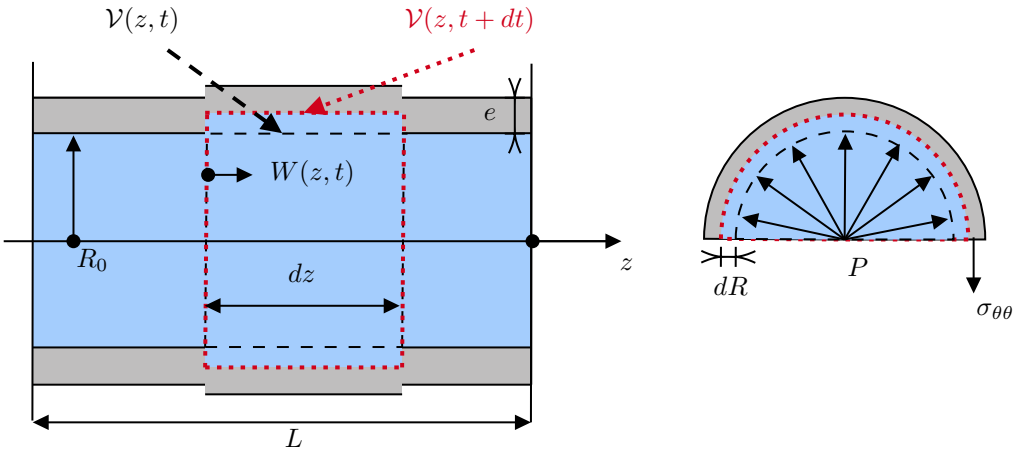

Figure 2: Fluid mass conservation during a hydraulic transient

balance in the elementary volume $\mathcal{V}^*$, having external surface S^*, as defined in Figure 2

$$\partial_{t^*}\left(\rho_f^* S^*\right) + \partial_{z^*}\left(\rho_f^* S^* W^*\right) = 0, \tag{4}$$

Introducing Lagrangian derivative $d/dt^* \equiv \partial_{t^*} + W^* \partial_{z^*}$, (4) can be decomposed into three terms

$$\underbrace{\frac{1}{\rho_f^*}\frac{d\rho_f^*}{dt^*}}_{\text{Liquid compression}} + \underbrace{\frac{1}{S^*}\frac{dS^*}{dt^*}}_{\text{Pipe dilatation}} + \underbrace{\partial_{z^*} W^*}_{\text{Velocity gradient}} = 0. \tag{5}$$

Using the previously mentioned isentropic compression law, the fluid density gradient are related to pressure ones

$$\frac{1}{\rho_f^*}\frac{d\rho_f^*}{dt^*} = \frac{1}{\mathcal{K}_f^*}\frac{dP^*}{dt^*}. \tag{6}$$

The pipe dilatation term of (5) requires a little more inspection. It is related to what is called the *pipe breathing phenomenon*, i.e the deformation arising when an axi-symmetric pressure wave propagates into a cylindrical solid, deforming it radially and longitudinally whilst preserving the axi-symmetry. Considering the instantaneous elastic solid response of the azymuthal normal stress, i.e the hoop stress $\sigma_{\theta\theta}^*$, integrated along one pipe's mid-plane section having normal direction $\mathbf{e}_\theta$ and longitudinal length L^*, provides a contribution into the solid region only, whose thickness is e^*, so that a an elastic force $2L^*e^*\sigma_{\theta\theta}^*$ is built to balance the fluid pressure P^* integrated along the same pipe's mid-plane section $2R_0^*L^*P^*$, so that

$$\sigma_{\theta\theta}^* = \frac{R_0^*}{e^*}P^* = \frac{1}{\alpha}P^*. \tag{7}$$

Furthermore, from elasticity theory, the relative strain of the pipe is proportional to its stress such that

$$d\sigma_{\theta\theta}^* = E^*\frac{dR^*}{R^*}. \tag{8}$$

From (7) in (8) and since, $S^* = \pi R^{*2}$, one finds

$$\frac{1}{S^*}\frac{dS^*}{dt^*} = \frac{2}{\alpha E^*}\frac{dP^*}{dt^*}. \tag{9}$$

Finally, combining (6), (9) and (5), yields to the following mass conservation equation

$$\frac{1}{\rho_f^*}\frac{dP^*}{dt^*} + \frac{c_0^{*2}}{1+\frac{2\mathcal{K}_f^*}{\alpha E^*}}\partial_{z^*}W^* = \frac{1}{\rho_f^*}\frac{dP^*}{dt^*} + c_{p,K}^{*2}\partial_{z^*}W^* = 0, \tag{10}$$

consistently with (1) found by [6]. It is also important to stress that (10) leads to the Joukowsky's scaling (3) for the pressure [7].

Although sufficient for many engineering applications, these theoretical outlines remain too limited in scope as they do not provide an in-depth comprehensive understanding of hydraulic transients. The relation (8) highlights the

weaknesses of these early models. The solid rheology is highly simplified which results in a degraded representation of shear and strain distribution in the pipe (which however might turn-out to be enough for some engineering issues). Furthermore, the fluid is supposed inviscid and the long-time dynamics of the pressure trend thereby remains unknown. This is why this simplified picture has been dramatically improved during the twentieth's century.

2. Water hammer : a dual phenomenon intertwined with three couplings

This section now presents the modern view of water-hammer progressively emerging from 20^{th} century developments. This view is very synthetically presented in [19, 25] resulting from the infusion of many previous studies as also discussed in [26] from which this section is inspired. Numerous deep analysis of great theoretical mechanics have progressively permit to understand that various fundamental mechanisms were acting together, on the water-hammer wave, in a subtle way. Moreover, and surprisingly enough, as the complexity increased, the ability to synthetically produce analytical results also permitted a more compact and clear presentation of the phenomenon to simplify its theoretical understanding. This back-and-forth (hopefully creative) competition between tackling complexity and idealistic simplification is still present at the fore-front of the phenomenon's understanding, as discussed in Section 4 References [19, 25] discuss how, resulting from both compressibility and FSI effects, the water-hammer wave is influenced by by three, possibly intertwined, couplings:

- *Poisson's coupling* which refers to solid axial vibrations arising from radial ones. These couplings depend on the mechanical properties of the solid, as well as on the possibly complex vibrating modes (flexural, torsional, etc...). It is thus related to the possibly complex solid response to the fluid pressure wave.

- *Junction couplings* which refers to pipe's ends couplings either resulting from connections with other pipes, or to boundary conditions imposed at pipe's end. This effect thus results in the boundary conditions influence on the propagating waves and selected modes.

- *Friction couplings* which refers to the shear stress couplings between the fluid and the solid, i.e. the viscous friction coupling, and between the solid and the surrounding medium, e.g. dry Coulomb's friction if the pipe is buried.

According to [27], Poisson and junction couplings are shaping the system's dynamics, i.e. determine the selected wave's modes as well as their structure, whilst friction couplings induce wave's attenuation due to energetic losses. Furthermore, from a mechanical viewpoint, any pipe's degree of freedom is expected to interact with the fluid dynamics, generating non-trivial additional couplings, [27]. We now detail each coupling in the forthcoming sections.

2.1. Poisson coupling and Fluid Structure Interaction (FSI) analysis

FSI describes couplings occurring in liquid-filled pipe systems. Let us first consider an homogeneous, elastic and isotropic pipe having density ρ_s^*. Let us denote the radial displacement ξ^* and axial one ζ^*, being the two components of the displacement vector $\boldsymbol{\xi}^* = (\xi^*, \zeta^*)$ —the only relevant ones for axisymmetric pipe breathing mode of deformation—, related to the strain tensor $\boldsymbol{\epsilon}^* = 1/2(\boldsymbol{\nabla}\boldsymbol{\xi}^* + \boldsymbol{\nabla}\boldsymbol{\xi}^{*T})$.

One of the first major contribution to pressure wave propagation studies in pipes taking into account (FSI) can be attributed to [28]. Lamb extends [6]'s work from taking into account the Poisson's coupling effect. Based on the second Newton's law for the solid equilibrium, and a radial dependent pressure

198 wave for the fluid, he found

$$\underbrace{\rho_s^* e^* \partial_{t^*}^2 \zeta^*}_{\text{Axial inertia}} = \underbrace{\frac{\alpha E^*}{1-\nu_s^2}\left(\nu_s \partial_{z^*}\xi^* + R_0^* \partial_{z^*}^2 \zeta^*\right)}_{\text{Axial tension}}, \tag{11}$$

$$\underbrace{\rho_s^* e^* \partial_{t^*}^2 \xi^*}_{\text{Radial inertia}} = -\underbrace{\frac{\alpha E^*}{1-\nu_s^2}\left(\frac{\xi^*}{R_0^*} + \nu_s \partial_{z*}\zeta^*\right)}_{\text{Radial tension}} + \underbrace{P^*}_{\text{Dynamic loading}}, \tag{12}$$

$$\partial_{t^*}^2 P = c_0^{*2}\left(\partial_{z*}^2 + \frac{\partial_{r^*}}{r^*}\left(r^* \partial_{r^*}\right)\right) P^*. \tag{13}$$

Under plane-wave long-wavelength framework assumption, Sr. H. Lamb determines the radial pressure variations from radial Bessel function. Furthermore, ensuring the kinematic continuity conditions at the pipe's inner wall, he spells out a cubic (in c^{*2}) dispersion relation for the wave speeds

$$\frac{c^{*2}-c_0^{*2}}{c_0^{*2}} \underbrace{\left[c^{*4} - \left(1 + \frac{\lambda^{*2}}{4\pi^2 R_0^{*2}}\right)\frac{E^*}{\rho_s^*\left(1-\nu_s^2\right)}c^{*2} + \frac{\left(1-\nu_s^2\right)\lambda^{*2}}{4\pi^2 R_0^{*2}}\left(\frac{E^*}{\rho_s\left(1-\nu_s^2\right)}\right)^2\right]}_{\text{Dispersion eq. for } P=0 \text{ in (12)}}$$
$$- \frac{2\mathcal{D}}{\alpha}\frac{\lambda^{*2}c^{*2}}{4\pi^2 R_0^{*2}}\left(c^{*2} - \frac{E^*}{\rho_s^*\left(1-\nu_s^2\right)}\right) = 0, \tag{14}$$

with the density ratio

$$\mathcal{D} = \frac{\rho_f^*}{\rho_s^*}, \tag{15}$$

λ^* being the wavelength. The cubic structure of the dispersion relation thus provides a set of three modes of propagation, being in increased order of frequency (decreasing order of wavelength) comparable to corrections upon the fluid wave speed, solid axial wave speed and solid radial wave speed, respectively. Under the long wavelength hypothesis framework, i.e. $\lambda^*/R_0^* \gg 1$, an important set of results can be found. If the dynamic loading term is neglected in (12), i.e. if P^* is set to zero, Lamb derives the compressible axial solid wave speed (Cf. terms in brackets in (14))

$$c_s^{*2} = \frac{E^*}{\rho_s^*}, \text{ (Hyp: } P* = 0). \tag{16}$$

Furthermore, if the solid instantaneously responds to the fluid dynamic load, i.e. neglecting time derivatives in (11)-(12), Lamb proves that his theory leads

to [6]'s one (Cf. (1)) so that no proper (FSI) occurs then

$$c^{*2}_{p,Lamb} = c^{*2}_{p,K} \quad , \text{(Hyp: } \partial^2_{t^*}\boldsymbol{\xi}^* = \mathbf{0}\text{)}. \tag{17}$$

If one considers a highly deformable tube, i.e. $\mathcal{K}^*_f \gg E^*$, Lamb's theory merges with the [4]'s one (Cf. (2))

$$c^{*2}_{p,Lamb} = \frac{\alpha E^*}{2\rho^*_f} \text{ , and, } c^{*2}_{s,Lamb} = \frac{E^*}{\rho^*_s\left(1-\nu^2_s\right)} \text{ , (Hyp: } \mathcal{K}^*_f \gg E^*\text{)}. \tag{18}$$

Finally, Taylor-expanding the dispersion relation (14) with respect to the radius per wavelength ratio, i.e. R^*_0/λ^* –long-wavelength asymptotic limit— H. Lamb finds an analytical formulation for the fluid and axial solid wave speed corrections due to FSI

$$c^{*2}_{\pm,Lamb} = \frac{1}{2}\left[\bar{c}^{*2}_{Lamb} \pm \sqrt{\bar{c}^{*4}_{Lamb} - \frac{4\left(c^*_0 c^*_s\right)^2}{1+\frac{2(1-\nu^2_s)\mathcal{K}^*_f}{\alpha E^*}}}\right], \tag{19}$$

$$\bar{c}^{*2}_{Lamb} = \frac{c^{*2}_s + c^{*2}_0\left(1+\frac{2\mathcal{D}}{\alpha}\right)}{1+\frac{2(1-\nu^2_s)\mathcal{K}^*_f}{\alpha E^*}}, \tag{20}$$

where the negative mode c^*_- holds for the fluid wave speed correction, whilst the positive mode c^*_+ stands for the axial solid wave speed correction one. Half a century later [10, 11] extends the brilliant contribution of [28]. In a sterling paper, Skalak derives an in-depth analysis of the coupling mechanisms occurring between an elastic shell pipe and the liquid. He considers both rotatory radial inertia and the bending moment of the solid. Skalak's shell model (hereby slightly re-organized) reads as follows, [29, 30]

$$\underbrace{\rho^*_s e^* \partial^2_{t^*}\zeta^*}_{\text{Axial inertia}} = \underbrace{\frac{\alpha E^*}{1-\nu^2_s}\left(\nu_s \partial_{z^*}\xi^* + R^*_0 \partial^2_{z^*}\zeta^*\right)}_{\text{[28]'s axial tension}} - \underbrace{\frac{\alpha e^{*2} E^*}{12\left(1-\nu^2_s\right)}\partial^3_{z^*}\xi^*}_{\text{Bending axial tension}}, \tag{21}$$

and

$$\underbrace{\rho^*_s e^* \partial^2_{t^*}\xi^*}_{\text{Radial inertia}} - \underbrace{\frac{\rho^*_s e^{*3}}{12}\partial^2_{z^*}\partial^2_{t^*}\xi^*}_{\text{Rotatory inertia}} = -\underbrace{\frac{\alpha E^*}{1-\nu^2_s}\left[\left(1+\frac{\alpha^2}{12}\right)\frac{\xi^*}{R^*_0} + \nu_s \partial_{z^*}\zeta^*\right]}_{\text{[28]'s modified radial tension}} \tag{22}$$

The continuity conditions at the fluid solid interface were ensured and Skalak overcomes the system resolution by performing a conjugate Fourier (upon space) and Laplace (upon time) analysis. The in-depth investigations of the radial solid displacement field reveals a discrete infinite set of resonance frequencies governed by a transcendental equation. As in [28], [10, 11] then analyzes the solution in the long-wavelength asymptotic limit, i.e. when frequency goes to zero. In this limit, two propagating modes remain and: "*a physical interpretation [...] is that only these two lowest modes have finite phase velocities as the wavelength increases indefinitely.* The two wave speeds, in the infinite wavelength framework, then converges toward the [28]'s one

$$\lim_{\lambda\to\infty} c^{*2}_{\pm,Sk} \equiv c^{*2}_{\pm,Lamb}. \tag{23}$$

R. Skalak [10, 11] is nevertheless the first to mention the "*precursor wave*" associated with the axial pipe dynamics, although the used of shell approximation remained a limitation for practical analysis. Whereas it turns out that the precursor wave prediction was indeed a robust prediction out of the shell approximation context, Skalak's model also neglects the wave speed dispersion arising from radial inertia. R. Skalak achieved the first known derivation of (FSI) four-equations of liquid-filled water-hammer

$$\frac{1}{\mathcal{K}^*_f}\partial_{t^*}P^* + \partial_{z^*}W^* = -\frac{2}{R^*_0}\partial_{t^*}\xi^*, \tag{24}$$

$$\rho^*_f\partial_{t^*}W^* + \partial_{z^*}P^* = 0, \tag{25}$$

$$\underbrace{\rho^*_s e^*\partial^2_{t^*}\zeta^*}_{\text{Axial inertia}} = \underbrace{\frac{\alpha E^*}{1-\nu_s^2}\left(\nu_s\partial_{z^*}\xi^* + R^*_0\partial^2_{z^*}\zeta^*\right)}_{\text{[28]'s axial tension}} \tag{26}$$

$$\underbrace{\frac{\alpha E^*}{1-\nu_s^2}\left[\frac{\xi^*}{R^*_0} + \nu_s\partial_{z^*}\zeta^*\right]}_{\text{[28]'s radial tension}} = P^*, \tag{27}$$

The r.h.s of (24) results from kinematic boundary conditions associated with the solid wall motion influence. It can be derived from Reynolds transport theorem, as discussed in [13, 18] and mentioned in [31] that we now detail. Consider a domain $\Omega(t)$, having boundary $\partial\Omega(t)$. Inside $\Omega(t)$ any field $\mathbf{\Psi}$ (scalar, vector,

tensor) fulfills Reynolds transport theorem

$$\frac{d}{dt}\int_{\Omega(t)} \mathbf{\Psi} d\Omega = \int_{\Omega(t)} \frac{\partial \mathbf{\Psi}}{\partial t} d\Omega + \int_{\partial\Omega(t)} \mathbf{\Psi} v_n d\partial\Omega, \tag{28}$$

v_n is the outer-normal velocity of the boundary $\partial\Omega(t)$ motion. This equality can also be rewritten in a usefull way with the use of the divergence theorem on the last term of (28) so that

$$\frac{d}{dt}\int_{\Omega(t)} \mathbf{\Psi} d\Omega = \int_{\Omega(t)} \left(\frac{\partial \mathbf{\Psi}}{\partial t} + \nabla \cdot (\mathbf{\Psi} \boldsymbol{v}) \right) d\Omega = \int_{\Omega(t)} \left(\frac{d\mathbf{\Psi}}{dt} + \mathbf{\Psi} \nabla \cdot \boldsymbol{v} \right) d\Omega \tag{29}$$

When considering the domain $\Omega(t)$ as the pipe section $S^*(t)$ whose boundary is the moving circle $\mathcal{C}^*(t)$ having radius R^*, and considering the unit scalar $\mathbf{\Psi} = 1$, then (28), associated with the kinematic boundary condition $u_n = \partial\xi^*/\partial t$ leads to

$$\frac{d}{dt} S^*(t) = \int_{\mathcal{C}^*(t)} \frac{\partial \xi^*}{\partial t} d\mathcal{C} = 2\pi R^* \frac{\partial \xi^*}{\partial t}, \tag{30}$$

Using (30) in (5) whilst using (9) leads to (24).

These coupled first-order hyperbolic (FSI) four-equations receive a more compact formulation in the form of two coupled propagating waves operators

$$\left[\partial^2_{t^*} - \begin{pmatrix} c^{*2}_{p,Sk} & 0 \\ 0 & c^{*2}_s \end{pmatrix} \partial^2_{z^*} - \begin{pmatrix} 0 & 2\nu_s \rho^*_f c^{*2}_{p,Sk} \\ \frac{\nu_s c^2_s}{\alpha E^*} & 0 \end{pmatrix} \partial_{z^*} \partial_{t^*} \right] \begin{pmatrix} P^* \\ \partial_{t^*} \zeta^* \end{pmatrix} = \mathbf{0}, \tag{31}$$

with

$$c^{*2}_{p,Sk} = \frac{c^{*2}_0}{1 + \frac{2\mathcal{K}^*_f (1-\nu^2_s)}{\alpha E^*}}. \tag{32}$$

Two years after, [32] followed up [10, 11]'s analysis by (i) integrating the transverse shear force contribution in the radial solid momentum conservation (27) (ii) considering the azymutal displacement. Using the same long-wavelength approximation framework, they also carried out a frequency-domain analysis and converged toward [28] and [10, 11] results. Although precursor waves have been theoretically predicted for a long time, there were experimentally confirmed in 1969 only [33] for elastic steel (aluminum alloyed) and visco-elastic (PE) pipes by Thorley. Whilst the predictive trend for the wave propagation speeds was inconclusive for visco-elastic materials, the order of magnitude for elastic solids

was consistent. Thorley attributed these discrepancies to the temperature sensitivity of visco-elastic rheology as illustrated in Figure 3. [34] carried out a

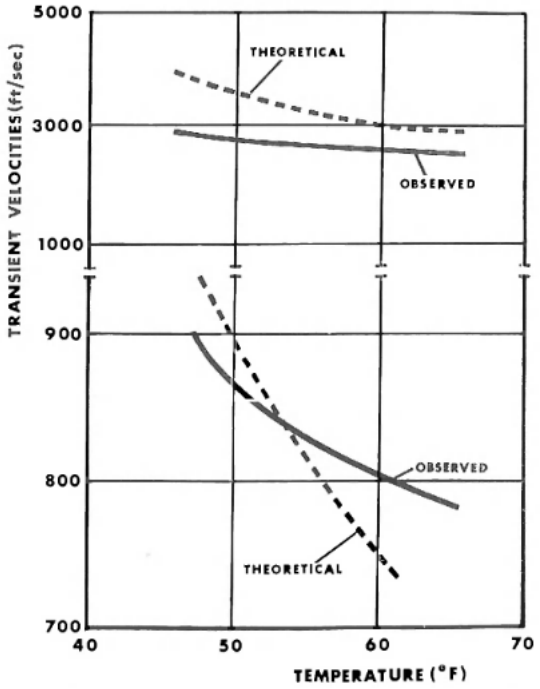

Figure 3: Experimental results of [33]. The upper curve represents the investigated elastic material whilst the lower curve holds for the visco-elastic material.

complete study extending the analysis of [32] to viscous fluid. The kinematic continuity conditions at the pipe's wall were spelled out and ensured, whilst the set of constitutive equations was analyzed under the scope of the plane wave framework. The authors then concluded that the: "'*frequency dependence of the zeroth mode phase velocity is primarily a result of the tube constraint at high frequencies and viscosity at low frequencies.*" Finally, [34] were able to propose an order of magnitude estimate for the transverse solid shear force, i.e $(\mathcal{D}/\alpha)\left(c_0^*/c_s^*\right)^2 \tau_w^*$ proportional to the fluid wall shear-stress τ_w. [35] carried out experimental tests similar to those of [33] on polymer materials (ABS, PVC) and steel for flexible and rigid configurations, i.e. unstressed and axially stressed pipes. Despite Thorley encountered difficulties in discarding the

effects of the junction coupling arising from his downstream solenoid valve, he clearly observed and identified the presence of precursor perturbations resulting from Poisson's coupling. [35] further noted: "*that mechanical damping can be more important for water-hammer decay than viscous friction*". This remark is meaningful when the radial inertia of the pipe is preponderant or when the rheology is inelastic, as is the case for visco-elastic materials. [36, 37] delivered a complete work emphasizing the previous contributions from [28] to [38]. The authors

considered the rigid, elastic and visco-elastic behavior of a pipe together with the viscous, or inviscid, behavior of the fluid. Their pipe model furthermore accounts for the radial thickness influence. [36, 37] derive a complete set of dispersion relations and studied the frequency dependence of the propagation wave speeds.

[39, 40, 41] carried out an outstanding and complete analysis within solid's shell approximation taking into account thermal and fluid viscosity effects.

The work of [41] provides a comprehensive overview of the main models, assumptions and results of the early researches on hydraulic transients in pipes. For the solid, the momentum conservation equation is integrated in the radial direction leading to an axial dependent problem, whilst the bending effects were neglected. [19]'s analysis is a breakthrough in the liquid-filled pipe research area. A. Tijsseling combined both the Navier-Stokes equations, averaged over the pipe's section, with the solid momentum conservation equations (also called Lamé-Clapeyron equations, [42]) to derive a set of four-(FSI) hyperbolic equations [19]

$$\left[\begin{pmatrix} \frac{c_0^{*2}}{\mathcal{K}_f^* c_{p,T}^{2*}} + \frac{4\nu_s^2}{\alpha(2+\alpha)E^*} & 0 \\ 0 & 1 \end{pmatrix} \partial_{t^*} + \begin{pmatrix} 0 & 1 \\ \frac{1}{\rho_f^*} & 0 \end{pmatrix} \partial_{z^*}\right] \begin{pmatrix} P^* \\ W^* \end{pmatrix} = \frac{2\nu_s}{E^*} \begin{pmatrix} \partial_{t^*}\sigma_{zz}^* \\ 0 \end{pmatrix} - \begin{pmatrix} 0 \\ \frac{2\tau_w^*}{\rho_f^* R_0^*} \end{pmatrix}, \tag{33}$$

$$\left[\partial_{t^*} - \begin{pmatrix} 0 & E^* \\ \frac{1}{\rho_s^*} & 0 \end{pmatrix} \partial_{z^*}\right] \begin{pmatrix} \sigma_{zz}^* \\ \dot{\zeta}^* \end{pmatrix} = \frac{2\nu_s}{\alpha(2+\alpha)} \begin{pmatrix} \partial_{t^*} P^* \\ 0 \end{pmatrix} + \begin{pmatrix} 0 \\ \frac{2\tau_w^*}{\rho_s^* e^*(2+\alpha)} \end{pmatrix} \tag{34}$$

with $\dot{\zeta}^* = \partial_{t^*}\zeta^*$ the longitudinal solid velocity and

$$c_{p,T}^{*2} = \frac{c_0^{*2}}{1 + \frac{2\mathcal{K}_f^*}{\alpha E^*}\left(\frac{2(1-\nu_s^2)}{2+\alpha} + \alpha(1+\nu_s)\right)}. \tag{35}$$

As in [28, 10, 32] a set of two coupled wave speeds can be found from (33)-(34)

$$c_{\pm,T}^{*2} = \frac{1}{2}\left[\bar{c}_T^{*2} \pm \sqrt{\bar{c}_T^{*4} - 4c_s^{*2}c_{p,T}^{*2}}\right], \quad \text{with} \quad \bar{c}_{\mathrm{T}}^{*2} = c_{\mathrm{s}}^{*2} + \left(1 + \frac{4\nu_{\mathrm{s}}^2\mathcal{D}}{\alpha\,(2+\alpha)}\right) c_{\mathrm{p,T}}^{*2}. \tag{36}$$

The last term of the (33)'s r.h.s involves a dissipative (a sink term) associated with the wall shear-rate τ_w^* the derivation of which can again be obtained using the Reynolds transport theorem as further discussed in Section 2.3. An undamped simplified derivation of (33)-(34) neglecting wall shear rate τ_w^*, thus neglecting dissipation, can also be found in [43]. Further information on the development of liquid-filled pipe models during the 20^{th} century can also be gathered from the review of [12]. As also discussed in many places [12, 41, 18, 13] the influence of a body force (e.g gravity) can easily be added into those FSI four-equations. The wave speeds and the corresponding corrective coupled wave speeds, are depicted in Figure 4. The Skalak's pulse wave speed model converges, in the limit α tends to one, to the D. Korteweg's one, whilst as expected, the A.S. Tijsseling's model differs for thick tubes (Cf. Fig. 4a&4b). In addition, for very thin pipes, the models strongly differ in the prediction of the coupled wave speeds as depicted in Figure 4d. To provide the pressure dynamic predictions the four-(FSI) equations system (33)-(34) nevertheless requires a closure wall shear stress model for τ_w^* [44]. This necessitates a rather developed discussion which is postponed to section 2.3. Un-damped wave propagation, is nevertheless interesting to compute considering $\tau_w^* = 0$ in the coupled hyperbolic problems (33)-(34) which is strongly dependent on boundary conditions, an issue related to *junction coupling* which is now considered.

2.2. Junction coupling

2.2.1. Junction coupling within simple domains

This section first considers the simple pipe's configurations and later-on discuss more complex ones, such as networks. Coupled FSI propagative hyperbolic problems are determined by their boundary conditions. Within simple configurations, since these boundary conditions might differ, it is possible to propagate one formal, yet un-determined solution —satisfying one of the boundary conditions— to the other additional boundary conditions. This is how transfer function matrices are used in free oscillation theory. It is also the way Transfer Matrix Method (TMM) handles the influence of boundary conditions. One ad-

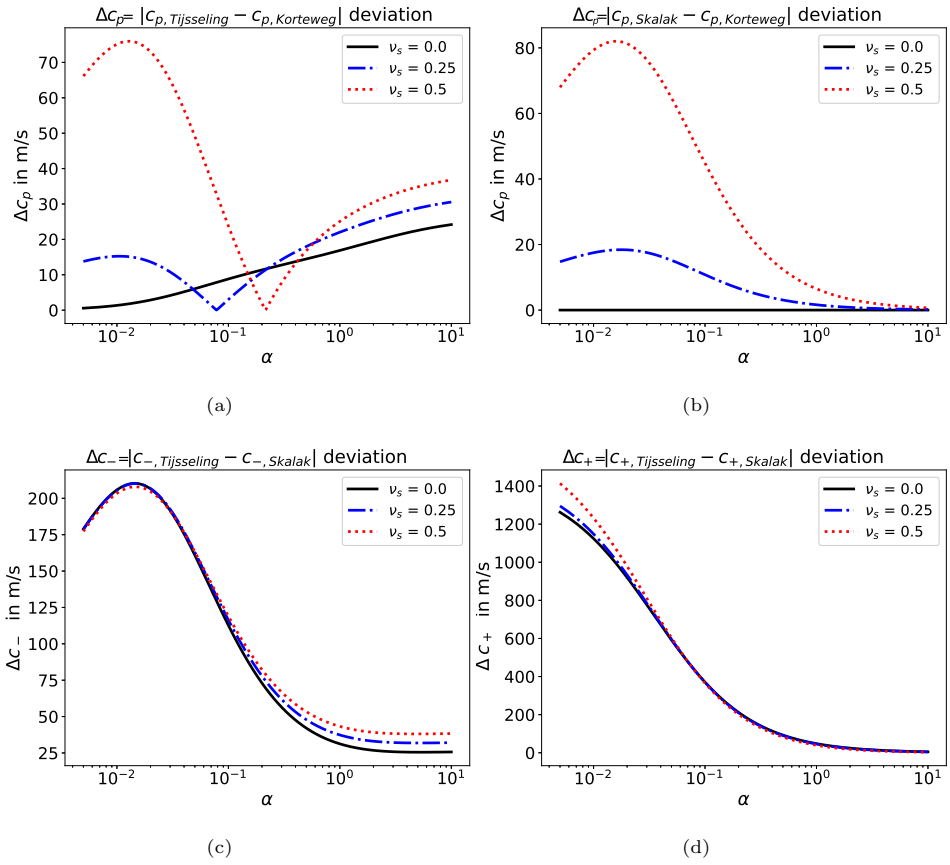

Figure 4: Pulse and (FSI)-corrective wave speeds deviation analysis for the models of [6, 10, 11, 43] for solid/fluid velocity ratio $\mathcal{C}_s = 4.93$, and fluid/solid density ratio $\mathcal{D} = 0.126$.

vantage of TMM is to be able to perform an explicit dependence of the solution to the prescribed boundary conditions for general sets of (linear) boundary conditions, either for FSI water-hammer [45, 46, 47, 48] or even in visco-elastic solid response [49]. TMM can either be expressed in time domain [50] or frequency domain [51, 52].

TMM has permitted explicit analytical solutions in restrained configurations. Non exhaustively among a vast literature TMM solutions have been developed for single pipe [47, 53], single pipe with elastic constraints [54], series pipe system [55], curved circular pipe [56], curved pipe with various degrees of freedom

[57], extended blockage [58], simple tree-like metric graphs [59], single pipe of arbitrary transverse shape approximated by Euler beam theory [60, 61] with various degrees of freedom or with visco-elatic solids [62, 63] in Laplace domain. In this section we first discuss the explicit way a transfer matrix condition is set for general linear boundary conditions. In the following some useful notation is considered, such as the dimensionless elastic velocity ratio

$$\mathcal{C}_s = \frac{c_s^*}{c_p^*}. \tag{37}$$

The physical time t^* is furthermore re-scaled with respect to the fluid acoustic advective time scale, i.e. $\tau = tL^*/c_p^*$, whereas the axial coordinate is non- dimensionalyzed by the pipe's length, i.e. $Z = z/L$. The perturbed fluid pressure P^*, and axial solid stress component σ_{zz}^*, are re-scaled by the [64]'s over-pressure, i.e. $O\left(\rho_f c_p W_0\right)$ where W_0 is the flow variation applied within the pipes, so that their dimensionless counterparts are denoted

$$P = \frac{P^*}{\rho_f^* c_p^* W_0^*} \quad \text{, and,} \quad \sigma_{zz} = \frac{\sigma_{zz}^*}{\rho_f^* c_p^* W_0^*}. \tag{38}$$

Note that, on the denominator of the right side of (38) the dimensionless stress σ_{zz} has been obtained from using Joukowsky's overpressure, anticipating the normal stress continuity between the fluid and the solid compartment. The dimensionless water-hammer four FSI hyperbolic equations can be recasted in the following two-wave coupled equation system (33)-(34) without friction coupling (i.e when $\tau_w^* = 0$)

$$\left(\partial_\tau^2 - \mathbf{C}_\mathbf{P}^2 \partial_Z^2\right) \mathbf{P} = \mathbf{0}, \tag{39}$$

where

$$\mathbf{C}_\mathbf{P}^2 = \begin{pmatrix} 1 & 2\nu_s \mathcal{D} \\ \frac{2\nu_s}{\alpha(2+\alpha)} & \frac{4\nu_s^2 \mathcal{D}}{\alpha(2+\alpha)} + \mathcal{C}_s^2 \end{pmatrix} \quad \text{, and,} \quad \mathbf{P} = \begin{pmatrix} P \\ \sigma_{zz} \end{pmatrix}. \tag{40}$$

Off-diagonal terms of matrix $\mathbf{C}_\mathbf{P}^2$ are proportional to the Poisson coefficient ν_s so that the fluid pressure and the solid stress decouple as $\nu_s \to 0$. Furthermore, as $\nu_s \to 0$ the remaining diagonal terms are 1 and $\mathcal{C}_s^2$, the two eigenvalues of the resulting diagonal matrix. These eigenvalues are providing the two distinct wave-velocities of the uncoupled limit: 1 which is the dimensionless pressure

pulse velocity c_p whereas $\mathcal{C}_s^2$ is the dimensionless elastic wave solid one. When $\nu_s \neq 0$ the eigenvalues of matrix $\mathbf{C}_{\mathbf{P}}^2$ provide the velocities of the coupled system. The vector homogeneous wave-equation resolution will be handled within the eigenvectors basis of $\mathbf{C}_{\mathbf{P}}^2$ as in [47]. The eigenvalues of $\mathbf{C}_{\mathbf{P}}^2$, denoted $c_\pm^2 > 0$, associated with diagonalized matrix $\boldsymbol{\mathcal{C}}_{\boldsymbol{\mathcal{P}}}^2$ correspond to the wave speed mode propagation. They are the solution of the following polynomial characteristic problem

$$c_\pm^4 - \left[1 + \mathcal{C}_s^2 + \frac{4\nu_s^2\mathcal{D}}{\alpha(2+\alpha)}\right] c_\pm^2 + \mathcal{C}_s^2 = 0, \tag{41}$$

the solutions of which are

$$c_\pm^2 = \frac{1 + \mathcal{C}_s^2 + \frac{4\nu_s^2\mathcal{D}}{\alpha(2+\alpha)} \pm \sqrt{\left(1 + \mathcal{C}_s^2 + \frac{4\nu_s^2\mathcal{D}}{\alpha(2+\alpha)}\right)^2 - 4\mathcal{C}_s^2}}{2}. \tag{42}$$

(42) is the dimensionless version of (36). The asymptotic behavior with respect to α parameter of all dimensionless velocity is illustrated in figure (5) from [65]. As α increases or $\nu_s \to 0$, the dimensionless positive and negative wave speed mode, c_+ tend to $\mathcal{C}_s$ and c_- tends to one. The various asymptotic limits of other dimensionless velocities are also reported for completeness in figure 5. The fluid pressure and the axial solid stress as well as their respective time-derivatives are assumed initially at rest so that

$$\mathbf{P}(Z,0) = \mathbf{0} \quad , \partial_\tau \mathbf{P}(Z,0) = \mathbf{0}. \tag{43}$$

In the diagonal base of matrix $\mathbf{C}_{\mathbf{P}}^2$ the system becomes

$$\left(\partial_\tau^2 - \boldsymbol{\mathcal{C}}_{\boldsymbol{\mathcal{P}}}^2 \partial_Z^2\right) \boldsymbol{\mathcal{P}} = \mathbf{0} \quad \text{, with,} \quad \boldsymbol{\mathcal{P}}(Z,0) = \partial_\tau \boldsymbol{\mathcal{P}}(Z,0) = \mathbf{0}, \tag{44}$$

where the change of basis

$$\boldsymbol{\Pi} = \begin{pmatrix} \frac{2\nu_s\mathcal{D}}{c_-^2 - 1} & \frac{2\nu_s\mathcal{D}}{c_+^2 - 1} \\ 1 & 1 \end{pmatrix}, \quad \boldsymbol{\mathcal{C}}_{\boldsymbol{\mathcal{P}}}^2 = \begin{pmatrix} c_-^2 & 0 \\ 0 & c_+^2 \end{pmatrix} \equiv \boldsymbol{\Pi} \mathbf{C}_{\mathbf{P}}^2 \boldsymbol{\Pi}^{-1} \quad \text{, and,} \quad \boldsymbol{\mathcal{P}} = \boldsymbol{\Pi}^{-1} \mathbf{P}, \tag{45}$$

has been used. The pressure-axial stress 2D-vector $\mathbf{P} = (P, \sigma_{zz})$ is transformed into a linear combination of those in 2D-vector $\boldsymbol{\mathcal{P}}$ from (45). The Laplace transform of (44) then leads to

$$\left(s^2 - \boldsymbol{\mathcal{C}}_{\boldsymbol{\mathcal{P}}}^2 \partial_Z^2\right) \tilde{\boldsymbol{\mathcal{P}}} = \mathbf{0}, \tag{46}$$

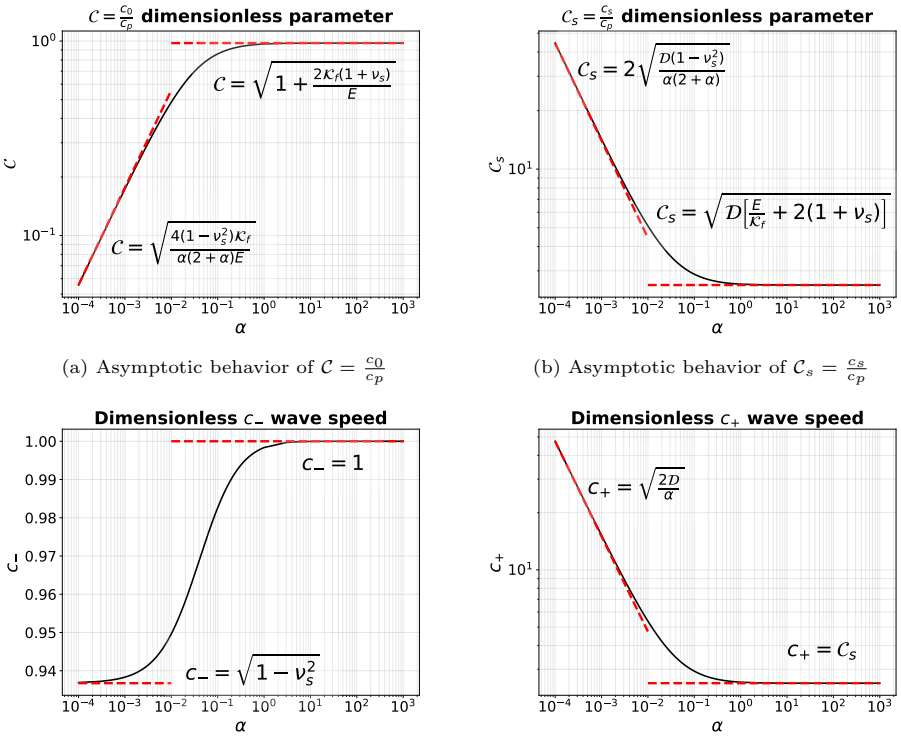

(a) Asymptotic behavior of $\mathcal{C} = \frac{c_0}{c_p}$

(b) Asymptotic behavior of $\mathcal{C}_s = \frac{c_s}{c_p}$

(c) Asymptotic behavior of c_-

(d) Asymptotic behavior of c_+

Figure 5: (taken form [65]) Wall tickness α-dependence ($\alpha = \frac{e}{R_0}$) of dimensionless characteristic FSI wave speeds for $\nu_s = 0.35$ and $\mathcal{D} = 0.1122$, $\frac{E}{\mathcal{K}_f} = 54$. The red dashed lines indicates various analytical asymptotic behaviors.

$\boldsymbol{\mathcal{C}}_{\boldsymbol{\mathcal{P}}}^2$ being diagonal given (45). A solution can be found for the spatial ODE system leading to

$$\tilde{\boldsymbol{\mathcal{P}}}(Z,s) = \mathbf{E}(Z,s)\tilde{\boldsymbol{\mathcal{P}}}^{\mathcal{D}}(s) + \mathbf{F}(Z,s)\tilde{\boldsymbol{\mathcal{P}}}^{\mathcal{N}}(s), \tag{47}$$

with 2×2 diagonal matrices

$$\mathbf{E}(Z,s) = \begin{pmatrix} \cos\left(\frac{is}{c_-}Z\right) & 0 \\ 0 & \cos\left(\frac{is}{c_+}Z\right) \end{pmatrix}, \quad \mathbf{F}(Z,s) = \begin{pmatrix} \sin\left(\frac{is}{c_-}Z\right) & 0 \\ 0 & \sin\left(\frac{is}{c_+}Z\right) \end{pmatrix}, \tag{48}$$

and $\tilde{\boldsymbol{\mathcal{P}}}^{\mathcal{D}}(s), \tilde{\boldsymbol{\mathcal{P}}}^{\mathcal{N}}(s)$ 2D-vectors yet to be found. $\tilde{\boldsymbol{\mathcal{P}}}^{\mathcal{D}}(s)/\tilde{\boldsymbol{\mathcal{P}}}^{\mathcal{N}}(s)$ provide the Dirichlet/Neumann mode-dependent amplitude of $\tilde{\boldsymbol{\mathcal{P}}}(Z,s)$ respectively associated with the condition imposed at location $Z = 0$ because $\mathbf{E}(0,s) = \mathbf{I}$ and $\mathbf{F}(0,s) = \mathbf{0}$. A general set of boundary conditions is stated as

$$\underset{(4\times 8)}{\begin{pmatrix} \boldsymbol{\mathcal{N}} & \boldsymbol{\mathcal{M}} & \mathbf{0} & \mathbf{0} \\ \mathbf{0} & \mathbf{0} & \boldsymbol{\mathcal{Q}} & \boldsymbol{\mathcal{R}} \end{pmatrix}} \underset{(4\times 1)}{\begin{pmatrix} \boldsymbol{\mathcal{P}}(0) \\ \partial_Z \boldsymbol{\mathcal{P}}(0) \\ \boldsymbol{\mathcal{P}}(1) \\ \partial_Z \boldsymbol{\mathcal{P}}(1) \end{pmatrix}} = \mathbf{0}, \tag{49}$$

with $\boldsymbol{\mathcal{N}}$, $\boldsymbol{\mathcal{M}}$, $\boldsymbol{\mathcal{Q}}$, $\boldsymbol{\mathcal{R}}$ 2×2 matrices associated with the Dirichlet/Neumann couplings at both ends. It is worth mentioning that condition 49 needs to be enlarged in the case where the applied boundary conditions depend on the velocity. Then, a four-dimensional wave vector including the fluid velocity and solid longitudinal acceleration needs to be considered as performed in [50]. Introducing notation $\boldsymbol{\mathcal{C}}_{\boldsymbol{\mathcal{P}}}^{-1} = \begin{pmatrix} c_-^{-1} & 0 \\ 0 & c_+^{-1} \end{pmatrix}$, from definition (48) one gets

$$\partial_Z \mathbf{E}(Z,s) = -is\boldsymbol{\mathcal{C}}_{\boldsymbol{\mathcal{P}}}^{-1}\mathbf{F}(Z,s), \qquad \partial_Z \mathbf{F}(Z,s) = is\boldsymbol{\mathcal{C}}_{\boldsymbol{\mathcal{P}}}^{-1}\mathbf{E}(Z,s) \tag{50}$$

Combining the expression of (47), (48) (50) with the Laplace transform of the boundary condition system (49) (into which the Laplace transform of the Dirac distribution $\delta(\tau)$ equals one, i.e $\tilde{\delta} = 1$), one finds

$$\begin{pmatrix} \tilde{\boldsymbol{\mathcal{P}}}^{\mathcal{D}} \\ \tilde{\boldsymbol{\mathcal{P}}}^{\mathcal{N}} \end{pmatrix}(s) = \boldsymbol{\mathcal{B}}^{-1}(s)\boldsymbol{\mathcal{S}}, \tag{51}$$

with $\boldsymbol{\mathcal{S}}$ being a constant 4-vector depending on the precise set of boundary conditions (explicit examples are given in [53]) and

$$\boldsymbol{\mathcal{B}} = \begin{pmatrix} \boldsymbol{\mathcal{N}} & is\boldsymbol{\mathcal{M}}\boldsymbol{\mathcal{C}}_{\boldsymbol{\mathcal{P}}}^{-1} \\ \boldsymbol{\mathcal{Q}}\mathbf{E}(1) - is\boldsymbol{\mathcal{R}}\boldsymbol{\mathcal{C}}_{\boldsymbol{\mathcal{P}}}^{-1}\mathbf{F}(1) & \boldsymbol{\mathcal{Q}}\mathbf{F}_k(1) + is\boldsymbol{\mathcal{R}}\boldsymbol{\mathcal{C}}_{\boldsymbol{\mathcal{P}}}^{-1}\mathbf{E}(1) \end{pmatrix}. \tag{52}$$

The inverse of (52) is then needed to find $\tilde{\boldsymbol{\mathcal{P}}}$ from solving (51). One can note that the general solution for arbitrary closure law can easily be deduced from solution (51) by multiplying the constant source term $\boldsymbol{\mathcal{S}}$ by the Laplace transform of the closure law (which depends on s). Alternatively, in time-domain, the general closure law solution is found from a convolution product with the impulse response solution as detailed in [50]. The impulse response is thus a generic solution. Following notations of [53] by introducing the adjugate matrix of $\boldsymbol{\mathcal{B}}$, namely $\mathbf{adj}\,[\boldsymbol{\mathcal{B}}]$ one can write

$$\boldsymbol{\mathcal{B}}^{-1}(s) = \frac{\mathbf{adj}\,[\boldsymbol{\mathcal{B}}(s)]}{\det \boldsymbol{\mathcal{B}}(s)}, \tag{53}$$

Let us furthermore introduce the two matrices

$$\mathbf{IO} = \begin{pmatrix} 1 & 0 & 0 & 0 \\ 0 & 1 & 0 & 0 \end{pmatrix}, \text{ and, } \mathbf{OI} = \begin{pmatrix} 0 & 0 & 1 & 0 \\ 0 & 0 & 0 & 1 \end{pmatrix}, \tag{54}$$

vector $\tilde{\boldsymbol{\mathcal{P}}}(s, Z)$ can then be found using (47), (51) and (53) to reach

$$\tilde{\boldsymbol{\mathcal{P}}}(s, Z) = [\mathbf{E}(Z, s)\mathbf{IO} + \mathbf{F}(Z, s)\mathbf{OI}]\, \frac{(\mathbf{adj}\,[\boldsymbol{\mathcal{B}}])}{\det \boldsymbol{\mathcal{B}}(s)} \boldsymbol{\mathcal{S}}, \tag{55}$$

(55) is the formal solution for the 2D-vector $\tilde{\boldsymbol{\mathcal{P}}}(s, Z)$ in the frequency domain. For specific sets of boundary conditions, this formal solution can be further developed into explicit analytical expressions. In [53] the complete analytical solutions of three families of boundary conditions are detailed, thus not repeated here. Nevertheless, there is one salient and generic feature of this solution which is of distinct importance : it diverges for specific values of s called poles. It can be shown from applying inverse Laplace transform and Cauchy theorem [53] that these poles provide the specific natural resonant frequencies of the wave system or, equivalently the specific oscillating modes of the time-domain solution. The ensemble of these discrete resonant frequencies is the solution's spectrum. As discussed in [53], from solution (55) one can find that this divergent condition at poles is given by condition

$$\mathcal{S}_{\mathcal{P}} = \{s \in \mathbb{C} \;\; | \det \boldsymbol{\mathcal{B}}(s) = 0\}. \tag{56}$$

Condition (56) can be translated into a transcendental equation, the roots of which are denoted s_k. One can find in [53] three configurations where the transcendental equation is explicitly given and for which, in each case, the root s_k is purely imaginary, i.e.

$$s_k = i\lambda_k \quad \text{, with,} \quad \lambda_k \in \mathbb{R}. \tag{57}$$

Curiously, it is only recently that a formal one-to-one mapping between TMM Laplace domain solutions and time domain ones has been clarified [50, 53]. One important consequence of this one-to-one mapping between Laplace domain and time-domain solutions is the appearance of discrete spectrum of λ_k, leading to $\sin(\lambda_k t)$ time oscillation modes. If no friction model is taken into account in these FSI function coupling solutions these modes are not damped. Including friction models produces damping with a resulting time decay specific to each mode as discussed in 2.3. Let us now add some aspects concerning time-domain solutions. Following notations of [50] the mode decomposition of time-domain solutions is performed over the eigen-function based $\boldsymbol{\Phi}_k(Z)$ of the heterogeneous operator $\mathcal{H}$ based on $\boldsymbol{\mathcal{C}}^2_{\boldsymbol{\mathcal{P}}}$ defined as

$$\mathcal{H}\boldsymbol{\Phi}_k(Z) \equiv \boldsymbol{\mathcal{C}}^2_{\boldsymbol{\mathcal{P}}} \cdot \partial_Z^2 \boldsymbol{\Phi}_k(Z) = -\lambda_k^2 \boldsymbol{\Phi}_k(Z), \tag{58}$$

The eigenfunctions have been given in [50] as $\boldsymbol{\Phi}_k = \boldsymbol{\phi}_k / \|\boldsymbol{\phi}_k\|$

$$\boldsymbol{\phi}_k(Z) = \begin{pmatrix} \cos\left(\frac{\lambda_k Z}{c_-}\right) + \tan\left(\frac{\lambda_k}{c_-}\right) \sin\left(\frac{\lambda_k Z}{c_-}\right) \\ -\frac{c_+}{\beta c_-}\left(\cos\left(\frac{\lambda_k Z}{c_+}\right) + \tan\left(\frac{\lambda_k}{c_+}\right) \sin\left(\frac{\lambda_k Z}{c_+}\right)\right) \end{pmatrix}, \tag{59}$$

with β defined as

$$\beta = \frac{c_+}{c_-} \frac{c_-^2 - 1}{c_+^2 - 1}. \tag{60}$$

Furthermore one has to define a general scalar product,

$$\forall \boldsymbol{\Psi}, \boldsymbol{\Psi}^{'} \in L^2(\mathbb{R}) \times L^2(\mathbb{R}), \quad \langle \boldsymbol{\Psi}^{'}, \boldsymbol{\Psi} \rangle = \sum_{j=1}^{2} \eta_j \int_0^1 \Psi_j^{'}(Z) \Psi_j(Z) dZ, \tag{61}$$

with $j = 1, 2$ referring to the j^{th} components of vector $\boldsymbol{\eta} \equiv (\eta_1, \eta_2) \in \mathbb{R}^2$, a real vector which is adapted to each specific problem, so that the operator 58 associated with boundary conditions 49 is self-adjoint. More precisely, invoking the definition of $\mathcal{H}$ in (58), the search for self-adjoint condition for operator $\mathcal{H}$, equipped with scalar product (61), performing a double integration by parts leads to

$$\begin{aligned} \langle \mathcal{H}\boldsymbol{\Psi}, \boldsymbol{\Psi}^{'} \rangle = \langle \boldsymbol{\mathcal{C}}^2_{\boldsymbol{\mathcal{P}}} \cdot \partial_Z^2 \boldsymbol{\Psi}, \boldsymbol{\Psi}^{'} \rangle = \langle \boldsymbol{\Psi}, \boldsymbol{\mathcal{C}}^2_{\boldsymbol{\mathcal{P}}} \cdot \partial_Z^2 \boldsymbol{\Psi}^{'} \rangle + \\ \sum_{j=1}^{2} \eta_j c_j^2 \left(\left[\partial_Z \Psi_j(Z) \Psi_j^{'}(Z) - \Psi_j(Z) \partial_Z \Psi_j^{'}(Z) \right]_0^1 \right), \end{aligned} \tag{62}$$

where c_j^2 are the j^{th} diagonal terms of $\boldsymbol{\mathcal{C}}^2_{\boldsymbol{\mathcal{P}}}$. From (62) self-adjoint property $\langle \mathcal{H}\boldsymbol{\Psi}, \boldsymbol{\Psi}^{'} \rangle = \langle \boldsymbol{\Psi}, \mathcal{H}\boldsymbol{\Psi}^{'} \rangle$, is thus obtained from condition

$$\sum_{j=1}^{2} \eta_j c_j^2 \left[\partial_Z \Psi_j(Z) \Psi_j^{'}(Z) - \Psi_j(Z) \partial_Z \Psi_j^{'}(Z) \right]_0^1 = 0. \tag{63}$$

Eigenfunctions $\boldsymbol{\Phi}_k(Z)$ are chosen of norm unity, i.e $\langle \boldsymbol{\Phi}_k, \boldsymbol{\Phi}_k \rangle = 1$ [50]. Operator $\mathcal{H}$ self-adjointess is a prerequisite to get a discrete spectrum composed of distinct eigenvalues as well as an orthogonal base decomposition. Using a proper choice of scalar product weight $\boldsymbol{\eta} \equiv (\eta_1, \eta_2)$ satisfying 63 permit to write the general time-domain solutions for the FSI problem to be decomposed into some homogeneous part and some particular solution taking care of non-homogeneous boundary conditions at the edges

$$\boldsymbol{\mathcal{P}}(Z,\tau) = \sum_{\mathcal{S}_p} a_k(\tau)\boldsymbol{\Phi}_k(Z) + \boldsymbol{\mathcal{P}}_p(Z,\tau), \tag{64}$$

where $a_k(\tau)$ are the mode amplitudes and $\boldsymbol{\mathcal{P}}_p$ is a particular solution lying in the kernel of $\mathcal{H}$, i.e

$$\mathcal{H}\boldsymbol{\mathcal{P}}_p = \mathbf{0}, \tag{65}$$

so that, it can be decomposed as a linear and constant field

$$\boldsymbol{\mathcal{P}}_p(Z,\tau) = Z\boldsymbol{\mathcal{P}}_p^1(\tau) + \boldsymbol{\mathcal{P}}_p^0(\tau), \tag{66}$$

where $\boldsymbol{\mathcal{P}}_p^1$ and $\boldsymbol{\mathcal{P}}_p^2$ are two time functions used to map boundary conditions as well as initial conditions as further detailed in [50]. Let us investigate further the homogeneous part of the time-domain solution in order to find how the spectrum solution condition appears in this case, and how does it compares to the one obtained in frequency domain. Transposing the TMM method in time domain one can propagate the boundary value from $Z = 0$ to a solution of (58) at coordinate Z from chosing

$$\boldsymbol{\Phi}_k(Z) = \mathbf{E}(Z, i\lambda_k)\boldsymbol{\Phi}_k(0) - \frac{1}{\lambda_k}\boldsymbol{\mathcal{C}}_{\boldsymbol{\mathcal{P}}}\mathbf{F}(Z, i\lambda_k)\partial_Z\boldsymbol{\Phi}_k(0) \tag{67}$$

which is built, from (48) definitions, so that when using (50) and again, $\mathbf{E}(0, i\lambda_k) = \mathbf{I}$, $\mathbf{F}(0, i\lambda_k) = \mathbf{0}$ one gets self-consistent $\boldsymbol{\Phi}_k(0) = \boldsymbol{\Phi}_k(0)$ both sides in (67). Similarly from derivating (67) using (50) again one finds

$$\partial_Z\boldsymbol{\Phi}_k(Z) = \lambda_k\boldsymbol{\mathcal{C}}_{\boldsymbol{\mathcal{P}}}^{-1}\mathbf{F}(Z, i\lambda_k)\boldsymbol{\Phi}_k(0) + \mathbf{E}(Z, i\lambda_k)\partial_Z\boldsymbol{\Phi}_k(0), \tag{68}$$

so that once again $\partial_Z\boldsymbol{\Phi}_k(0) = \partial_Z\boldsymbol{\Phi}_k(0)$ both sides in (68). Hence, using (67) and (68) at $Z = 1$, it is possible to express boundary condition (49) as

$$\begin{pmatrix} \boldsymbol{\mathcal{N}} & \boldsymbol{\mathcal{M}} \\ \boldsymbol{\mathcal{Q}}\mathbf{E}(1, i\lambda_k) - \lambda_k\boldsymbol{\mathcal{R}}\boldsymbol{\mathcal{C}}_{\boldsymbol{\mathcal{P}}}^{-1}\mathbf{F}(1, i\lambda_k) & -\frac{1}{\lambda_k}\boldsymbol{\mathcal{C}}_{\boldsymbol{\mathcal{P}}}\left[\boldsymbol{\mathcal{Q}}\mathbf{F}(1, i\lambda_k) - \lambda_k\boldsymbol{\mathcal{R}}\boldsymbol{\mathcal{C}}_{\boldsymbol{\mathcal{P}}}^{-1}\mathbf{E}(1, i\lambda_k)\right] \end{pmatrix} \begin{pmatrix} \boldsymbol{\Phi}_k(0) \\ \partial_Z\boldsymbol{\Phi}_k(0) \end{pmatrix} = 0 \tag{69}$$

A non-trivial solution to (69) boundary condition is only possible if the matrix has a non-empty kernel, i.e if its determinant equals zero. Comparing (69) with 52 shows

that these two matrices have a determinant which is proportional, so that the zero determinant condition leads to the same spectrum. Hence the discrete spectrum solution is identical either found from frequency domain or time domain. Furthermore, in time-domain, the homogeneous solution value and derivative at one node of the single pipe pertain to the null-space of a given matrix. We will find in the section 4.4.2 that the spectrum of vibrating modes into a network share a similar property, but for a distinct matrix.

2.2.2. Junction coupling within complex domains

Within pipe systems and networks, even in the case of linear boundary conditions, most of the literature analyze junction coupling using numerical methods. This is mostly because in this more complex context, analytical solutions are most often not possible to find. Nevertheless section 4.4 covers recent advances whereby some algebraic analytical solutions are discussed in networks. Since dealing with an hyperbolic problem, classical numerical methods have been adapted and developed to solve water-hammer wave propagation using Method of Characteristics (MOC) [66, 67, 68, 69, 70], Finite Element Method (FEM) [71, 72, 73, 74, 75, 76, 77], Finite-Volume method (FV) [78, 79, 80, 81, 82, 83] or coupled MOC–FEM [84]. The respective pros and cons of these various methods have been discussed in several specific reviews [27, 15, 85], so that a similar meticulous discussion will not be be repeated here. When FSI's effects are ignored considering the pressure transient dynamics in hydraulic systems [13], MOC is one of the most popular methods. Rather than considering a pressure wave second order propagation operator, it is more precise and easier to consider the first order coupled hyperbolic problem associated with the pressure and velocity (82). Since for water-hammer wave propagation within pipes having elastic properties (such as metallic materials), the wave velocity is homogeneous along each pipe, MOC provides an easy to implement, very weakly dissipative integration method. MOC nevertheless has two intrinsic drawback/weakness. First, a Courant–Friedrichs–Lewy (CFL) condition (obviously not specific to MOC's method) $c_{p_{ij}}\Delta t_{ij}/\Delta Z_{ij} < 1$ has to be fulfilled along each pipe ij, connecting node i to node j whereby the wave velocity is $c_{p_{ij}}$ prescribing a constraint between time-step Δt_{ij} and spatial discretization ΔZ_{ij}. Since the CFL condition has to be fulfilled in each pipe, the most restrictive time step enslaves all others so that the time step is $\Delta t = \min_{ij} \Delta t_{ij}$. The CFL condition also prescribes the spatial discretization $\Delta Z_{ij} = c_{p_{ij}}\Delta t$ in each pipe. This constraint con-

siderably enlarges the number of unknowns of the problem as well as imposes a small constant time-step (without the possible use of adaptative time-stepping). The second drawback is that even if MOC is well adapted to non-dispersive wave propagation, i.e propagation with constant wave speed, this framework is limited and not always relevant. For example, in the case of water-hammer within visco-elastic pipes, the wave-speed is not constant over time. In this case, MOC method is not well adapted even though some scheme and approximations have been developed to extent its application in this context [27, 15, 85]. On the contrary, FEM and FV methods permit the use of adaptative time stepping and/or implicit time integration schemes debilitating the numerical cost of the CFL constraint. Both FEM and FV can be applied with stabilizing hyperbolic schemes (the most popular being the Godunov scheme for FV [78, 79, 86], and possibly the Streamline Upwind Petrov–Galerkin SUPG for FEM [87]). One distinct advantage of FE over FV is its ability to deal with FSI from solving the coupled solid elasto-dynamic problem. Furthermore, considering FEM method in more than one dimension in space (e.g non axi-symmetrical breathing varying along θ) also permit to handle much more general deformations (e.g yaw, torsion, etc..) than pipe breathing modes mostly considered in this review.

2.3. Friction coupling with shear stress dissipation modeling

As recently discussed in an authorized survey by A. E. Vardy [88], friction is one mechanism of water-hammer's damping having attracted much attention, by the author himself but also many others as will be discussed just below. Many modeling efforts have indeed been dedicated to model the experimental damping of water-hammer waves, which turns-out to be a subtle, difficult, but also central issue in the topic. Let us start briefly from mentioning why this issue definitely owns a practical interest. From neglecting wave dissipation and dispersion, surge analysis is a current engineering computation which permits to localize the most dangerous spots, i.e locations where the water-hammer pressure can exceed security prescriptions into a given installation, resulting from a given operation/incident within the network (e.g. valve closing, hydraulic motor tripping, check valve failure, pipe breakage, etc...). Obviously this analysis can be overprotective, and possibly alarming. Hence more accurate predictions for water-hammer events is of interest for lowering the cost of water-hammer protection equipment and security design of a given installation. This is where friction modeling kicks-in. As for any modeling, two strategies can be pursued : on the one

hand, a practical one, dealing with developing specific, dedicated and accurate models able to describe observations. On the other hand, a more generic one trying to decipher which friction mechanisms are involved, and how they could be modeled in a generic way. Before entering into the details of friction model, we would first like to mention (for honesty and perhaps clarity) that this review is more oriented toward the second modeling effort. One motivation behind this tropism is the ability to quantify the respective contributions involving various superposed effects, so as to be predictive in different situations. Nevertheless, albeit many research efforts, this issue has not reached this level of maturity, as now detailed.

Some wall-shear-stress models emerged from the hydraulic analysis of viscous flow in pipes, ignoring (FSI) effects. In many cases, the acoustic hypothesis is used for the fluid and the Poisson coupling is discarded, [89, 90, 91, 13, 92].

Nevertheless before discussing the various dissipation models proposed in the literature, let us step out to properly derive how the wall shear-stress happens to be the key ingredient in this issue. As previously mentioned in 2.1 the momentum balance second equation of Tijsseling's four-equation FSI model (34) can be deduced using Reynolds transport theorem. Considering a flexible tube, i.e a tube whose radius and section varies in time, where a velocity field $\mathbf{u}^*$ flows, momentum balance in the fluid (without body force) reads

$$\rho_f^* \frac{d\mathbf{v}^*}{dt^*} = \nabla \cdot \boldsymbol{\sigma}_f^*, \tag{70}$$

where the fluid stress-tensor of a Newtonian fluid is

$$\boldsymbol{\sigma}_f^* = -P^*\mathbf{I} + \mu_f^*(\boldsymbol{\nabla}\boldsymbol{v}^* + \boldsymbol{\nabla}\boldsymbol{v}^{*T}) = \boldsymbol{\sigma}_f^* = -P^*\mathbf{I} + 2\mu_f^*\boldsymbol{e}^*{}_f, \tag{71}$$

where the deviatoric part of $\boldsymbol{\sigma}_f^*$ is related to the symmetric velocity gradient $\boldsymbol{e}^*{}_f = 1/2(\boldsymbol{\nabla}\boldsymbol{v}^* + \boldsymbol{\nabla}\boldsymbol{v}^{*T})$ defined in (71). Let us first consider (70)'s r.h.s. Integrating (70) into the infinitesimal volume $\Omega(t^*) = S^*(z^*, t^*) \times \epsilon_z$, based upon the product between the section S^* with the infinitesimal thickness ϵ_z along z direction, whilst using the divergence theorem leads to

$$\int_{\Omega(t^*)} \nabla \cdot \boldsymbol{\sigma}_f^* = \int_{S^*(z^*+\epsilon_z,t)} \boldsymbol{\sigma}_f^* \cdot \mathbf{n} ds + \int_{S^*(z^*,t)} \boldsymbol{\sigma}_f^* \cdot \mathbf{n} dS + \epsilon_z \int_{\mathcal{C}^*} \boldsymbol{\sigma}_f^* \cdot \mathbf{n} d\mathcal{C}^* \tag{72}$$

where $\mathcal{C}$ is again the contour of surface $S^*(z^*,t)$. (72) gives

$$\int_{\Omega(t^*)} \nabla\cdot\boldsymbol{\sigma}_f^* = -S^*\left(\overline{P}(z^*+\epsilon_z)-\overline{P}(z^*)\right)\mathbf{e}_z+\epsilon_z\int_{\mathcal{C}^*}\boldsymbol{\tau}_w^* d\mathcal{C}^* \\ +2\mu_f\int_{S^*(z^*+\epsilon_z,t)\cup S^*(z^*,t)}\boldsymbol{e}^*{}_f\cdot\mathbf{e}_z, \tag{73}$$

where $\overline{P}$ denotes the surface average pressure, i.e $\overline{P}=\int_{S^*}Pds/S^*$. Let us now take care of the integral of (70)'s l.h.s. For this we use the Reynolds transport theorem (29) for vector field $\boldsymbol{\Psi}=\rho_f^*\boldsymbol{v}^*$ which leads to

$$\frac{d}{dt^*}\int_{\Omega(t^*)}\rho_f^*\mathbf{v}^* d\Omega=\int_{\Omega(t^*)}\left(\frac{\partial(\rho_f^*\mathbf{v}^*)}{\partial t^*}+\nabla\cdot(\rho_f^*\mathbf{v}^*\mathbf{v}^*)\right)d\Omega \tag{74}$$

Developing the r.h.s integrand term of (74) leads to

$$\frac{\partial(\rho_f^*\mathbf{v}^*)}{\partial t^*}+\nabla\cdot(\rho_f^*\mathbf{v}^*\mathbf{v}^*)=\mathbf{v}^*\left(\frac{\partial\rho_f^*}{\partial t^*}+\nabla\cdot(\rho_f^*\mathbf{v}^*)\right)+\rho_f^*(\frac{\partial\mathbf{v}^*}{\partial t^*}+\mathbf{v}^*\nabla\cdot\mathbf{v}^*) \tag{75}$$

Since the local version of the integrated mass balance (4)'s reads

$$\partial_{t^*}\rho_f^*+\nabla\cdot(\rho_f^*\mathbf{v}^*)=0, \tag{76}$$

this permits to simplify the r.h.s of (75), so that using (76) in (75) and (74) then leads to the equality

$$\frac{d}{dt^*}\int_{\Omega(t^*)}\rho_f^*\mathbf{v}^* d\Omega=\int_{\Omega(t^*)}\rho_f^*\frac{d\mathbf{v}^*}{dt^*}d\Omega \tag{77}$$

Using now the domain $\Omega(t^*)=S^*(z^*,t^*)\times\epsilon_z$, integrating (70)'s l.h.s using (77) and (73) whilst dividing both sides by ϵ_z, projecting the vectorial equality along $\mathbf{e}_z$ and taking the limit $\epsilon_z\to 0$ leads to

$$\frac{d}{dt^*}\int_{S^*}\rho_f^* w^* ds=-S^*\frac{\partial\overline{P}}{\partial z^*}+\int_{S^*}\mu_f^*\frac{\partial^2 w^*}{\partial z^{*2}}ds+\int_{\mathcal{C}^*}\tau_w^* d\mathcal{C}^*. \tag{78}$$

We now consider axi-symmetric wave perturbations (pipe breathing perturbations) for which τ_w^* is uniform along $\mathcal{C}^*$. Furthermore, a core acoustic wave velocity for which the longitudinal velocity field w^* is uniform and denoted W^* is also considered. On (78)'s l.h.s, there is small contribution of boundary layers where w^* tends to zero near the boundary, but these regions are small. More precisely denoting δR_0^* the boundary layer thickness, as $\delta\equiv\sqrt{1/\epsilon Re_p}$ with $\delta\ll 1$, $\epsilon=R_0^*/L\ll 1$ and $Re_p=R_0^* c_p^*/\nu\gg 1$. The correction from these regions to (78)'s l.h.s are $O(\delta)$. Similarly, on (78)'s r.h.s, a core acoustic perturbation having constant longitudinal velocity W^* is such

that $\partial^2 W^*/\partial z^{*2} = 0$, so that a non-zero contribution of the viscous dissipation term $\partial^2 w^*/\partial z^{*2}$ is found only within the boundary layer. This leads to

$$\frac{d}{dt^*}(S^*\rho_f^* W^*)(1+O(\delta)) = -S^*\frac{\partial \overline{P}}{\partial z^*} + 2\pi R^* \tau_w^*(1+O(\delta)), \tag{79}$$

Furthermore, from integrated mass-balance (4) one gets

$$\frac{d}{dt^*}(\rho_f^* S^*) + \rho_f^* S^* \partial_{z^*} W^* = 0, \tag{80}$$

so that, finally, using (80) in (79) leads to

$$\rho_f^* \partial_{t^*} W^*(1+O(\delta)) = -\frac{\partial \overline{P}}{\partial z^*} + \frac{2}{R^*}\tau_w^*(1+O(\delta)), \tag{81}$$

Since $\delta \ll 1$, $O(\delta)$ corrections are generally neglected so that (81) is identical with the second line of (33). (81)'s r.h.s thus involve a source term proportional to wall shear stress and responsible for the wave damping. It is directly related to the viscous dissipation arising within the liquid boundary layer. Hydraulic water-hammer modeling has mainly been focused on dissipative viscous losses, whilst disregarding (FSI) effects. More precisely, this means that most of the hydraulic literature ignores the stress-acceleration equations (34) and only consider (33) discarding Poisson's coupling, i.e in the $\nu_s \to 0$ limit. In this limit, the set of four-(FSI) equations introduced in (33)-(34), simplifies to two coupled first order hyperbolic equations for the fluid pressure P and longitudinal velocity W^* [93, 94]

$$\left[\partial_{t^*} + \begin{pmatrix} 0 & \rho_f^* c_p^{*2} \\ \frac{1}{\rho_f^*} & 0 \end{pmatrix} \partial_{z^*}\right] \begin{pmatrix} P^* \\ W^* \end{pmatrix} = -\frac{2\tau_w^*}{\rho_f^* R_0^*} \begin{pmatrix} 0 \\ 1 \end{pmatrix}. \tag{82}$$

The coupled first order hyperbolic problem (82) can be re-casted into a second order wave equation, in dimensionless form, using $z^* = ZL$ as quoted in [13, 95]

$$\left[\partial_t^2 - \partial_Z^2\right] P = 2\delta \frac{\partial \tau_w}{\partial Z}. \tag{83}$$

When viscosity effects are taken into account, one needs a wall shear-stress model. This issue turns out to be central, for a correct evaluation of the wave damping prediction and this is why it has attracted so many studies in the literature. But, as previously stated, it is a subtle issue, for which there is still surprisingly remaining open questions at the present state of the art, as will be discussed at the end of this section. Furthermore, the dimensionless pressure wave (83) shows that the dissipation

rate is slow since the r.h.s is small, i.e $O(\delta)$. This specific asymptotic property has nevertheless been used only recently, and will thus be discussed in section 4.1.

A first intuitive empirical and popular wall shear-stress model is built from the extension of the steady-state Darcy-Weisbach friction law (Cf. [19, 96, 13]) to hydraulic transient. The use of the redesigned quasi-steady wall shear rate τ_{qst}

$$\tau^*_{qst}(z^*,t^*) = \frac{\rho^*_f f_{DW} W^*(z^*,t^*)|W^*(z^*,t^*)|}{8}, \tag{84}$$

through the dimensionless Darcy-Weisbach coefficient f_{DW}, is nevertheless questionable for transient investigations. Poor experimental agreement is sometimes found using this dissipation model [97, 98, 99]. Furthermore, even if the extension of steady friction to quasi-steady one seems a plausible model at first sight, one should bear in mind that (84) has not been established within any rigorous derivation framework. Also, this wall-shear stress model considers that the rapid wave shear is coupled with the steady-state velocity. How such coupling between steady and transient happens for the shear stress is elusive. We will consider this issue in a much deeper way in section (4.2), so as to address the fluid mechanics behind a possible coupling between the steady-flow and the unsteady one, still not well understood at the present state of the art.

This quasi-steady model has then been enriched to improve the experimental attenuation's predictibility. Several classes of model, [16] have been established: (i) instantaneous material acceleration-based (IMAB) models and, (ii) weighting function-based (WFB). Although conceptually different, these two approaches seek to account for the same physical observation, that the near-wall dynamics does not instantaneously respond to the core velocity variations. The energetic dissipation emerges from the time response delay between the central part of the flow and its boundary layer. Finally, these models are based on a decomposition of the total wall shear rate into a quasi-steady component, via the use of the Darcy-Weisbach model (84), and a transient one τ^*_{tr}, [13]

$$\tau^*_w = \tau^*_{qst} + \tau^*_{tr}. \tag{85}$$

The τ^*_{tr} component is then expected to fill the gaps between the model predictions and the experimental observations, when only a quasi-steady wall shear stress model is considered.

Instantaneous material acceleration-based (IMAB) model. IMAB relies on semi-empirical observations and assumes a linear variation of the transient wall shear stress τ^*_{tr}, with respect to the mean flow acceleration $\partial_{t^*} W^*$. These models arise from the experimental work of [100]. The author analyzed the turbulence structure in a pressurized flow with or without orifices. [100] highlighted the time delay between the response of boundary lines with respect to the mean flow variations. He then proposes the following transient wall shear stress model

$$\tau^*_{tr} = \frac{\rho_f k_3 R^*_0}{2} \partial_{t^*} W^*, \tag{86}$$

where k_3 account for the boundary response deviation. When re-injecting the above transient wall shear stress expression into the hyperbolic constitutive equation set (82), it turns out that no energetic damping arises, [101]. Indeed, the time-derivatives of both (82) and (86) can be factorized so that no source term remains in the hyperbolic system r.h.s. However, the structure of the hyperbolic system, i.e. its eigenvalues and eigenvectors, are modified by k_3. The wave speed is thus modified by a $1/\sqrt{1+k_3}$ prefactor. To account for energetic losses, the (IMAB) model was then later completed by [102, 98]. The authors added a convective term to the transient shear-stress (86) and proposed that

$$\tau^*_{tr}(x,t) = \frac{\rho^*_f k_3 R^*_0}{2} \left(\partial_{t^*} W^* + c^*_p \cdot sgn(W) \left| \partial_{z^*} W^* \right| \right), \tag{87}$$

where $sgn(W)$ stands for the accelerating or decelerating transient flow phase. This inertial contribution, similar to the Navier's inertial terms, creates a source term in the hyperbolic system (82). Consequently, the (IMAB) model intends to model both the attenuation and the phase shift of overpressure waves. Some authors, [103, 104, 105], also developed a slightly distinct model by using a second semi-empirical parameter $k_3^{'}$

$$\tau_{tr}(x,t)^* = \frac{\rho^*_f R^*_0}{2} \left(k_3 \partial_{t^*} W^* + k_3^{'} c^*_p \cdot sgn(W^*) \left| \partial_{z^*} W^* \right| \right) \tag{88}$$

and then distinguished the phenomenon of wave speed deviation from the damping one, [101]. When the single coefficient model is used in (87), an approximation arising from theoretical arguments is used to estimate the Reynolds number dependence of k_3, [106]

$$k_3 = \frac{\sqrt{0.00476}}{2} \text{ , if, } Re \leq 2000, \tag{89}$$

$$k_3 = \frac{1}{2} \sqrt{\frac{7.41}{Re^{\log\left(\frac{14.3}{Re^{0.05}}\right)}}} \text{ , else,} \tag{90}$$

where $Re = W_0 R_0/\nu_f$ is the Reynolds number, W_0 is a reference axial fluid velocity magnitude and ν_f is the fluid kinematic viscosity. The review of [13] provides an excellent state-of-the-art of (IMAB) models. In addition to the use of semi-empirical models, some analytical developments relying on a weighting function-based (WFB) approach, have also been carried out.

Weighting function-based (WFB) model. WFB seeks for an analytical description of the viscous shear energetic losses. One of the first noteworthy contributions has been provided by [107]. In the low-Mach number acoustic framework, i.e. neglecting Navier's inertial terms and decomposing the fluid variables into steady and perturbed components, the authors performed a Laplace domain analysis of the fluid mass and momentum conservation equations. They found a radial- Bessel-dependent solution for the axial fluid velocity $W^*(r)$. The transient wall shear stress was then also derived, directly from a direct computation of the shear

$$\tau^*_{tr} = \rho^*_f \nu^*_f \partial^*_r W^* \Big|_{r=R_0}. \tag{91}$$

This theoretical approach is also consistent with [7] for the maximum overpressure prediction. Furthermore, [13] highlighted the relevance of a previously defined dimensionless parameter associated with the pressure waves damping, which is now known as the water-hammer small parameter δ

$$\delta^2 = \frac{\nu^*_f L^*}{c^*_p R^{*2}_0} = \frac{\nu^*_f}{R^{*2}_0} \cdot \frac{L^*}{c^*_p} \equiv \frac{t^*_c}{t^*_{vis}} \equiv \frac{1}{\epsilon Re_p}, \tag{92}$$

where $t^*_{vis} = R^{*2}_0/\nu^*_f$ is the viscous diffusion time-scale within the boundary layer, and $t^*_c = L^*/c^*_p$ is the advective time-scale of the wave, $\epsilon = R^*_0/L^*$ is the inner pipe's radius to its length ratio and $Re_p = R^*_0 c^*_p/\nu^*_f$ is the pulse re-scaled Reynolds number. This small parameter is the cornerstone of the asymptotic analysis of water hammer as will be discussed in section 4.1. Approximatively at the same time as Holmboe, Zielke [108, 109] delivered a famous analysis of fully developed laminar boundary layer and derived a diffusion equation of the axial fluid velocity, forced by the longitudinal pressure gradient

$$\left[\partial^*_t - \nu^*_f \frac{\partial^*_r}{r^*}\left(r^* \partial^*_r\right)\right] W^* = -\frac{1}{\rho^*_f} \partial_{z^*} P^*. \tag{93}$$

Solving (93) in the Laplace domain, and then performing an inverse Laplace transform using Cauchy's residue theorem leads to a time-convoluted form of the wall shear stress

$$\tau_w^* = \underbrace{\frac{4\rho_f^*\nu_f^*}{R_0^*}W^*}_{\tau_{qst}^*} + \underbrace{\frac{2\rho_f^*\nu_f^*}{R_0^*}\int_0^{t^*}\Theta_{Zielke}(t^*-\tau^*)\partial_\tau^* W d\tau^*}_{\tau_{tr}^*}, \tag{94}$$

where $\Theta_{Zielke}(t)$ is the convolution kernel. For practical use of this kernel Zielke has provided some approximate fitting of the form

$$\Theta_{Zielke}(t^*) = \sum_{i=0}^{5} m_i \left(\frac{t^*}{t_{vis}^*}\right)^{\frac{i-1}{2}} \text{, if } \frac{t}{t_{vis}} \leq 0.02, \tag{95}$$

$$\Theta_{Zielke}(t^*) = \sum_{i=0}^{4} e^{-n_i \frac{t^*}{t_{vis}^*}} \text{, if, } \frac{t^*}{t_{vis}^*} > 0.02, \tag{96}$$

where n_i, m_i parameters can be found in [109]. The presence of the τ_{qst} term in (94) arises form the fact that W. Zielke did not decompose his fluid velocity and pressure fields into steady and perturbed components as its classically done in the low Mach number acoustic framework. This point is highlighted here and will be discussed further in section 4.1. It is interesting to point out that the W. Zielke's kernel is convoluted with the fluid mean acceleration. It then reflects that the underlying physical phenomenon governing the energetic damping in the (WFB) models and in the (IMAB) ones is the same (Cf. (86)), and relies on the non-instantaneous response of the boundary layer with respect to the core acceleration. Whilst the (IMAB) assumes a direct linear relation between the wall shear stress and the mean acceleration using k_3, the (WFB) embeds all the historic mean flow variations through a time convolution with $\Theta_{Zielke}(t)$. The scaling of the W. Zielke convolution kernel is obtained regarding both the first term of (95) and by setting up the characteristic advective time scale $\tau_c = \frac{L^*}{c_p^*}$, thus leading to

$$\Theta_{Zielke} \equiv O\left(\frac{1}{\delta}\right), \tag{97}$$

with δ as introduced in (92). The convolution kernel scaling thereby merges with the conclusion of [107]. Finally, the author confronted his theory to the experimental data of [107] and a very close agreement was found as revealed in Figure 6. [110] extended W. Zielke's work into an asymptotic analysis which supposes a near wall inner concentrated laminar boundary layer, or a skin friction model. The flow in the core area, bulk or outer region, is then considered as inviscid. The Figure 7a provides a schematic representation of the [110]'s asymptotic model. During a transient event, the authors supposed that: "*the fluid remains divided into a turbulent core and laminary boundary layer and that, the boundary-layer thickness remains constant.*" The

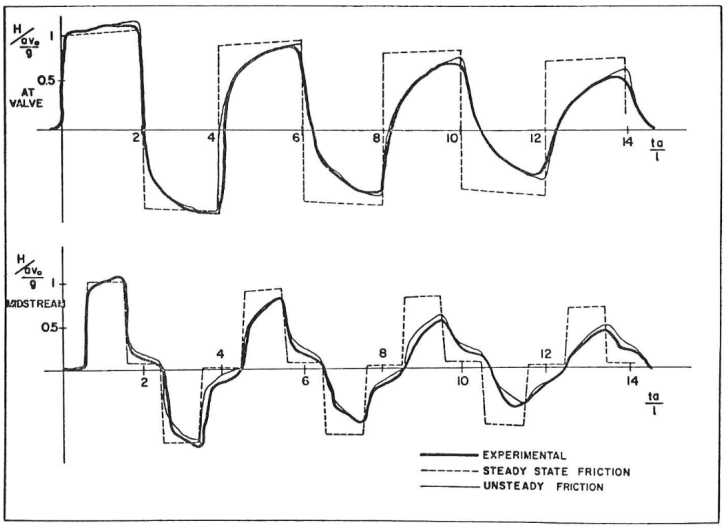

Figure 6: [109]'s theoretical predictions compared to [107]'s experimental data. The following notation are used: H the hydraulic head line, a the pulse wave speed.

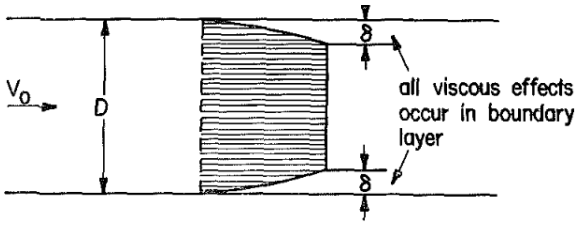

(a) Laminar boundary layer concept, [110].

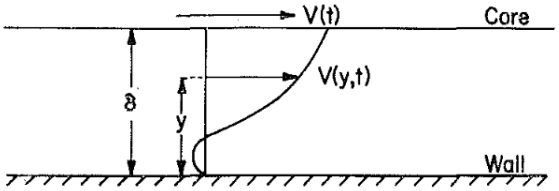

(b) Axial velocity matching at the fluid boundary layer interface, [110].

Figure 7: [110] boundary layer model for pressure waves energetic damping.

boundary layer thickness, and hence its dynamics, are thus governed by the preexisting flow regime. The dimensionless steady boundary layer thickness δ_{st}, follows from the

equilibrium of steady state viscous terms with the initial the pressure gradient

$$\delta_{st} = \frac{4}{f_{DW} Re}. \tag{98}$$

Two approaches are then proposed to evaluate the attenuation of pressure waves. The first one relies on solving the inner region problem associated with the diffusion equation upon the axial velocity in the boundary layer. A velocity matching at the boundary layer interface is then performed to ensure kinematic continuity conditions (Cf. Fig.7b). The second method involves energy balance from taking into account energy losses via the quadratic integral of the wall shear-stress over the boundary layer thickness. [97] extended a similar asymptotic approach from designing a two-dimensional model to describe the viscous losses in both the laminar and turbulent regions. By considering the pipe as an in-extensible solid, i.e. without radial dilatation, they decomposed the fluid into a succession of interconnected concentric ring of small thicknesses. Each layer of fluid is coupled to others via momentum transfers, radial kinematic and shear stress continuity, as depicted in Figure 8. Ensuring mass and

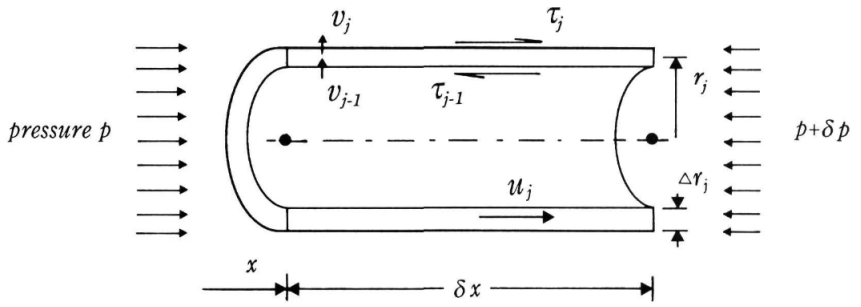

Figure 8: Momentum balance on a cylinder element, [97]

momentum conservation within each rings, [97] derive a coupled hyperbolic system forced by the radial transfer. For turbulent flow regimes, a five-region model has been adopted to model the shear rate. The authors found: "*pleasantly surprising that Zielke's expression is so successful even through his assumed (laminar) initial velocity profile differs markedly from reality*". [113] extended the laminar framework of [110] by taking into account the Reynolds-dependence of the flow in its convolution kernel. The flow is again divided into two regions: (i) the acoustic outer (*bulk*) region where the velocity field is radially uniform (ii) the inner boundary layer (*annulus*) where viscous effects are concentrated. The dimensionless boundary layer thickness is once again set

up to match with the preexisting flow conditions. Inspired by the experimental results of [114], [110] highlights the effects of the initial Reynolds number upon the convolution kernel structure as illustrated in Figure 9. In the boundary layer, a diffusion equation is

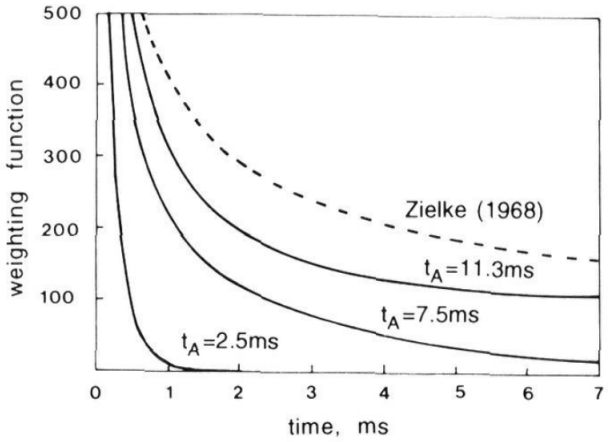

Figure 9: [113] discussion on the convolution kernel Reynolds-dependence according to the experimental work of [114].

once again derived in [113], which merges with [109, 110] analysis. The improvement and elegance of [113]'s model lies in the inner-outer *asymptotic matching* handling. The authors finally yielded the derivation of a Reynolds-dependent transient wall shear stress kernel expression (via the δ_{st} parameter)

$$\Theta(t)_{\text{Vardy et al. (1993)}} \approx \frac{1}{\delta_{st}} \sum_{k \in \mathbb{N}^*} e^{-[\frac{k\pi}{\delta_{st}}]^2 \frac{t^*}{t^*_{vis}}} \equiv O\left(\frac{1}{\delta_{st}}\right). \tag{99}$$

The experimental contributions of [115, 116] on the turbulent kinematic viscosity distribution in pipes, permitted [106] to extend [113] to account for higher Reynolds numbers ($Re \gg 10^5$). This new model, valid in a smooth pipe, is based on an idealized radial distribution of the turbulent kinematic viscosity in the boundary-layer as shown in Figure 10a. In this work, a core viscosity ν_c to wall viscosity ν_w ratio is introduced and used to characterize the turbulent kinematic distribution

$$\frac{\nu_c}{\nu_w} \equiv \sigma_{\text{Vardy}} \approx 0.173 \left(f_{DW} Re\right)^{1.12}, \tag{100}$$

whilst a new dimensionless boundary layer thickness is set up to scale in

$$\frac{b}{R_0} = \delta_{st} \frac{u_c}{U} \frac{\sigma_{\text{Vardy}} - 1}{\ln\left(\sigma_{\text{Vardy et al.}}\right)}, \tag{101}$$

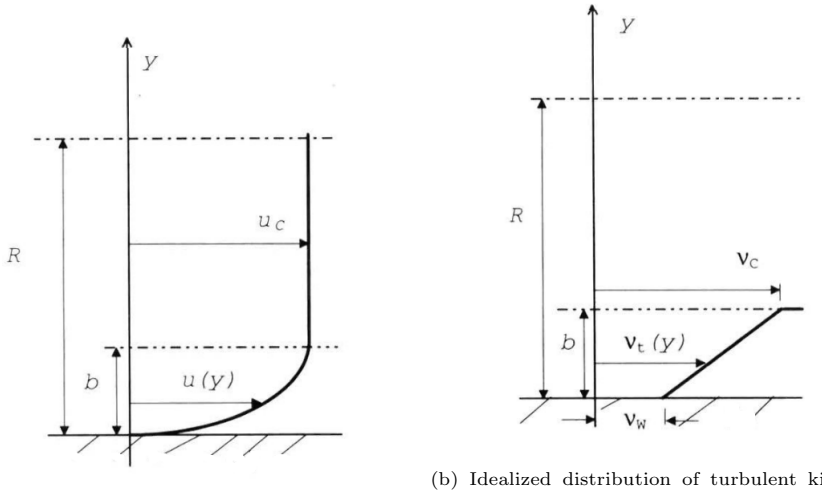

(a) Skin friction axial velocity distribution, [106]

(b) Idealized distribution of turbulent kinetic viscosity, [106]

Figure 10: Idealized velocity and viscosity distribution for the skin friction model of [106].

where u_c is the uniform core velocity, U the mean flow velocity per section and b is the dimensional boundary layer thickness. In the limit σ_{Vardy} tends to unity, the dimensionless boundary layer thickness of [113], presented in (98), is recovered. A similar asymptotic analysis as in [113] is carried out in [106] yielding to the derivation of a modified convolution kernel

$$\Theta(t)_{\text{Vardy et al. (1995)}} = \frac{A^* e^{-B^* \frac{t^*}{t^*_{vis}}}}{\sqrt{\frac{t^*}{t^*_{vis}}}}, \quad A^* = \frac{1}{2\sqrt{\pi}}, \quad B^* = 0.135 Re^{\log_{10}\left(\frac{14.3}{Re^{0.05}}\right)}. \tag{102}$$

For $t \equiv O\left(\frac{L}{c_p}\right)$, one finds

$$\Theta(t)_{\text{Vardy et al. (1995)}} \equiv O\left(\frac{1}{\delta}\right). \tag{103}$$

Under the hypothesis of constant transient acceleration, i.e. if $\partial_t W$ constant in (94), [106] derived a straightforward relation between the semi-empirical deviation constant k_3, and their inertial shear coefficient B^*

$$k_3 \approx \frac{1}{2\sqrt{B^*}}. \tag{104}$$

This relation provides a plausible justification for the derivation of (89)-(90). [106] point-out the Reynolds-dependence of parameter k_3. Additional discussions concerning the relations between [106]'s model and the (IMAB) ones are developed within

[102]. Finally, it is important to mention that many expressions have been proposed to model A^* and B^* from model (102) derived from several approximations. For example, [117] extend their previous model by modifying both (i) their idealized turbulent viscosity distribution (until then considered as infinite in the acoustic core) and, (ii) considering the boundary-layer thickness as independent from Reynolds. [117] reached a new convolution kernel via a modification of the B^* coefficient

$$B^* = \frac{Re^{\log_{10}\left(\frac{15.29}{Re^{0.0567}}\right)}}{12.86}, \tag{105}$$

which appear seemingly valid over a wider range of Reynolds numbers, i.e $Re \in [2 \cdot 10^3, 10^8]$. Ref. [118] gives a final answer in order to take pipe's roughness into account. It is noteworthy discussing [117, 119, 118]'s assumptions. The authors indeed supposed that the idealize turbulent eddy viscosity profile does not instantaneously respond to the mean flow variations. Quoting the authors: "*The change in the effective viscosity occurs during the period when the shape of the velocity profile is changing, not during the earlier period when the velocity amplitude increases uniformly. That is, there is a phase lag between the step change in mean velocity and the resulting change in the effective viscosity.*" This assumption is known in this literature as the "*frozen viscosity*" model and has been later-on analyzed by [120, 118, 13]. [120, 119, 118, 13] confirmed the relevance of the "*frozen viscosity*" approach as long as the shear pulse diffusion through the viscous sub-layer time scale, i.e. $\tau_{diff,sublayer} \equiv \frac{\sqrt{2}R_0}{u_*}$ with $u_*^2 = \frac{f_{DW} W_0^2}{8}$ the friction velocity, is smaller than the advective wave time scale, i.e. $\tau_{adv} \equiv \frac{L^*}{c_p^*}$. A validity condition then follows

$$\frac{4R_0 c_p}{\sqrt{f_{DW}} L W_0} \gg 1, \tag{106}$$

or otherwise, invoking the definition of δ and δ_{st} in (92) and (98), respectively

$$\delta^2 \ll \sqrt{f_{DW}}\delta_{st}, \tag{107}$$

It obviously follows from the condition (107), that it should not be expected close agreement between the [117, 119] model predictions and the experimental data, for observation times upper than $\tau_{diff,subayer}$. To test these models, comparisons between theoretical/semi-empirical predictions and experimental data were carried out in [98]. The authors found excellent agreement for all the models herein presented. Other experimental validations were carried-out in [122, 99]. [122, 99] performed a series of experiments in an elastic copper pipe of length $L = 98m$, inner radius $R_0 = 8 \cdot 10^{-3}m$

Friction Model Category	Model Name	Equation
Steady and quasisteady friction	Darcy Weisbach	$f_s = \frac{8fL}{\pi^2 g D^5} Q^2$
Instantaneous mean flow velocity	Hino	$f_u = 0.188 \left(V \sqrt{\frac{4L}{v\pi a}} \right)^{-\frac{1}{2.85}}$
Instantaneous mean flow velocity and local acceleration	Daily	$\frac{f_u}{f_s} = 1 + c_2 \frac{2D}{f_s V^2} \frac{dV}{dt}$
Instantaneous mean flow velocity, local acceleration, and convective acceleration	Brunone	$f_u = \frac{kD}{V\|V\|} \left(\frac{\partial V}{\partial t} - a \frac{\partial V}{\partial x} \right)$
Instantaneous mean flow velocity, local acceleration, and convective acceleration	Vítkovský	$f_u = \frac{kD}{V\|V\|} \left(\frac{\partial V}{\partial t} - a.sign(V) \left\| \frac{\partial V}{\partial x} \right\| \right)$
Instantaneous mean flow velocity and past velocity changes weights	Convolutional model	$f_u = \frac{16\mu}{\rho D^2 A} \left(\frac{\partial Q}{\partial t} * W(\tau) \right)$
	Vardy and Brown weighting function	$W(\tau) = \frac{A^{\times} e^{-B^{\times}\tau}}{\sqrt{\tau}}$

Figure 11: Friction coefficient f_u, i.e. $\tau_{tr} \equiv \frac{\rho_f f_u W|W|}{4}$ for the characterization of transient overpressure waves damping in pipes. Original chart of [121].

and wall thickness $e = 10^{-3} m$ for a wide Reynolds number range, $R_e \in [1100, 15800]$. Despite their conclusions merge those of [98], they highlighted that (WFB) models: "*have to be singled out. These models predict almost superbly the wave front shape and preserve the frequency. However, it is symptomatic that for higher Reynolds number (over approx* 10^5*) the damping effect observed in the calculated courses is greater than in the experimental ones*". An observation also shared recently by [123, 124]. An overview of all damping models can be gathered from the work of [121] from which Figure 11 has been taken.

Beside pipe wall's boundary-layer related damping models, some analysis suggest that acoustic impedance discontinuities might also affect the phase as well as the damping of water-hammer waves [70, 111]. How to handle and model the wave interaction nearby discontinuities is still under debate [70, 111] and many possible improvements are suggested from a huge acoustic literature that this review does not cover. However, a recent asymptotic analysis [112] in complex geometries might help improving long-wavelength approximation models when impedance discontinuities have to be taken into account.

Finally, it is worth mentioning that despite of all these modeling efforts, water-hammer friction models, are yet only partially successful when confronted with experimental observations. One possible explanation — maybe an optative one— is that

some issues might have been missed. As mentioned earlier, some researches evoked the possible influence of turbulence [106, 117] of the "steady" flow to influence the water-hammer wave friction propagating through it. Also, at the roots of the quasi-steady Darcy-Weisbach approximation (84) is a coupling between the water-hammer wave and the steady flow underneath. In both cases, the friction model depends on the coupling arising between the steady base flow and water-hammer wave, but, to our knowledge, the mechanical origin of this coupling has not been clearly elucidated yet. A possible path toward clarifying this issue will be described in section 4.2 where a recent asymptotic study is discussed.

3. Poisson coupling in more complex contexts

3.1. More complex vibrating degree of freedom

I should be pointed out that, depending on the system's Degree Of Freedom (DOF), several additional vibrations must be taken into account (e.g. torsion, bending etc.). The recent reviews of [15, 17] provide insights into this modeling when all pipe's DOF are considered, leading to an increasingly larger number of equations (e.g eight DOF leads to sixteen coupled equations [17]). Obviously, in this context of extended DOF analysis, only very simple pipe's configurations have been considered without taking into account friction coupling.

3.2. Visco-elastic FSI effects

Water hammer pressure waves propagating into liquid filled pipes having visco-elastic solid walls experience a strong attenuation both in hydraulic contexts [88] as well as bio-mechanical ones [125, 126, 127, 128, 18]. By the last quarter of the twentieth century, Rieutord et al. [129] demonstrated that visco-elastic stress-strain response of a pipe wall has a strong influence on the water-hammer waves propagation. A few years later some experiments from the same team [130] complemented with a 1D theoretical model [131] confirmed their first observations supported by a theoretical understanding of it. As opposed to the case of a purely elastic solid, when considering a visco-elastic wall, the water-hammer wave velocity becomes dispersive [125, 40, 132], i e, the wave velocity depends on the considered frequency. Secondly, the wave amplitude is exponentially damped because the wave velocity acquires an imaginary component coming from visco-elastic dissipation [133, 31, 104, 134]. Both

damping and dispersivity are related to the creep-functions J^* defined as the strain to stress ratio. More precisely considering the normal stress σ^*_{rr} and the longitudinal deformation ξ^*,

$$J^* = \frac{\epsilon^*_{rr}}{\sigma^*_{rr}} \equiv \frac{\partial_r \xi^*}{\sigma^*_{rr}} \equiv \frac{1}{E^*}, \tag{108}$$

where the strain tensor $\boldsymbol{\epsilon}^*$ and displacement gradients are related by

$$\boldsymbol{\epsilon}^* = \frac{1}{2}\left(\boldsymbol{\nabla}^* \boldsymbol{\xi}^* + \boldsymbol{\nabla}^{*T} \boldsymbol{\xi}^*\right). \tag{109}$$

A similar exponential damping is also present in water-hammer wave propagation within purely elastic pipes as discussed in 2.3. Nevertheless it results from a very distinct mechanism associated with the viscous dissipation within boundary layers [95, 135]. In many cases however, the visco-elastic damping dominates over the viscous one. This visco-elastic damping is filtering high-frequency oscillating elastic modes. Since water-hammer wave propagation has been found material dependent, the pioneering studies of [129, 130, 131] inspired many others, following the similar footsteps, combining experimental measurements with modeling associated with solid creep-functions displaying Kelvin-Voigt behavior (Cf [136, 137, 31, 104, 138] among many others). The applicative interest and the relevance of the topic motivated many further studies whereby one could enrich the Kelvin-Voigt model [139, 140] to better fit with observations. Alternatively, some authors also included both solid visco-elastic damping and fluid one, through time-convolution, shear-stress models [141, 142, 143]. Because the modelling relies on many parameters, combined with time-convolution many approaches are possible to match experiments raising a number of questions including wave-speed calibration in visco-elastic pipes [138, 144]. The influence of the visco-elastic stress response has been more recently considered in a Fluid-Structure-Interaction (FSI) context as more extensively discussed in the recent review of [15]. In this context Kelvin-Voigt solid responses of the creep function have also been used in FSI four-equations models [145, 146, 147] in order to improve the relevance of the modeling. Furthermore, for improving data fitting, a series of Kelvin-Voigt units are often considered [145, 148, 146, 147]. However, in these previous modeling efforts, the creep-function parameters are calibrated [149] not only to describe the visco-elastic properties of the solid but also the considered pipe configuration associated with a specific length, thickness, diameter and boundary conditions. Let us now first discuss in more details visco-elastic models without FSI effects.

3.2.1. Two-equations water hammer models within visco-elastic pipes

When considering an acoustic fluid region whilst disregarding the influence of viscous boundary layer, the dimensionless low-Mach, long-wavelength mass conservation and momentum balance in the core fluid region (the outer region of the asymptotic framework) leads to the following two-equation hyperbolic problem [149, 43, 135, 65]

$$\partial_\tau P + \mathcal{C}^2 \partial_Z W = -2\alpha \mathcal{C}^2 \partial_\tau \xi\big|_{R=1}, \tag{110}$$

$$\partial_\tau W = -\partial_Z P. \tag{111}$$

In (110)-(111), as used in (38) a Joukowsky's dimensionless pressure is chosen, i.e $P^* = (\rho_f c_p^* W^*)P$, built upon reference steady fluid velocity W^*, also used for dimensionless velocity W defined as $w^* = W^* W$. As in section 2.2.1 dimensionless time is again based upon wave traveling reference time, i.e $t^* = (L/c_p^*)\tau$, associated with the pulsed wave-speed c_p^* and longitudinal reference length L^*, also used for dimensionless longitudinal length $Z^* = L^* Z$. Finally the dimensionless longitudinal solid displacement $\xi^* = \xi_0^* \xi$ is related to a reference length $\xi_0^* = R_0^* \alpha W^*/c_p^*$ the origin of which comes from kinematic boundary conditions [135]. From the r.h.s of (110) and the long-wavelength approximation, continuity relations of the radial velocity at the wall $\partial_\tau \xi\big|_{R=1}$ is automatically satisfied. The dimensional version of (110)'s r.h.s was derived from Reynolds transport theorem using (30) in section 2.1 as resulting from a kinematic driven FSI coupling. Writing (110)-(111) in Fourier space leads to

$$i\omega \tilde{P} + \mathcal{C}^2 \partial_Z \tilde{W} = -2i\alpha\omega \mathcal{C}^2 \tilde{\xi}\big|_{R=1}, \tag{112}$$

$$i\omega \tilde{W} = -\partial_Z \tilde{P}. \tag{113}$$

These equations are complemented with Fluid/Solid interface boundary conditions. To express them, one first needs to define the linear constitutive relation between the solid stress tensor $\boldsymbol{\sigma}^*$ and strain tensor $\boldsymbol{\epsilon}^*$. In frequency domain and dimensional form, these constitutive visco-elastic solid equations read

$$\tilde{\boldsymbol{\sigma}}^* = \tilde{\lambda}_s^*(\omega^*)\mathrm{Tr}\left(\tilde{\boldsymbol{\epsilon}}^*\right)\mathbf{I} + 2\tilde{\mu}_s^*(\omega^*)\tilde{\boldsymbol{\epsilon}}^* \quad \text{, with, } \tilde{\boldsymbol{\epsilon}}^* = \frac{1}{2}\left(\boldsymbol{\nabla}^* \tilde{\boldsymbol{\xi}}^* + \boldsymbol{\nabla}^{*\,\mathrm{T}} \tilde{\boldsymbol{\xi}}^*\right). \tag{114}$$

where $\mathrm{Tr}\left(\tilde{\boldsymbol{\epsilon}}^*\right) = \boldsymbol{\nabla}^* \cdot \tilde{\boldsymbol{\xi}}^*$ is the trace of tensor $\tilde{\boldsymbol{\epsilon}}^*$ which also equals the divergence of the displacement vector. $\tilde{\lambda}_s^*(\omega^*)$ and $\tilde{\mu}_s^*(\omega^*)$ are the generalized Lamé coefficients, dependent on pulsation ω^*. These coefficients are usually found experimentally from using Dynamic Mechanical Analysis (DMA) measurements). Since dimensionless formulations are better for comparing various models in the same reference framework,

609 the Joukowsky pressure is used as a reference pressure, for dimensionless stress ten-
610 sor $\boldsymbol{\sigma}^* = \rho_f c_p^* W^* \boldsymbol{\sigma}$. Each Lamé coefficient is made dimensionless using the Young
611 modulus, $(\lambda_e^*, \mu_e^*) = E^*(\lambda_e, \mu_e)$, so that in dimensionless form, frequency domain and
612 cylindrical coordinates the visco-elastic equation (114) reads

$$\tilde{\sigma}_{rr} = \alpha \left[\frac{2}{\tilde{\mathcal{C}}_{\mu_s}(\omega)} + \frac{1}{\tilde{\mathcal{C}}_{\lambda_s}(\omega)} \right] \partial_R \tilde{\xi} + \frac{\alpha}{\tilde{\mathcal{C}}_{\lambda_s}(\omega)} \left[\partial_Z \tilde{\zeta} + \frac{\tilde{\xi}}{R} \right], \quad (115)$$

$$\tilde{\sigma}_{\theta\theta} = \alpha \left[\frac{2}{\tilde{\mathcal{C}}_{\mu_s}(\omega)} + \frac{1}{\tilde{\mathcal{C}}_{\lambda_s}(\omega)} \right] \frac{\tilde{\xi}}{R} + \frac{\alpha}{\tilde{\mathcal{C}}_{\lambda_s}(\omega)} \left[\partial_Z \tilde{\zeta} + \partial_R \tilde{\xi} \right], \quad (116)$$

$$\tilde{\sigma}_{zz} = \alpha \left[\frac{2}{\tilde{\mathcal{C}}_{\mu_s}(\omega)} + \frac{1}{\tilde{\mathcal{C}}_{\lambda_s}(\omega)} \right] \partial_Z \tilde{\zeta} + \frac{\alpha}{\tilde{\mathcal{C}}_{\lambda_s}(\omega)} \frac{\partial_R}{R} \left(R\tilde{\xi} \right), \quad (117)$$

$$\epsilon^2 \frac{\tilde{\mathcal{C}}_{\mu_s}(\omega)}{\alpha} \tilde{\sigma}_{rz} = \partial_R \tilde{\zeta} + \epsilon^2 \partial_Z \tilde{\xi}, \quad (118)$$

Ignoring external constraints applied in the solid radial direction (supposing a zero external normal stress) whilst using $\tilde{\sigma}_{rr}$ defined in (115), the continuity of the normal and tangential stress as well as axial velocity read (Cf [65] for more details)

$$\tilde{\sigma}_{rr} = -\tilde{P} \ \text{, at} \ R = 1 \qquad \tilde{\sigma}_{rr} = 0 \ \text{, at} \ R = 1 + \alpha \quad (119)$$

$$\tilde{\sigma}_{rz} = 0 \ \text{, at} \ R = 1 \qquad \tilde{\sigma}_{rz} = 0 \ \text{, at} \ R = 1 + \alpha \quad (120)$$

Note that, for dimensionless radial distance r, since the dimensionless thickness of the pipe is α, the outer wall is reached as $R = 1 + \alpha$. Kinematic condition between the solid and the fluid at $R = 1$ in Fourier space read

$$\tilde{w} = \alpha i\omega \tilde{\zeta}\big|_{R=1} \qquad \tilde{u} = \alpha i\omega \tilde{\xi}\big|_{R=1} \quad (121)$$

It is noteworthy to mention that, the dimensionless form of the two-equation model proposed by Covas et al. [31] reads

$$i\omega \tilde{P} + \partial_Z \tilde{W} = -\frac{2\mathcal{D}}{\alpha \mathcal{C}_s^{e\,2}} i\omega \tilde{\mathcal{I}}_{Cov} \tilde{P}, \quad (122)$$

$$i\omega \tilde{W} = -\partial_Z \tilde{P}, \quad (123)$$

$$(124)$$

613 having the very same terms as (112)-(113) but for introducing the creep function $\tilde{\mathcal{I}}_{Cov}$
614 in the r.h.s term of (122). Using the relation between normal stress and pressure
615 obtained from normal-stress continuity boundary condition (119), since the normal
616 displacement $\tilde{\xi}\big|_{R=1}$ in (112) is linearly related with the radial velocity of (121) which
617 is also linearly related to the normal stress, and thus to the wall pressure, the r.h.s

term of (122) can be interpreted as resulting from some FSI effect. This is why the full FSI problem is now considered.

3.2.2. Four-equations water hammer models within visco-elastic pipes

The dimensionless form of the four-equation model proposed by Keramat et al. [145] is (the dimensionless formulation of this model is derived in [135]'s Appendix)

$$i\omega\tilde{W} = -\partial_Z\tilde{P}, \tag{125}$$

$$i\omega\tilde{P} + \partial_Z\tilde{W} - 2i\omega\alpha\nu_e\partial_Z\tilde{\zeta} = -\frac{2\mathcal{D}\left(1-\nu_e^2\right)}{\alpha\mathcal{C}_s^{e\,2}}i\omega\tilde{\mathcal{I}}_{Ker}\tilde{P}, \tag{126}$$

$$i\omega\tilde{\sigma}_{zz} - i\omega\frac{\nu_e}{\alpha}\tilde{P} - i\omega\frac{\alpha\mathcal{C}_s^{e\,2}}{\mathcal{D}}\partial_Z\tilde{\zeta} = -i\omega\tilde{\mathcal{I}}_{ker}\tilde{\sigma}_{zz} + \frac{\nu_e}{\alpha}i\omega\tilde{\mathcal{I}}_{Ker}\tilde{P}, \tag{127}$$

$$\frac{\alpha}{\mathcal{D}}\omega^2\tilde{\zeta} + \partial_Z\tilde{\sigma}_{zz} = 0, \tag{128}$$

where $\tilde{\mathcal{I}}_{Ker}$ is the Fourier transform of kernels proposed in Keramat et al. [145]). The Covas et al. [31]'s model can be derived in the $\nu_e \to 0$ limit of the Keramat et al. [145]'s one resulting in decoupling fluid axial dynamics to the solid's one. Nevertheless, it is important to stress that, in this limit the right-hand-side of (122) is non-zero, resulting from kinematic continuity condition which produces a FSI term into (112) already found in Skalak's model (24), as previously mentioned. Both [31] and [145] then consider N_{kv} Kelvin-Voigt elements to build their convolution kernel interpreted as a creeping law, each having its own exponential times-decay τ_k, amplitudes J_k, to model their convolution kernels, [148]

$$\left(\tilde{\mathcal{I}}_{Cov}, \tilde{\mathcal{I}}_{Ker}\right) = \sum_{k=1}^{N_{kv}} \frac{E_e J_k}{1 + i\omega\frac{c_p^e\tau_k}{L}}. \tag{129}$$

3.2.3. Generalized 3D visco-elastic rheology

Various Kelvin-Voigt models have been previously considered in the literature [150, 149, 139, 140, 141, 146]. Nevertheless among those almost every model has used a 1D scalar relationship between the stress and the strain. However, general visco-elastic Kelvin-Voigt models can be formulated in 3D as provided by [151] for the stress-strain relation

$$\boldsymbol{\sigma}^* = \lambda_e^*\left(1+\tau_\lambda\partial_{t^*}\right)\left(\boldsymbol{\nabla}^*\cdot\boldsymbol{\xi}\right)\mathbf{I} + \mu_e^*\left(1+\tau_\mu\partial_{t^*}\right)\left(\boldsymbol{\nabla}^*\boldsymbol{\xi}^* + \boldsymbol{\nabla}^{*T}\boldsymbol{\xi}^*\right), \tag{130}$$

having four parameters : two elastic Lamé coefficients λ_e^*, μ_e^* and two visco-elastic times τ_λ, τ_μ. A more general 3D visco-elastic rheology can be formulated [135]

$$a\left(1+\tau_r\partial_{t^*}\right)\boldsymbol{\sigma}^* = \lambda_e^*\left(1+\tau_\lambda\partial_{t^*}\right)\left(\boldsymbol{\nabla}^*\cdot\boldsymbol{\xi}^*\right)\mathbf{I} + \mu_e^*\left(1+\tau_\mu\partial_{t^*}\right)\left(\boldsymbol{\nabla}^*\boldsymbol{\xi}^* + \boldsymbol{\nabla}^{*T}\boldsymbol{\xi}^*\right), \tag{131}$$

where now, six constitutive parameters $a, \tau_r, \tau_\lambda, \tau_\mu, \lambda_e^*, \mu_e^*$ are considered, with again (λ_e^*, μ_e^*) the elastic Lamé coefficients and $(\tau_r, \tau_\lambda, \tau_\mu)$ visco-elastic characteristic times, all independent of frequency ω^*. (131) general visco-elastic rheology encapsulates all previous models used in the context of water-hammer analysis [126, 134, 152, 153, 154, 155, 156], as detailed in table 1. Among those parameters a might be chosen equal to one if the elastic part of the visco-elastic response match with the purely elastic one, since $1/a$ essentially appears as a visco-elastic rescaling of elastic parameters λ_e^* and μ_e^*. Now, from the Fourier transform of (131) and identification with (114) the

	a	τ_r	λ_e^*	τ_λ	μ_e^*	τ_μ
Carcione et al. [152]			✓	✓	✓	✓
Eringen, Canic et al.[153, 126]			✓	✓	✓	✓
Kisilova et al. [134]		✓			✓	✓
Bland [154]			✓		✓	
Ieşan [155]			✓	✓	✓	✓
Sharma et al. [156]			✓	✓	✓	✓

Table 1: Comparative table of 3D rheological parameters taken from literature.

generalized Lamé coefficients can be deduced for this rheology

$$\tilde{\lambda}_s^*(\omega^*) = \lambda_e^*\frac{1+i\omega^*\tau_\lambda}{a\left(1+i\omega^*\tau_r\right)} \quad \text{, and} \quad \tilde{\mu}_s^*(\omega^*) = \mu_e^*\frac{1+i\omega^*\tau_\mu}{a\left(1+i\omega^*\tau_r\right)}. \tag{132}$$

Generalized Poisson and Young modulus can also be found from these rheological parameters

$$\tilde{\nu}_s^*\left(\omega^*\right) = \nu_e\frac{1+i\omega^*\tau_\lambda}{1+i\omega^*\tau_\nu} \quad \text{, and} \quad \tilde{E}_s^*\left(\omega^*\right) = \frac{E_e(1+i\omega^*\tau_\mu)(1+i\omega^*\tau_E)}{a(1+i\omega^*\tau_r)(1+i\omega^*\tau_\nu)}, \tag{133}$$

where the above introduced times-scale τ_ν and τ_E are given by

$$\tau_\nu = \frac{\lambda_e\tau_\lambda + \mu_e\tau_\mu}{\lambda_e+\mu_e} \quad \text{, and} \quad \tau_E = \frac{3\lambda_e\tau_\lambda + 2\mu_e\tau_\mu}{3\lambda_e+2\mu_e}. \tag{134}$$

In the following the dimensionless generalized Lamé coefficients are defined,

$$\tilde{\lambda}_s^*(\omega^*) = \tilde{\lambda}(\omega^*)\lambda_e^* \quad \text{, and} \quad \tilde{\mu}_s^*(\omega^*) = \tilde{\mu}_s(\omega^*)\mu_e^*, \tag{135}$$

as well as the dimensionless generalized Poisson and Young modulus

$$\tilde{\nu}_s^*(\omega^*) = \tilde{\nu}_s(\omega^*)\,\nu_e \quad \text{, and} \quad \tilde{E}_s^*(\omega^*) = E_e\tilde{E}_s(\omega^*). \tag{136}$$

Also, the Fourier transform of the dimensionless creep function $\tilde{J}_s(\omega)$ (108) reads from (136)

$$\tilde{J}_s(\omega) = \frac{1}{\tilde{E}_s} = a\frac{\left(1+i\omega\tau_r\frac{c_p}{L}\right)\left(1+i\omega\tau_\nu\frac{c_p}{L}\right)}{\left(1+i\omega\tau_\mu\frac{c_p}{L}\right)\left(1+i\omega\tau_E\frac{c_p}{L}\right)}. \tag{137}$$

where dimensionless frequency ω is related to the dimensional one $\omega^* = \omega c_p/L$ using the advective time-scale L/c_p.

3.3. FSI Rheology-based four-equations dimensionless visco-elastic water-hammer

In [135], a rheology-based four-equations FSI model has been derived from the general visco-elastic rheology (131) hereby presented in dimensionless form

$$\begin{aligned}
i\omega\tilde{P} + \partial_Z\tilde{W} - 2i\omega\alpha\nu_e\partial_Z\tilde{\zeta} &= -i\omega\chi_e\tilde{\mathcal{I}}_P^F\tilde{P} + \frac{2\mathcal{D}\nu_e}{\mathcal{C}_s^{e2}}i\omega\tilde{\mathcal{I}}_\sigma^F\tilde{\sigma}_{zz}, && (138)\\
i\omega\tilde{W} &= -\partial_Z\tilde{P} && (139)\\
i\omega\tilde{\sigma}_{zz} - \frac{2\nu_e}{\alpha(2+\alpha)}i\omega\tilde{P} - i\omega\frac{\alpha\mathcal{C}_s^{e2}}{\mathcal{D}}\partial_Z\tilde{\zeta} &= -i\omega\tilde{\mathcal{I}}_\sigma^S\tilde{\sigma}_{zz} + \frac{2\nu_e}{\alpha(2+\alpha)}i\omega\tilde{\mathcal{I}}_P^S\tilde{P}, && (140)\\
\frac{\alpha}{\mathcal{D}}\omega^2\tilde{\zeta} + \partial_Z\tilde{\sigma}_{zz} &= 0, && (141)
\end{aligned}$$

where the hereby introduced visco-elastic extra terms $\tilde{\mathcal{I}}_P^F$, $\tilde{\mathcal{I}}_\sigma^F$, $\tilde{\mathcal{I}}_P^S$ and $\tilde{\mathcal{I}}_\sigma^S$ read

$$\begin{aligned}
\tilde{\mathcal{I}}_P^F &= \frac{1}{\tilde{E}_s(\omega)}\frac{1-\nu_e^2\tilde{\nu}_s(\omega)+\frac{\alpha(2+\alpha)}{2}(1+\nu_e\tilde{\nu}_s(\omega))}{1-\nu_e^2+\frac{\alpha(2+\alpha)}{2}(1+\nu_e)} - 1, && (142)\\
\tilde{\mathcal{I}}_\sigma^F &= \frac{\tilde{\nu}_s(\omega)-1}{\tilde{E}_s(\omega)}, && (143)\\
\tilde{\mathcal{I}}_P^S &= -\left(1-\frac{\tilde{\nu}_s(\omega)}{\tilde{E}(\omega)}\right), && (144)\\
\tilde{\mathcal{I}}_\sigma^S &= \frac{1-\tilde{E}_s(\omega)}{\tilde{E}_s(\omega)}. && (145)
\end{aligned}$$

It is important to stress the similarity between (138)-(141)'s model and Keramat et al. [31, 145]'s ones. Considering [145]'s hypothesis that the generalized Young modulus ν_s^* equals the elastic one ν_e, i.e. $\tilde{\nu}_s = 1$, with small dimensionless tube's thickness i.e. $\alpha \ll 1$, visco-elastic kernels (142)-(145) simplify to

$$\tilde{\mathcal{I}}_P^F = \tilde{\mathcal{I}}_P^S = \tilde{\mathcal{I}}_\sigma^S = \tilde{J}_s(\omega) - 1 \quad \text{, and} \quad \tilde{\mathcal{I}}_\sigma^F = 0. \tag{146}$$

As a matter of fact within $\tilde{\nu}_s = 1$ ($\tilde{\nu}_s^* = \nu_e$) and $\alpha \to 0$ hypothesis, one finds that the r.h.s of (139) displays a convolution product with the pressure only, as (126) when $\mathcal{I}_\sigma^F = 0$ as provided by (146). Furthermore, the kernel associated with $\tilde{\mathcal{I}}_P^F$, $\tilde{\mathcal{I}}_P^S$ and $\tilde{\mathcal{I}}_\sigma^S$ is the same, so that both r.h.s terms of (140) share the same kernel respectively applied to the pressure and the axial stress. The very same feature is satisfied by the r.h.s of (127). Hence, the visco-elastic rheological based model (138)-(141) is similar with Keramat et al. (2011) (125)-(128) when using the $\tilde{\nu}_s = 1$ and $\alpha \to 0$ i.e, in the limit of thin-wall and without visco-elastic contribution to the Poisson coupling, the [135]'s model directly matches with [31, 145] provided by the explicit rheology-based creep-function familly (137). In the more general case $\tilde{\nu}_s \neq 1$, [135] gives explicit derivations of visco-elastic extra-terms versus rheological parameters reading

$$\tilde{\mathcal{I}}_P^F = a\frac{\left(1+i\omega\frac{\tau_r}{t_c}\right)\left(1+i\omega\frac{\tau_\nu}{t_c}\right)}{\left(1+i\omega\frac{\tau_\mu}{t_c}\right)\left(1+i\omega\frac{\tau_E}{t_c}\right)}\frac{\nu_e^2\frac{1+i\omega\frac{\tau_\lambda}{t_c}}{1+i\omega\frac{\tau_\nu}{t_c}} - 1 - \frac{\alpha(2+\alpha)}{2}\left(1+\nu_e\frac{1+i\omega\frac{\tau_\lambda}{t_c}}{1+i\omega\frac{\tau_\nu}{t_c}}\right)}{\nu_e^2 - 1 - \frac{\alpha(2+\alpha)}{2}(1+\nu_e)} \quad (147)$$

$$\tilde{\mathcal{I}}_\sigma^F = a\frac{\left(1+i\omega\frac{\tau_r}{t_c}\right)\left(1+i\omega\frac{\tau_\nu}{t_c}\right)}{\left(1+i\omega\frac{\tau_\mu}{t_c}\right)\left(1+i\omega\frac{\tau_E}{t_c}\right)}\left(\frac{1+i\omega\frac{\tau_\lambda}{t_c}}{1+i\omega\frac{\tau_\nu}{t_c}} - 1\right), \quad (148)$$

$$\tilde{\mathcal{I}}_P^S = -\left(1 - a\frac{\left(1+i\omega\frac{\tau_r}{t_c}\right)\left(1+\omega\frac{\tau_\lambda}{t_c}\right)}{\left(1+i\omega\frac{\tau_\nu}{t_c}\right)\left(1+i\omega\frac{\tau_E}{t_c}\right)}\right), \quad (149)$$

$$\tilde{\mathcal{I}}_\sigma^S = -\left(1 - a\frac{\left(1+i\omega\frac{\tau_r}{t_c}\right)\left(1+i\omega\frac{\tau_\nu}{t_c}\right)}{\left(1+i\omega\frac{\tau_\mu}{t_c}\right)\left(1+i\omega\frac{\tau_E}{t_c}\right)}\right). \quad (150)$$

where, again the convective time-scale is defined as $t_c = L/c_p$. As previously considered in (39) the wave system resulting from the visco-elastic FSI four equations hyperbolic problem (138)-(141) can thus be recast into two coupled waves for the two-component pressure/stress vector $\tilde{\mathbf{P}} \equiv [\tilde{P}, \tilde{\sigma}_{zz}]$ following [65]

$$\omega^2\tilde{\mathbf{P}} + [\tilde{c}_p^v]^2\begin{pmatrix} 1 & 2\nu_e\mathcal{D}\frac{1+\tilde{\mathcal{I}}_\sigma^S+\tilde{\mathcal{I}}_\sigma^F}{1+\tilde{\mathcal{I}}_\sigma^S} \\ \frac{2\nu_e}{\alpha(2+\alpha)}\frac{1+\tilde{\mathcal{I}}_P^S}{1+\tilde{\mathcal{I}}_\sigma^S} & \mathcal{C}_s^{e\,2}\frac{1+\chi_e\tilde{\mathcal{I}}_P^F}{1+\tilde{\mathcal{I}}_\sigma^S} + \frac{4\nu_e^2\mathcal{D}}{\alpha(2+\alpha)}\frac{1+\tilde{\mathcal{I}}_P^S}{1+\tilde{\mathcal{I}}_\sigma^S} \end{pmatrix}\partial_Z^2\tilde{\mathbf{P}} = \mathbf{0}. \quad (151)$$

The characteristic equation associated with this propagating operator is

$$\left(\frac{\tilde{c}_\pm}{\tilde{c}_p^v}\right)^4 - \left(\frac{\tilde{c}_\pm}{\tilde{c}_p^v}\right)^2\left[1 + \mathcal{C}_s^{e\,2}\frac{1+\chi_e\tilde{\mathcal{I}}_P^F}{1+\tilde{\mathcal{I}}_\sigma^S} + \frac{4\nu_e^2\mathcal{D}}{\alpha(2+\alpha)}\frac{1+\tilde{\mathcal{I}}_P^S}{1+\tilde{\mathcal{I}}_\sigma^S}\right] + \mathcal{C}_s^{e\,2}\frac{1+\chi_e\tilde{\mathcal{I}}_P^F}{1+\tilde{\mathcal{I}}_\sigma^S} + \frac{4\nu_e^2\mathcal{D}}{\alpha(2+\alpha)}\frac{1+\tilde{\mathcal{I}}_P^S}{1+\tilde{\mathcal{I}}_\sigma^S}\left(1 - \frac{1+\tilde{\mathcal{I}}_\sigma^S+\tilde{\mathcal{I}}_\sigma^F}{1+\tilde{\mathcal{I}}_\sigma^S}\right) = 0, \quad (152)$$

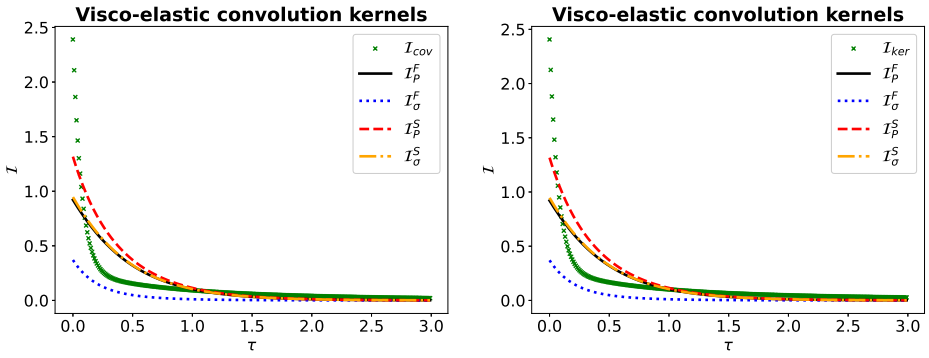

(a) (b)

Figure 12: Comparison to (a) Covas et al. [31]'s and (b) Keramat et al. [145]'s visco-elastic convolution kernels for the experimental data of Covas et al. [137, 31]. Dimensionless time $\tau = t^* c^*_{p,T}/L^*$ has been used.

where the effective frequency-dependent corrective visco-elastic phase velocity $\tilde{c}_p^v(\omega)$ found in [135] is

$$\tilde{c}_p^v(\omega) = \frac{1}{\sqrt{1+\chi_e \tilde{\mathcal{I}}_P^F - \frac{4\mathcal{D}\nu_e^2}{\alpha(2+\alpha)\mathcal{C}_s^{e\,2}}\tilde{\mathcal{I}}_\sigma^F \frac{1+\tilde{\mathcal{I}}_P^S}{1+\tilde{\mathcal{I}}_\sigma^S}}}. \tag{153}$$

The root of (152) can be found, generalyzing (42) to a general visco-elastic rheology

$$\tilde{c}_\pm^2 = [\tilde{c}_p^v]^2 \frac{\hat{c} \pm \sqrt{\hat{c}^2 - 4\left[\mathcal{C}_s^{e\,2}\frac{1+\chi_e\tilde{\mathcal{I}}_P^F}{1+\tilde{\mathcal{I}}_\sigma^S} + \frac{4\nu_e^2\mathcal{D}}{\alpha(2+\alpha)}\frac{1+\tilde{\mathcal{I}}_P^S}{1+\tilde{\mathcal{I}}_\sigma^S}\left(1 - \frac{1+\tilde{\mathcal{I}}_\sigma^S+\tilde{\mathcal{I}}_\sigma^F}{1+\tilde{\mathcal{I}}_\sigma^S}\right)\right]}}{2}, \tag{154}$$

$$\hat{c} = 1 + \mathcal{C}_s^{e\,2}\frac{1+\chi_e\tilde{\mathcal{I}}_P^F}{1+\tilde{\mathcal{I}}_\sigma^S} + \frac{4\nu_e^2\mathcal{D}}{\alpha(2+\alpha)}\frac{1+\tilde{\mathcal{I}}_P^S}{1+\tilde{\mathcal{I}}_\sigma^S} \equiv \frac{\tilde{c}_+^2 + \tilde{c}_-^2}{[\tilde{c}_p^v]^2}. \tag{155}$$

The various visco-elastic convolution kernels are compared in Figure 12 for the experimental data of [31] presented in Table 2. Figure 13 shows the least-squares difference fitting of the pressure solution (151) obtained in [65]. Even though in each case a fitting of the pressure signal is performed, it is nice to observe that the various models [31], [145] or [65] do not perform alike, in this fitting. This is expected since both the model and the fitting parameters differ. From the rheological fitting on the pressure signal, the visco-elastic kernels can be compared. Even though these kernel families present similar exponential decay types, $\tilde{\mathcal{I}}_{Cov}$ and $\tilde{\mathcal{I}}_{Ker}$ display faster attenuation than the various kernels $\mathcal{I}_P^F, \mathcal{I}_\sigma^F, \mathcal{I}_P^S, \mathcal{I}_\sigma^S$ of [65] as can be observed in Fig 14c. Also, both $\mathcal{I}_P^F$ and $\mathcal{I}_\sigma^S$ are very similar for the obtained visco-elastic parameters. Concerning the

velocity dispersivity prediction provided in Figure 14, one should note that every model displays a similar trend for the norm of complex velocities: it varies from a minimum value at $\omega = 0$ within a narrow low-frequency region (associated with a long time behaviour) so as to reach a constant plateau for large $|\omega|$ values.

Hence, at short-time/large $|\omega|$ most dispersivity of the wave velocity is lost and the visco-elastic response is very much like the elastic one, [157, 158]. This allows to define a 'dispersive' frequency gap band depicted within vertical orange dotted lines for which visco-elastic effects are important. The 'dispersive' frequency gap band $\Delta\omega_v$ is more precisely defined as the 95% difference velocity region from the asymptotic high-frequency regime, as exemplified in the inset of figure 14a. The larger this dispersive gap-band, and the deeper the $\omega = 0$ velocity, the larger visco-elastic effects are. One can observe in figure 14 that the dispersive gap is wider for Covas et al. [31] and Keramat et al. [145] models than for the hereby model (in black) for parameters obtained from the same data set [137, 31].

4. Recent developments

4.1. Two-time scale asymptotic analysis of water-hammer without FSI

In this section more recent advances obtained from complementing the spatial asymptotic analysis discussed in section 2.3 with a two-time scale asymptotic approach are now presented. Indeed, not only the water-hammer small parameter δ (92) is useful to define the dimensionless size of the wave perturbation boundary layer nearby the solid wall. It is also relevant to define a long-time scale associated with the momentum relaxation within it. More precisely, as provided in (92) since δ is related to the ratio between advection time to viscous relaxation time $\delta^2 = t_c/t_{vis}$, and since, as found by Zielke (95), Vardy (102) or others, the velocity time variations within the boundary layer are controlled by t_{vis}, one realizes that since momentum relaxation within the boundary layer varies as $t/t_{vis} = \delta^2 t/t_c = \delta^2\tau$ when chossing a dimensionless time $\tau = t/t_c$. In other words, the time response of the wave perturbation within the boundary layer is slow compared to the wave advection time. Approximated solutions for water-hammer waves based upon this multi-time scale nature of the water-hammer wave have been developed in several contributions [159, 160, 161, 162, 95, 163]. In the following we will nevertheless first focus on the contribution of Mei & Jing [95] which investigates how a two-time scale perturbation analysis permits to predict the

exponential decay of the wave envelope. Introducing the slow time-scale $T = \delta\tau$ permits to decompose time variations as

$$\partial_{t^*} = \frac{c_p}{L}(\partial_\tau + \delta\partial_T) \tag{156}$$

Either non-FSI or FSI effects can be considered within this multi-time scale approximation approach. Since, the latter requires much involved developments, we first consider the non-FSI problem analyzed in [95] for a single pipe.

An asymptotic solution to the slowly damped pressure wave (83) is set up from evaluating the leading order wall-shear stress associated with damped propagation from solving the undamped problem first. The dimensionless pressure P, velocity W and wall shear-stress $\tau_w \equiv \tau_f|_{R=1}$ are thus asymptotically expanded as

$$P = P^0 + \delta P^1 + \ldots, \quad W = W^0 + \delta W^1 + \ldots, \quad \tau_w = \tau_w^0 + \delta\tau_w^1 + \ldots \tag{157}$$

Using (157) and (156) in (83) provide the leading order undampted problem

$$\left[\partial_\tau^2 - \partial_Z^2\right] P^0 = 0 \tag{158}$$

which is solved together with mixed Dirichlet-Neumann boundary conditions

$$P^0(Z=0) = 0, \quad \tfrac{\partial P^0}{\partial Z}(Z=1) = D(t) \tag{159}$$

where $D(t)$ is a closure law to be specified (and chosen as a triangular shape in [95]), but we will simplify their result to either a general closure $D(t)$ or a Dirac distribution $D(t) \equiv \delta(t)$). In Laplace domain, the solution (158) and (159) is

$$P^0(Z,s) = \frac{\sinh(sZ)}{s\cosh s} D(s) \tag{160}$$

The time-domain solution can either be found from inverse Laplace transform, or direct solution. The time-domain solution for the leading order pressure is reported in [95] for a Dirac distribution closure $D(t) \equiv \delta(t)$, $D(s) = 1$ and reads

$$P^0(Z,t) = 2\sum_{k\in\mathbb{N}} (-1)^k \frac{\sin(\lambda_k Z)}{\lambda_k} \sin(\lambda_k \tau) \quad \& \quad \lambda_k = \pi\left(\frac{1}{2} + k\right). \tag{161}$$

From (161), one realizes that boundary conditions (159) are satisfied. The same result can also be obtained from (158) decomposing the pressure into an homogeneous component having homogeneous boundary conditions, as well as a particular solution dealing with the non-homogeneous r.h.s of (159) with $D(t) \equiv \delta(t)$

$$P^0(Z,t) \quad = \quad P_p^0(Z,t) + P_h^0(Z,t) \ \text{ with, } \ P_p^0(Z,t) = Z\delta(t), \tag{162}$$

In the following, it will be useful to define the spatial orthogonal basis such that

$$\phi_{\lambda_k}(Z) = \sqrt{2}\text{sgn}(\lambda_k)\sin(\lambda_k Z) \quad \& \quad \int_0^1 \phi_{\lambda_k}\phi_{\lambda_{k'}} dZ = \langle \phi_{\lambda_k}, \phi_{\lambda_{k'}} \rangle = \delta_{\lambda_k,\lambda_{k'}} + \delta_{\lambda_k,-\lambda_{k'}}. \tag{163}$$

where $\delta_{\lambda_k,\lambda_{k'}}$ is the Kronecker symbol associated with the equality of λ_k and $\lambda_{k'}$. Given $\lambda_k = \pi\left(\frac{1}{2} + k\right)$ for $k \in \mathbb{Z}$, the resulting $\lambda_k \in \mathbb{R}$ can indeed lead to $\pm\lambda_k$ as possible eigenvalues, and since $\phi_{\lambda_k} = \phi_{-\lambda_k}$ there are indeed two possible non-zero contributions to the base decomposition, i.e $\pm\lambda_k$. Since the Laplace transform of the particular solution defined in (162) is $\tilde{P}_h^0(Z,s) = Z$, it decomposes into the ϕ_{λ_k} base as follows

$$\tilde{P}_p = \frac{1}{2}\sum_{\lambda_k \in \mathbb{R}} \langle Z, \phi_{\lambda_k}\rangle \phi_{\lambda_k}, \quad \& \quad \langle Z, \phi_{\lambda_k}\rangle = \frac{(-1)^k}{\sqrt{2}\lambda_k^2}. \tag{164}$$

Decomposing the Laplace transform of the homogeneous part as

$$\tilde{P}_h^0(Z,s) = \sum_{\lambda_k \in \mathbb{R}} \tilde{a}^0(s)\phi_{\lambda_k}, \tag{165}$$

whilst using (158), (164) and (165) leads to

$$\sum_{\lambda_k \in \mathbb{R}} (s^2 + \lambda_k^2)\tilde{a}^0(s)\phi_{\lambda_k} = -s^2\tilde{P}_p = \frac{-s^2}{2}\sum_{\lambda_k \in \mathbb{R}} \langle Z, \phi_{\lambda_k}\rangle \phi_{\lambda_k}, \tag{166}$$

678 the projection of which over ϕ_{λ_k}, leads to

$$\tilde{a}^0_{\lambda_k}(s) + \tilde{a}^0_{-\lambda_k}(s) = -\frac{s^2}{s^2+\lambda_k^2}\langle Z, \phi_{\lambda_k}\rangle = (\frac{\lambda_k^2}{s^2+\lambda_k^2} - 1)\langle Z, \phi_{\lambda_k}\rangle \tag{167}$$

$$\tilde{a}^0_{\lambda_k}(s) + \tilde{a}^0_{-\lambda_k}(s) = [\frac{\lambda_k}{2i}\left(\frac{1}{s - i\lambda_k} - \frac{1}{s + i\lambda_k}\right) - 1]\langle Z, \phi_{\lambda_k}\rangle \tag{168}$$

so that, given the condition $\tilde{a}^{0\star}_{\lambda_k} = \tilde{a}^0_{-\lambda_k}$ one finds

$$\tilde{a}^0_{\lambda_k} = -\frac{1}{2}[\frac{\pm i\lambda_k}{s \mp \lambda_k} + 1]\langle Z, \phi_{\lambda_k}\rangle. \tag{169}$$

Using the Laplace transform of sinus function $\mathcal{L}(\sin(\lambda_k\tau) = \lambda_k/(s^2+\lambda_k^2)$, (161) can be rewritten using (164) as

$$\tilde{P} = \sum_{k\in\mathbb{N}} \frac{\lambda_k^2}{s^2+\lambda_k^2}\phi_{\lambda_k}\langle Z, \phi_{\lambda_k}\rangle = \sum_{k\in\mathbb{N}}[1 - \frac{s^2}{s^2+\lambda_k^2}]\phi_{\lambda_k}\langle Z, \phi_{\lambda_k}\rangle \tag{170}$$

which can now easily be identified with

$$\tilde{P}_h^0(Z,s) + \tilde{P}_p^0(Z,s) = \sum_{\lambda_k \in \mathbb{R}} \tilde{a}^0_{\lambda_k}(s)\phi_{\lambda_k} + \frac{1}{2}\sum_{\lambda_k \in \mathbb{R}} \langle Z, \phi_{\lambda_k}\rangle \phi_{\lambda_k} = \sum_{k\in\mathbb{N}}[1 - \frac{s^2}{s^2+\lambda_k^2}]\phi_{\lambda_k}\langle Z, \phi_{\lambda_k}\rangle. \tag{171}$$

Momentum balance into the core acoustic domain for leading order reads

$$\frac{\partial W^0}{\partial \tau} = -\partial_Z P^0. \tag{172}$$

679 From which one finds,

$$W^0(Z,t) \quad = \quad 2\sum_{k\in\mathbb{N}}(-1)^k \frac{\cos(\lambda_k Z)}{\lambda_k}\cos\left(\lambda_k \tau\right) \tag{173}$$

The wall shear-stress is furthermore obtained in [95] from solving the boundary-layer problem. In the boundary-layer, i.e, the inner domain of the asymptotic analysis, one needs to solve the dimensionless momentum conservation (93), which includes the viscous contribution related to dimensionless pipe radius $R = R^*/R_0^*$, i.e

$$\frac{\partial W^0}{\partial \tau} = -\partial_Z P^0 + \frac{\delta^2}{R}\partial_R(R\partial_R W^0). \tag{174}$$

Defining the inner boundary-layer transverse coordinate,

$$y = (1-r)/\delta, \tag{175}$$

as well as inner boundary-layer pressure p and longitudinal velocity w, (172) leads to a boundary-layer momentum diffusion dynamics according to

$$\left(\frac{\partial}{\partial \tau} - \frac{\partial^2}{\partial y^2}\right) w^0(y,\tau) = -\partial_Z p^0 \tag{176}$$

(176) is a diffusion problem driven by the longitudinal pressure gradient associated with no-slip boundary condition

$$w^0(y,t)|_{y=0} = 0. \tag{177}$$

The Laplace transform of (176) reads

$$\left(s - \frac{\partial^2}{\partial y^2}\right)\tilde{w}^0 = -\partial_Z \tilde{p}^0. \tag{178}$$

The solution for $\tilde{w}$ with boundary condition (177) is

$$\tilde{w}^0 = -\frac{1}{s}\left(1 - e^{-\sqrt{sy}}\right)\partial_Z \tilde{p}^0. \tag{179}$$

From, (179), one can evaluate the shear-rate

$$\frac{\partial \tilde{w}^0}{\partial y} = -\frac{\sqrt{s}}{s}e^{-\sqrt{sy}}\partial_Z \tilde{p}^0, \tag{180}$$

which, evaluated at $y = 0$, gives the wall shear-stress

$$\tilde{\tau}_w^0 = \frac{\partial \tilde{w}^0}{\partial y}|_{y=0} = -\frac{\sqrt{s}}{s}\partial_Z \tilde{p}^0 = -\frac{\sqrt{s}}{s}\partial_Z \tilde{P}^0, \tag{181}$$

since the outer pressure P^0 and the inner one p^0 match together, and since neither depends on the transverse coordinate, i.e $P^0 = p^0$. From (181), the r.h.s of (83) can be evaluated, feeding the first order pressure field

$$\left[s^2 - \partial_Z^2\right] \tilde{P}^1 = -2\frac{\sqrt{s}}{s}\partial_Z^2 \tilde{P}^0(s,Z) = -2\frac{\sqrt{s}}{s}\partial_Z^2 \tilde{P}_h^0(s,Z) \tag{182}$$

since, $\partial_Z^2 \tilde{P}_p^0(s,Z) = 0$. In [95], P^1 solution in time-domain is explicitly solved from the inverse Laplace transform performing some heavy computations. Among the obtained complicated expressions, a specific one is linearly diverging with time. The so-called "secularity" condition is then introduced so as to zeros these diverging terms. In fact, this secularity condition happens when "resonant modes" are triggered by the slow-time perturbation. The resulting secularity condition then provides the envelope attenuation of the leading order, which is the main useful result of the two-time scale asymptotic analysis.

Realizing that the precise solution of P^1 is not needed in order to evaluate the secular condition [65] gives a short-cut to avoid cumbersome developments, and provides it from realizing that secularity is related to double poles in the inverse Laplace transform of $\tilde{P}^1$. This comes from the following result : given any analytical function $\phi(s)$ in the complex plane, the inverse Laplace transform of the double poles through Cauchy's residue theorem effectively leads to a linear divergence in time

$$\mathcal{L}^{-1}\left(\frac{\phi(s)}{(s \pm i\lambda_k)^2}\right)(\tau) = \lim_{s \to \pm i\lambda_k} \partial_s[\phi(s)e^{s\tau}] = [\phi(\pm i\lambda_k)\tau + \partial_s\phi(\pm i\lambda_k)]e^{\pm i\lambda_k \tau}. \tag{183}$$

Here we adapt the approach of [65] for the simpler case treated in [95] so as to better emphasize the origin of resonance modes. At order one, the solution for $\tilde{P}^1$ only has an homogeneous part for the particular one is zero since homogeneous boundary conditions apply at this order. Hence, $\tilde{P}^1(Z,s)$ can be decomposed into the orthogonal base

$$\tilde{P}^1 = \sum_{k \in \mathbb{Z}} a_1^k(\tau)\phi_{\lambda_k}(Z) \tag{184}$$

Using this decomposition in (182) whilst using the leading-order pressure solution (161)leads to

$$\sum_{\lambda_k \in \mathbb{R}} \left(s^2 + \lambda_k^2\right) \tilde{a}_{\lambda_k}^1(s)\phi_{\lambda_k}(Z) \qquad = \qquad -\frac{\sqrt{s}}{s} 2\sqrt{2} \sum_{k \in \mathbb{N}} (-1)^k \frac{s^2}{s^2 + \lambda_k^2}\phi_{\lambda_k}(Z) \tag{185}$$

where the Laplace transform of (158) have led to $\partial_Z^2 \tilde{P}^0(s,Z) = \partial_Z^2 \tilde{P}_h^0(s,Z) = s^2 \tilde{P}_h^0(s,Z)$, and where $\mathcal{L}(\sin(\lambda_k \tau) = \lambda_k/(s^2 + \lambda_k^2)$ has been used. When projecting (254) on ϕ_{λ_k}

modes one finds in (254)'s r.h.s a term proportional to $1/(s^2+\lambda_k^2)^2$ i.e proportional to $1/(s+i\lambda_k)^2(s-i\lambda_k)^2$ having two double poles in $s=\pm i\lambda_k$. From (183) one realizes that these double poles lead to a linear divergence with time, which is inconsistent with the fact that each perturbative $a_1^k(\tau)$ term has to keep being $O(1)$ so as the order-one correction δP^1 is also kept $O(\delta)$. To remove this divergent term, the leading-order solution has to be enriched with some slow-time scale envelope, so that P_h^0 (165) is re-written

$$P_h^0(Z,s,T)=\sum_{k\in\mathbb{Z}} A^0_{\lambda_k}(T)\tilde{a}^0_{\lambda_k}(s)\phi_{\lambda_k} \tag{186}$$

with $T=\delta\tau$ and the normalization condition $A^0_{\lambda_k}(T)=1$ for each $k\in\mathbb{Z}$. Using (186) and (156) in (83) using (181) then leads to

$$\left[\partial_\tau^2-\partial_Z^2\right]P^1+2\partial_T\partial_\tau P^0=-2\frac{\sqrt{s}}{s}\partial_Z^2\tilde{P}^0 \tag{187}$$

In Laplace domain, (187) becomes

$$\left[s^2-\partial_Z^2\right]\tilde{P}^1=-2\partial_T s\tilde{P}_h^0-2\frac{\sqrt{s}}{s}s^2\tilde{P}_h^0 \tag{188}$$

so that using decomposition (186) and (184), in (188) one gets

$$\sum_{k\in\mathbb{Z}}\left(s^2+\lambda_k^2\right)\tilde{a}^1_{\lambda_k}(s)\phi_{\lambda_k}(Z)=\sum_{k\in\mathbb{Z}}2s[-\partial_T A^0_{\lambda_k}-\sqrt{s}A^0_{\lambda_k}]\tilde{a}^0_{\lambda_k}(s)\phi_{\lambda_k}. \tag{189}$$

688 Projecting (189) over ϕ_{λ_k} whilst using (169) leads to

$$\begin{aligned}\tilde{a}^1_{\lambda_k}(s)+\tilde{a}^1_{-\lambda_k}(s) &= \frac{s}{\lambda_k^2+s^2}\sum_{\pm}2[-\partial_T A^0_{\pm\lambda_k}-\sqrt{s}A^0_{\pm\lambda_k}]a^0_{\pm\lambda_k} &(190)\\ &= \frac{s\langle Z,\phi_{\lambda_k}\rangle}{(\lambda_k^2+s^2)}\sum_{\pm}[\partial_T A^0_{\pm\lambda_k}+\sqrt{s}A^0_{\pm\lambda_k}][\frac{\pm i\lambda_k}{s\mp\lambda_k}+1], &(191)\end{aligned}$$

so that the double poles are canceled if the two secularity conditions

$$\lim_{s\to\pm i\lambda_k}[-\partial_T A^0_{\pm\lambda_k}(T)-\sqrt{s}A^0_{\pm\lambda_k}(T)]=0, \tag{192}$$

are met. Hence, slow time-scale amplitude dependence has to be chosen so as to cancel this term, so that

$$A^0_{\pm\lambda_k}(T)=e^{-\sqrt{\pm i\lambda_k T}}=e^{-\frac{1\pm i}{2}\sqrt{|\lambda_k|T}} \tag{193}$$

Then, using the slow amplitude solution (193) in (186) whilst using (169) and inverse Laplace transform leads to the final damped solution

$$P(Z,t,T)=2\sum_{k\in\mathbb{N}}(-1)^k\frac{\sin(\lambda_k Z)}{\lambda_k}e^{-\sqrt{\frac{\lambda_k}{2}}T}\sin\left(\lambda_k\tau-\sqrt{\frac{\lambda_k}{2}}T\right),\quad \&\quad \lambda_k=\pi\left(\frac{1}{2}+k\right), \tag{194}$$

with again, $T = \delta\tau$. This solution has been compared with several experimental recordings in [65], and will be illustrated in section 4.3. We will discuss in section 4.3 how most of the foot-steps detailed in this section can be extended when FSI effects are taken into account. Nevertheless before entering into this matter, let us now discuss how a systematic asymptotic derivation of water-hammer four-equation FSI models can be handled so as to better understand what are the constraints on the dimensionless parameter for water-hammer formulation (33)-(34) to hold.

4.2. Asymptotic analysis of water-hammer with FSI

Most of water-hammer studies are given, performed and analyzed with the implicit hypothesis or possibly the explicit measure of small Mach number. Nevertheless, how precisely small the Mach should be for water hammer wave modeling (33)-(34) to be valid has remained mostly uninformed until recently. More generally, a systematic derivation of water-hammer waves from constitutive equations (Solid Lamé's equations coupled with compressible Navier-Stokes ones) has only been recently achieved in [65]. This section discusses some aspects of this derivation which sheds new light into the mechanism underpinning the wave propagation model, and noteworthy the possible couplings between the wave and the underlying flow's steady-state.

The outer/inner fluid pressure P_f^*/p_f^*, axial velocity W_f^*/w_f^*, and radial velocity U_f^*/u_f^*, are split into steady, denoted with subscript st, and unsteady components (without subscript) following classical acoustic approach, ([164])

$$P_f^* = P^*(r,z,t) + P_{st}^*(r,z), \qquad p_f^* = p^*(r,z,t) + p_{st}^*(r,z), \tag{195}$$

$$W_f^* = W^*(r,z,t) + W_{st}(r,z), \qquad w_f^* = w^*(r,z,t) + w_{st}^*(r,z), \tag{196}$$

$$U_f^* = U^*(r,z,t), \qquad u_f^* = u^*(r,z,t). \tag{197}$$

As the steady–state is assumed unidirectional, the outer/inner radial velocity components U_f^*/u_f^*, are unsteady. Finally, the fluid stress tensors are $\boldsymbol{\sigma}_f^* = \boldsymbol{\sigma}_{st}^* + \boldsymbol{\sigma}^*$

$$\boldsymbol{\sigma}_{st}^* = (-P_{st}^* + \lambda_f \partial_z W_{st}^*)\,\mathbf{I} + \mu_f \begin{pmatrix} 0 & \cdots & \partial_r W_{st}^* \\ \cdots & 0 & \cdots \\ \partial_r W_{st}^* & \cdots & 0 \end{pmatrix}, \tag{198}$$

$$\boldsymbol{\sigma}^* = \left(-p^* + \lambda_f \left[\frac{\partial_r}{r}(r u^*) + \partial_z w^*\right]\right)\mathbf{I} + 2\mu_f \begin{pmatrix} \partial_r u^* & \cdots & \frac{\partial_r w^* + \partial_z u^*}{2} \\ \cdots & \frac{u^*}{r} & \cdots \\ \frac{\partial_r w^* + \partial_z u^*}{2} & \cdots & \partial_z w^* \end{pmatrix} \tag{199}$$

where the volume viscosity λ_f has been used. In the following the dimensionless ratio Γ of volume viscosity to dynamic viscosity will also be used :

$$\Gamma = \frac{\lambda_f}{\mu_f} \tag{200}$$

4.2.1. Dimensionless numbers setting

Two dimensionless numbers (similar to Cauchy's number) are introduced

$$\mathcal{C}_\mathcal{G} = \frac{\rho_f^* c_p^{*2}}{\mathcal{G}^*} \equiv \frac{2\rho_f^* c_p^{*2}(1+\nu_s)}{E^*}, \quad \& \quad \mathcal{C}_{\lambda_s} = \frac{\rho_f^* c_p^{*2}}{\lambda_s^*} \equiv \frac{\mathcal{C}_\mathcal{G}(1-2\nu_s)}{2\nu_s}, \tag{201}$$

where

$$\mathcal{G}^* = \frac{E^*}{2(1+\nu_s)}, \quad \& \quad \lambda_s^* = \frac{\nu_s E^*}{(1+\nu_s)(1-2\nu_s)}, \tag{202}$$

are the solid shear modulus and the second Lamé-Clapeyron coefficient, respectively. The overpressure wave velocity $c_{p,T}^*$, given in (35), is thus a corrective formulation of c_0^* due to the tube elastic constraints. By introducing parameter

$$\chi = \frac{2\mathcal{K}_f^*}{\alpha E^* \mathcal{C}^2}\left(\frac{2(1-\nu_s^2)}{2+\alpha} + \alpha(1+\nu_s)\right) \equiv \frac{2\nu_s \mathcal{C}_{\lambda_s} + (1+\alpha)^2 \mathcal{C}_\mathcal{G}}{\alpha(2+\alpha)}, \tag{203}$$

the dimensionless version of (35) is defined as the dimensionless wave speed $c_p = c_{p,T}^*/c_0^*$ and fulfills

$$c_p^2 = \frac{1}{1+\chi\mathcal{C}^2}, \quad \text{with} \quad \mathcal{C} = \frac{c_0^*}{c_{p,T}^*} \tag{204}$$

where $1+\chi\mathcal{C}^2$ is a corrective fluid pulse–wave speed factor. Regarding c_p definition in (204), it should be noted that $\mathcal{C}^2 > 1$ implies $c_p < 1$ ([6, 10, 19, 165]). Dimensionless parameters associated with boundary layer thickness δ (92), aspect ratio $\epsilon = R_0^*/L^*$, Reynolds number Re, pulsed Reynolds number Re_p and Mach number $\mathcal{M}$ are related as

$$Re_p = \frac{c_p R_0}{\nu_f} \gg 1, \qquad Re = \frac{W_0 R_0}{\nu_f} = \mathcal{M} Re_p, \tag{205}$$

$$\delta^2 = \frac{\nu_f L}{c_p R_0^2} = \frac{1}{\epsilon Re_p} \ll 1, \qquad \mathcal{M} = \frac{W_0}{c_p} \ll 1. \tag{206}$$

Low–Mach number i.e. $\mathcal{M} \ll 1$ and long–wavelength, i.e. $\epsilon \ll 1$ ([28, 32, 166, 43]), are generally considered for water-hammer validity [13, 167]. But, much

more precisely, they have been asymptotically established in [65] within the following condition

$$\delta^2 \gg \mathcal{M} > \frac{\mathcal{M}}{\mathcal{C}^2}, \qquad \delta \gg \epsilon^2, \qquad \delta \gg \alpha\mathcal{M}, \qquad 1 \gg \epsilon \gg \alpha\mathcal{M}. \tag{207}$$

We now provide some supplementary details of this asymptotic analysis, especially those related to $O(\delta)$ corrections which were considered in the previous section but also other possible corrections/contributions such as $O(\mathcal{M}/\delta)$, $O(\mathcal{M}\epsilon Re)$ and $O\left(\frac{\mathcal{M}\epsilon Re}{\delta}\right)$.

4.2.2. Navier–Stokes equations

Taking W_{st} as the reference dimensionless velocity for the steady- longitudinal flow, and as previously W_0^* for the disturbance, and since long–wavelength assumption implies that the radial fluid velocity component is ϵ smaller than the axial one, dimensionless pressure and velocity fulfill

$$P_{st}^* = \rho_{f_0} W_0^{*2} P_{st}(R,Z), \qquad W_{st}^* = W_0^* W_{st}(R,Z), \tag{208}$$

$$P^* = \rho_{f_0} c_p W_0^* P(R,Z,\tau), \qquad p^* = \rho_{f_0} c_p W_0^* p(y,Z,\tau), \tag{209}$$

$$W^* = W_0^* W(R,Z,\tau), \qquad w^* = W_0^* w(y,Z,\tau), \tag{210}$$

$$U^* = \epsilon W_0 U(R,Z,\tau), \qquad u^* = \epsilon W_0 u(y,Z,\tau), \tag{211}$$

where capital letters have been used to define the outer variables, and lower case has been chosen for inner variables. Note that the perturbed velocity and the steady state both scale as W_0^* since the perturbation is supposed to arise from an order-one fraction of the steady state velocity. From (208)-(211) it is also useful to define dimensionless stress and shear as

$$\tau_f^* = -\frac{\rho_f^* \nu_f^* W_0^*}{\delta R_0^*} \tau_f(y,Z,\tau), \qquad \tau_f = \partial_y w(y,Z,\tau), \tag{212}$$

$$\boldsymbol{\sigma}^* = \rho_{f_0}^* c_p^* W_0^* \boldsymbol{\sigma}, \qquad \boldsymbol{\sigma}_{st}^* = \rho_{f_0}^* W_0^{*2} \boldsymbol{\sigma}_{st}, \tag{213}$$

with,

$$\boldsymbol{\sigma}_{st} = \left(-P_{st} + \Gamma \frac{(\epsilon\delta)^2}{\mathcal{M}} \partial_Z W_{st}\right) \mathbf{I} + \frac{\epsilon\delta}{\mathcal{M}} \begin{pmatrix} 0 & \cdots & -\partial_y W_{st} \\ \cdots & 0 & \cdots \\ -\partial_y W_{st} & \cdots & \epsilon\delta \partial_Z W_{st} \end{pmatrix}, \tag{214}$$

715

$$\boldsymbol{\sigma} = \left(-p + \Gamma\left(\epsilon\delta\right)^2\left(-\frac{\partial_y\left[\left(1-\delta y\right)u\right]}{\delta\left(1-\delta y\right)} + \partial_Z w\right)\right)\mathbf{I} + \epsilon\delta\begin{pmatrix} -2\epsilon\partial_y u & \cdots & -\partial_y w + \epsilon^2\partial_Z u \\ \cdots & 2\epsilon\delta\frac{u}{1-\delta y} & \cdots \\ -\partial_y w + \epsilon^2\partial_Z u & \cdots & 2\epsilon\delta\partial_Z w \end{pmatrix}. \tag{215}$$

Integrating the fluid isentropic compression law (6) the fluid density is subjected to pressure variations following

$$\rho_f^*(r,z,t) = \rho_{f_0}^* e^{\frac{P_f^*(r,z,t)}{\mathcal{K}_f}} = \rho_{f_0}^* e^{\frac{P^*(r,z,t)+P_{st}^*(r,z)}{\mathcal{K}_f}}, \tag{216}$$

so that by introducing the dimensionless density $\rho_f = \rho_f^*/\rho_{f_0}^*$ whilst using scalings (208)–(211) yields

$$\left[1, \boldsymbol{\nabla}, \partial_\tau\right]\rho_f = e^{\frac{\mathcal{M}}{\mathcal{C}^2}\left(P+\mathcal{M}P_{st}\right)}\left[1, \frac{\mathcal{M}}{\mathcal{C}^2}\boldsymbol{\nabla}\left(P+\mathcal{M}P_{st}\right), \frac{\mathcal{M}}{\mathcal{C}^2}\partial_\tau P\right], \tag{217}$$

with $\boldsymbol{\nabla}$ the dimensionless nabla operator, $\mathcal{C}^2$ define in (204) and $\mathcal{M}/\mathcal{C}^2 \ll 1$. Obviously, in the inner region (217) holds from replacing P by the inner pressure p. The Navier–Stokes equations, which follow from fluid mass and momentum conservations, are

$$\left(\partial_t + W_f^*\partial_z + U^*\partial_r\right)\rho_f^* + \rho_f^*\left(\partial_z W_f^* + \frac{1}{r}\partial_r\left(r\partial_r U^*\right)\right) = 0, \tag{218}$$

$$\begin{aligned}\rho_f^*\left(\partial_t + W_f^*\partial_z + U^*\partial_r\right)W_f^* &= -\partial_z P_f^* \\ &+ \rho_{f_0}\nu_f\left(\left(1+\Gamma\right)\partial_z\left[\partial_z W_f^* + \frac{\partial_r}{r}\left(rU^*\right)\right] + \left(\frac{\partial_r}{r}\left(r\partial_r\right) + \partial_z^2\right)W_f^*\right),\end{aligned} \tag{219}$$

$$\begin{aligned}\rho_f^*\left(\partial_t + W_f^*\partial_z + U^*\partial_r\right)U^* &= -\partial_r P_f^* \\ &+ \rho_{f_0}\nu_f\left(\left(1+\Gamma\right)\partial_r\left[\partial_z W_f^* + \frac{\partial_r}{r}\left(rU^*\right)\right] + \left(\frac{\partial_r}{r}\left(r\partial_r\right) - \frac{1}{r^2} + \partial_z^2\right)U^*\right),\end{aligned} \tag{220}$$

716 where Γ definition (200) has been used. They are now decomposed into steady-state
717 and perturbations.

718 *4.2.3. Dimensionless steady–state fluid equations*

At steady–state, the fluid unsteady components vanish, so that the dimensionless steady version of (218)–(220) reads

$$\left(\frac{\mathcal{M}}{\mathcal{C}}\right)^2 W_{st}\partial_Z P_{st} + \partial_Z W_{st} = 0, \tag{221}$$

$$\mathcal{M}e^{\left(\frac{\mathcal{M}}{C}\right)^2 P_{st}} W_{st}\partial_Z W_{st} = -\mathcal{M}\partial_Z P_{st} + (\epsilon\delta)^2 (2+\Gamma)\partial_Z^2 W_{st} + \delta^2 \frac{\partial_R}{R}\left(R\partial_R\right) W_{st}, \quad (222)$$

$$\frac{\mathcal{M}}{\epsilon^2}\partial_R P_{st} = (1+\Gamma)\delta^2 \partial_R \partial_Z W_{st}, \quad (223)$$

From (221), the leading–order dimensionless steady solution $\left(W_{st}^0, P_{st}^0\right)$ fulfills

$$\partial_Z W_{st}^0 = 0. \quad (224)$$

On the other hand, $\epsilon^2\delta^2/\mathcal{M} = \epsilon/R_e \ll 1$ follows from the definition of δ, ϵ and $\mathcal{M}$ in (205)–(206) so that using (224) in (223) leads to find that the steady–state leading–order pressure field is uniform per section

$$\partial_R P_{st}^0 = 0. \quad (225)$$

Finally, the steady–state leading–order axial mass conservation equation (222) results in equalizing a R–dependent function to a Z–dependent one

$$\mathcal{M}\partial_Z P_{st}^0 = \delta^2 \frac{\partial_R}{R}\left(R\partial_R W_{st}^0\right), \quad (226)$$

yielding the steady-state velocity W_{st}

$$W_{st}^0 \quad = \quad \frac{\mathcal{M}}{4\delta^2}\partial_Z P_{st}^0 \left[R^2 - 1\right] = \frac{\mathcal{M}}{4\delta}\partial_Z P_{st}^0 \left[\delta y - 2\right] y, \quad (227)$$

since $R = 1 - \delta y$. Note that, in the core region e.g. $R = 0$, $W_{st}^0 \sim \mathcal{M}/\delta^2 = \epsilon Re$ which results from the steady-state balance between the inertial pressure with viscous dissipation. Furthermore, from (227), one can evaluate the steady-state leading order shear stress

$$\partial_y w_{st}^0 \equiv \tau_{st}^0 \quad = \quad \frac{\mathcal{M}}{4\delta}\partial_Z P_{st}^0 \left[\delta y - 2\right] + \frac{\mathcal{M}}{4}\partial_Z P_{st}^0 y, \quad (228)$$

which is thus found $\tau_{st}^0 \sim O(\mathcal{M}/\delta)$. From (228) one can now compare the relative contribution of the steady to transient friction in (85). Since $\tau_{tr} = \tau_f = \partial_y w(y, Z, \tau) \sim O(1)$ in (212) it is easy to find that the relative steady-state shear stress contribution compared to unsteady one is $O(\mathcal{M}/\delta)$. It first means that decomposition (85) is meaningful only if $\mathcal{M}/\delta$ is not too small, but also that if $\mathcal{M}/\delta \sim \delta$, then, there is a need to take into account the steady-state shear, when considering viscous dissipation for the unsteady contributions arising at $O(\delta)$. In section 4.2.5 it is shown that such

condition, i.e $\mathcal{M}/\delta \sim \delta$ also necessitates to take care of perturbed shear-stress radial convection, a task not yet achieved in the literature. Last but not least, as done in the next section, since the transient can always be written as the superposition of a perturbation over a pre-existing steady-state both in the fluid and the solid, every aspect of the steady-state including normal stress and shear-stress at the liquid/solid interface can be subtracted from the analysis. In other words, decomposition (85) cannot involve the steady shear τ_{st} for transient analysis, and this is why a quasi-steady τ_{qst} is used. However, even if a Darcy-Weisbach quasi-steady shear (84) is sometimes successfully used in engineering applications, to the best of our knowledge, it is still lacking for theoretical basis. As a possible path for future investigation we will however provide the conditions for steady-state and transient to be coupled together from inertial non-linearities in the following sections.

4.2.4. Dimensionless unsteady bulk fluid equations

Subtracting the steady–state relations (221)–(223), from (218)–(220) whilst using scalings (208)–(211), the outer region dimensionless mass and momentum conservation equations read

$$\partial_\tau P + \mathcal{M}\left(\left[W\partial_Z + U\partial_R\right](P + \mathcal{M}P_{st}) + W_{st}\partial_Z P\right) + \mathcal{C}^2\left[\partial_Z W + \frac{1}{R}\partial_R\left(RU\right)\right] = 0, \tag{229}$$

$$e^{\frac{\mathcal{M}}{\mathcal{C}^2}(P+\mathcal{M}P_{st})}\left(\partial_\tau W + \mathcal{M}\left(\left[W\partial_Z + U\partial_R\right](W + W_{st}) + W_{st}\partial_Z W\right)\right) =$$
$$-\partial_Z P + (\epsilon\delta)^2(1+\Gamma)\partial_Z\left[\partial_Z W + \frac{1}{R}\partial_R\left(RU\right)\right] + \delta^2\left(\frac{\partial_R}{R}R\partial_R + \epsilon^2\partial_Z^2\right)W, \tag{230}$$

$$e^{\frac{\mathcal{M}}{\mathcal{C}^2}(P+\mathcal{M}P_{st})}\left(\partial_\tau + \mathcal{M}\left[\left(W + W_{st}\right)\partial_Z + U\partial_R\right]\right)U = -\frac{1}{\epsilon^2}\partial_R P$$
$$+\delta^2(1+\Gamma)\partial_R\left[\partial_Z W + \frac{1}{R}\partial_R\left(RU\right)\right] + \delta^2\left(\frac{\partial_R}{R}\left(R\partial_R\right) - \frac{1}{R^2} + \epsilon^2\partial_Z^2\right)U, \tag{231}$$

The steady–state contributions into the unsteady fluid equations (229)–(231) appear to be driven by the Mach number, i.e are $O(\mathcal{M})$. More precisely, from (227) one finds that the outer steady-state contributions in (229)-(231) are $O(\mathcal{M}\epsilon Re)$, thus not significant as far as $\delta \gg \mathcal{M}(\epsilon Re)$. Following the asymptotic framework of [65], since $\delta^2 \gg \mathcal{M}$, no steady–state contributions arise into the outer region (core region of the pipe). What happens in the unsteady boundary-layer is now discussed.

4.2.5. Dimensionless unsteady fluid boundary-layer equations

In the inner viscous zone, using rescaled coordinate y defined in (175) dimensionless Navier–Stokes equations are

$$\partial_\tau p + \mathcal{M}\left(\left[w\partial_Z - \frac{u}{\delta}\partial_y\right](p+\mathcal{M}P_{st}) + w_{st}\partial_Z p\right) + \mathcal{C}^2\left[\partial_Z w - \frac{1}{\delta}\frac{1}{1-\delta y}\partial_y\left((1-\delta y)u\right)\right] = 0, \tag{232}$$

$$\begin{aligned} e^{\frac{\mathcal{M}}{\mathcal{C}^2}(p+\mathcal{M}P_{st})}&\left(\partial_\tau w + \mathcal{M}\left(\left[w\partial_Z - \frac{u}{\delta}\partial_y\right](w+w_{st}) + w_{st}\partial_Z w\right)\right) \\ &= -\partial_Z p + (\epsilon\delta)^2(1+\Gamma)\partial_Z\left[\partial_Z w - \frac{1}{\delta}\frac{1}{1-\delta y}\partial_y\left((1-\delta y)u\right)\right] \\ &\quad + \left(\frac{\partial_y}{1-\delta y}\left((1-\delta y)\partial_y\right) + (\epsilon\delta)^2\partial_Z^2\right)w, \end{aligned} \tag{233}$$

$$\begin{aligned} e^{\frac{\mathcal{M}}{\mathcal{C}^2}(p+\mathcal{M}P_{st})}&\left(\partial_\tau + \mathcal{M}\left[(w+w_{st})\partial_Z - \frac{u}{\delta}\partial_y\right]\right)u = \frac{1}{\delta\epsilon^2}\partial_y p \\ &\quad - (1+\Gamma)\partial_y\left[\delta\partial_Z w - \frac{1}{1-\delta y}\partial_y\left((1-\delta y)u\right)\right] \\ &\quad + \left(\frac{\partial_y}{1-\delta y}\left((1-\delta y)\partial_y\right) - \frac{\delta^2}{(1-\delta y)^2} + (\epsilon\delta)^2\partial_Z^2\right)u. \end{aligned} \tag{234}$$

(233) can be expanded and simplified to

$$\begin{aligned} e^{\frac{\mathcal{M}}{\mathcal{C}^2}(p+\mathcal{M}P_{st})}&\left(\partial_\tau w + \mathcal{M}\left((w+w_{st})\partial_Z w - \frac{u}{\delta}\left(\tau_f + \partial_y w_{st}\right) + w\partial_Z w_{st}\right)\right) \\ &= -\partial_Z p + (\epsilon\delta)^2(1+\Gamma)\partial_Z\left[\partial_Z w - \frac{1}{\delta}\left(\partial_y u - \delta\frac{u}{1-\delta y}\right)\right] \\ &\quad + \partial_y^2 w - \delta\frac{\tau_f}{1-\delta y} + (\epsilon\delta)^2\partial_Z^2 w, \end{aligned} \tag{235}$$

where dimensionless shear-rate $\tau_f = \partial_y w$ defined in (212) has been used. From (235), one finds that various possible dissipation term can arise

- $O\left(\frac{\mathcal{M}}{\mathcal{C}^2}\right)$ and $O\left(\left(\frac{\mathcal{M}}{\mathcal{C}}\right)^2\right)$ fluid density compressibility effects (217);
- $O\left(\epsilon^2\delta\right)$ radial flow compressibility effects within the inner region;
- $O\left(\epsilon^2\delta^2\right)$ and $O\left(\epsilon^2\delta\right)$ axial diffusion and radial flow compressibility;
- $O\left(\mathcal{M}\right)$ and $O\left(\mathcal{M}\epsilon Re\right)$, axial inertial corrections;
- $O\left(\frac{\mathcal{M}}{\delta}\right)$ and $O\left(\frac{\mathcal{M}\epsilon Re}{\delta}\right)$ radial inertial transport of viscous shear;
- $O\left(\delta\right)$ radial diffusion transport of viscous shear.

This very last effect is the only one been analyzed by [65] reaching to the "classical" four equation FSI (33)-(34) model (more precisely a perturbative version of it, as further detailed in 4.2.6). Furthermore, since the leading-order steady dimensionless inner velocity field (227) is $w_{st} \sim O(\mathcal{M}/\delta^2) \equiv O(\epsilon Re)$ the steady-state/perturbation couplings terms in (235) are either $O(\mathcal{M}\epsilon Re)$ or $O\left(\mathcal{M}\epsilon Re/\delta\right)$. As already mentioned in (207), [65] have considered the asymptotic setting (207) for which all these contributions are not significant, so that transient and steady-state are decoupled. Nevertheless, (235) shows that there is a possible non-trivial one-way coupling between the steady-state and the perturbation when the steady-state inertia rises, i.e for $\epsilon Re > 1$, when $\mathcal{M}\epsilon Re/\delta \sim \delta$, i.e $\delta^2 \sim \mathcal{M}\epsilon Re$ (keeping with the largest perturbative term only). This asymptotic regime has not yet been analyzed in the literature but it might result in a deeper understanding of why, as inertia increases, there is a need for changing the friction model depending on the steady flow inertia as already mentioned in section 2.3.

4.2.6. Dimensionless boundary condition and FSI perturbative two-wave formulation

From (198)-(199) and (195) it has been shown in [65] that dimensionless stress boundary conditions at the solid-fluid interface settled at $R = 1 + O(\alpha\mathcal{M})$ and at the solid external boundary at $R = 1 + \alpha + O(\alpha\mathcal{M})$ read

$$\sigma_{rr}\big|_{R=1+O(\alpha\mathcal{M})} = -p\big|_{y=O\left(\frac{\alpha\mathcal{M}}{\delta}\right)} + O\left(\alpha\epsilon\mathcal{M}\right), \;\; \& \;\; \sigma_{rr}\big|_{R=1+\alpha+O(\alpha\mathcal{M})} = O\left(\alpha\epsilon\mathcal{M}\right), \quad (236)$$

$$\sigma_{rz}\big|_{R=1+O(\alpha\mathcal{M})} = -\delta\tau_w\big|_{y=O\left(\frac{\alpha\mathcal{M}}{\delta}\right)} + O\left(\alpha\epsilon\mathcal{M}\right), \;\; \& \;\; \sigma_{rz}\big|_{R=1+\alpha+O(\alpha\mathcal{M})} = O\left(\alpha\epsilon\mathcal{M}\right), \quad (237)$$

It is important to note that the transient shear-stress coupling between the solid and the fluid found in (237) appears as an $O(\delta)$ correction. At leading order, the solid response is independent from the fluid dissipation. This very small detail is the corner-stone of the perturbative approach of [65], since it implies that FSI can only occur perturbatively and should be derived as such. Nevertheless, including $O(\delta)$ then also necessitates, for asymptotic consistency, to take care of small time-scale variations from (156) also providing $O(\delta)$ corrections.

Using fluid pressure/longitudinal stress vector $\mathbf{P}$ previously defined in (40), a perturbative expansion of $\mathbf{P}$ is considered as

$$\mathbf{P}^0 + \delta\mathbf{P}^1 = \begin{pmatrix} P^0 + \delta P^1 \\ \sigma_{zz}^0 + \delta\sigma_{zz}^1 \end{pmatrix}. \quad (238)$$

Inlet/outlet boundary conditions are also needed for the wave problem to be closed. For a single pipe, having dimensionless length unity, they read as follows (Cf [65] for more information)

$$\partial_Z P^0\big|_{Z=1} = \delta(\tau) \quad \text{, and, } \quad \partial_Z P^1\big|_{Z=1} = 0, \tag{239}$$

where $\delta(\tau)$ is the Dirac distribution. Upstream, the homogeneous Dirichlet condition applied on the pressure trivially leads to

$$P^0\big|_{Z=0} = P^1\big|_{Z=0} = 0. \tag{240}$$

In the solid, the upstream and downstream conditions are

$$\partial_Z \sigma^0_{zz}\big|_{Z=0\&1} = 0 \quad \text{, and, } \quad \partial_Z \sigma^1_{zz}\big|_{Z=0\&1} = -\frac{2}{\alpha(2+\alpha)} \tau^0_w\big|_{Z=0\&1}. \tag{241}$$

[65] establishes a perturbative coupled waves equation reading

$$\left(\partial^2_\tau - \mathbf{C}^2_{\mathbf{P}} \partial^2_Z\right)\left[\mathbf{P}^0 + \delta \mathbf{P}^1\right] = -2\delta \left[\partial_T \partial_\tau \mathbf{P}^0 - \partial_Z \tau^0_w \begin{pmatrix} 1 + \frac{2\nu_s \mathcal{D}}{\alpha(2+\alpha)} \\ \frac{1}{\alpha(2+\alpha)} \left[2\nu_s \mathcal{D} + \mathcal{C}_s^2 + \frac{4\nu_s^2 \mathcal{D}}{\alpha(2+\alpha)}\right] \end{pmatrix}\right], \tag{242}$$

where matrix $\mathbf{C}^2_{\mathbf{P}}$ defined in (40) has been used. (242) is the dimensionless perturbative version of (33)-(34), and the strict equivalence between the wave operator has been shown in [65]. Note that the limit $\nu_s \to 0$, (242) degenerates to the non-FSI dissipative pressure wave (83). The leading–order of (242) displays a parabolic form without dissipation associated with a fast time–scale wave propagation already analyzed in section 2.2.1, as opposed to the additional slow–time scale damping that arises when $O(\delta)$ corrections are considered. This short–time behavior appears because the dissipation in the fluid boundary layer does not have time to develop, and the coupled system remains purely conservative. We now present how this perturbative FSI couple wave can be analyzed within a two-time scale asymptotic analysis similar to section 4.1.

4.3. Two-time scale asymptotic analysis of water-hammer with FSI

The Laplace transform of the transient wall shear-stress has been derived in [65] and reads

$$\partial_Z \tilde{\tau}^0_w = -s\sqrt{s}\left(\left[1 - (1-2\nu_s)\frac{2\nu_s \mathcal{D}}{\alpha \mathcal{C}_s^2 (2+\alpha)}\right]\tilde{P}^0 + (1-2\nu_s)\frac{\mathcal{D}}{\mathcal{C}_s^2}\tilde{\sigma}^0_{zz}\right). \tag{243}$$

The axial gradient of the fluid wall shear stress is thus a linear combination of $\tilde{P}^0$ and $\tilde{\sigma^0_{zz}}$. The Laplace transform of (242) then reads

$$\left(s^2 - \mathbf{C}_\mathbf{P}^2 \partial_Z^2\right) \tilde{\mathbf{P}}^0 = \mathbf{0}, \tag{244}$$

$$\left(s^2 - \mathbf{C}_\mathbf{P}^2 \partial_Z^2\right) \tilde{\mathbf{P}}^1 = -2s \left[\partial_T + \sqrt{s}\mathbf{E}\right] \tilde{\mathbf{P}}^0, \tag{245}$$

where matrix $\mathbf{E}$ has been introduced

$$\mathbf{E} = \frac{1}{2\nu_s} \begin{pmatrix} \left(1 - (1-2\nu_s)\frac{\overline{c^2}-1}{\mathcal{C}_s^2}\right)\left(1 + \frac{2\nu_s\mathcal{D}}{\alpha(2+\alpha)}\right) & \frac{2\nu_s\mathcal{D}(1-2\nu_s)}{\mathcal{C}_s^2}\left(1 + \frac{2\nu_s\mathcal{D}}{\alpha(2+\alpha)}\right) \\ \left(1 - (1-2\nu_s)\frac{\overline{c^2}-1}{\mathcal{C}_s^2}\right)\frac{\overline{c^2}-(1-2\nu_s)}{\alpha(2+\alpha)} & \frac{2\nu_s\mathcal{D}(1-2\nu_s)}{\mathcal{C}_s^2}\frac{\overline{c^2}-(1-2\nu_s)}{\alpha(2+\alpha)} \end{pmatrix}. \tag{246}$$

(244) and (245) are the FSI generalization of (158) and (188). 2×2 matrix $\mathbf{E}$ (246) then permits to find the damping rate from following the very same footsteps as in section 4.1. Using previously defined base change (45) associated with diagonal base $\boldsymbol{\mathcal{P}} = \boldsymbol{\Pi}^{-1}\mathbf{P}$, and decomposing $\boldsymbol{\mathcal{P}}$ over eigenfunctions (58)-(59), then leads to

$$\tilde{\boldsymbol{\mathcal{P}}}^0(Z,s,T) = \sum_{\lambda_k \in \mathbb{R}} \tilde{a}^0_{\lambda_k}(s) A_{\lambda_k}(T) \boldsymbol{\Phi}_{\lambda_k}(Z) + \tilde{\boldsymbol{\mathcal{P}}}^0_p(Z), \tag{247}$$

$$\tilde{\boldsymbol{\mathcal{P}}}^1(Z,s) = \sum_{\lambda_k \in \mathbb{R}} \tilde{a}^1_{\lambda_k}(s) \boldsymbol{\Phi}_{\lambda_k}(Z) + \tilde{\boldsymbol{\mathcal{P}}}^1_p(Z,s), \tag{248}$$

with particular solution associated with non-homogeneous boundary conditions (239)-(240) and (241)

$$\tilde{\boldsymbol{\mathcal{P}}}^0_p(Z) = \frac{Z}{\det(\boldsymbol{\Pi})}\begin{pmatrix} 1 \\ -1 \end{pmatrix}, \tag{249}$$

$$\tilde{\boldsymbol{\mathcal{P}}}^1_p(Z,s) = \frac{1}{\alpha(2+\alpha)\sqrt{s}}\left(\frac{Z^2}{1-\frac{c_+}{c_-\beta}}\begin{pmatrix} 1 \\ \frac{-c_+}{c_-\beta} \end{pmatrix} - \frac{4\nu_s\mathcal{D}\left(\frac{Z^2}{2} - Z\right)}{c_-^2 - 1}\begin{pmatrix} 1 & 0 \\ 0 & \frac{c_-\beta}{c_+} \end{pmatrix}\partial_Z\tilde{\boldsymbol{\mathcal{P}}}^0\right)(Z). \tag{250}$$

The Laplace transform of (244) leads to

$$\sum_{\lambda_k \in \mathbb{R}} \left(s^2 - \mathcal{H}\right) \tilde{a}^0_{\lambda_k}(s) \boldsymbol{\Phi}_{\lambda_k}(Z) = -s^2 \tilde{\boldsymbol{\mathcal{P}}}^0_p(Z), \tag{251}$$

where operator $\mathcal{H}$ has been defined in (58). Using (244), (247) and the orthogonality of the eigenfunction basis one gets

$$\tilde{a}^0_{\lambda_k}(s) + \tilde{a}^0_{-\lambda_k}(s) = \left[\frac{\lambda_k}{2i}\left(\frac{1}{s - i\lambda_k} - \frac{1}{s + i\lambda_k}\right) - 1\right] \langle \tilde{\boldsymbol{\mathcal{P}}}^0_p(Z), \boldsymbol{\Phi}_{\lambda_k}(Z) \rangle. \tag{252}$$

leading to

$$\tilde{a}^0_{\pm\lambda_k}(s) = -\frac{1}{2}\left[\frac{\pm i\lambda_k}{s \mp i\lambda_k} + 1\right] \langle \tilde{\boldsymbol{\mathcal{P}}}^0_p(Z), \boldsymbol{\Phi}_{\lambda_k}(Z)\rangle. \tag{253}$$

a result which generalizes (169). At next order, the Laplace transform of (245) is

$$\sum_{\lambda_k\in\mathbb{R}} \left(s^2+\lambda_k^2\right) \tilde{a}^1_{\lambda_k}(s)\boldsymbol{\Phi}_{\lambda_k}(Z) = -\left(s^2-\mathcal{H}\right)\tilde{\boldsymbol{\mathcal{P}}}^1_p(Z,s) - 2s\sqrt{s}\boldsymbol{\mathcal{E}}\tilde{\boldsymbol{\mathcal{P}}}^0_p(Z,s)$$
$$+ s\sum_{\lambda_k\in\mathbb{R}} \left[\partial_T + \sqrt{s}\boldsymbol{\mathcal{E}}\right] A_{\lambda_k}(T)\left[\frac{i\lambda_k}{s-i\lambda_k}+1\right]\langle\tilde{\boldsymbol{\mathcal{P}}}^0_p(Z,s), \boldsymbol{\Phi}_{\lambda_k}(Z)\rangle\boldsymbol{\Phi}_{\lambda_k}(Z). \tag{254}$$

where $\boldsymbol{\mathcal{E}} = \boldsymbol{\Pi}\cdot\mathbf{E}\cdot\boldsymbol{\Pi}^{-1}$ is the base-transform of matrix $\mathbf{E}$ with, again the base change matrix $\boldsymbol{\Pi}$ defined in (45). As previously detailed in section 4.1, the secularity condition is found from suppressing resonant modes of $\tilde{a}^1_{\lambda_k}(s)$ solutions. Defining the 2-component vector function

$$\boldsymbol{\mathcal{J}}_{\lambda_k}(Z,s) = \frac{\lambda_k}{\alpha(2+\alpha)\left(1-\frac{c_-\beta}{c_+}\right)}\begin{pmatrix} \left(s^2\left(\frac{Z^2}{2}-Z\right)-c_-^2\right)\frac{\tan\left(\frac{\lambda_k}{c_-}\right)}{c_-} \\ -\left(s^2\left(\frac{Z^2}{2}-Z\right)-c_+^2\right)\frac{\tan\left(\frac{\lambda_k}{c_+}\right)}{c_+}\end{pmatrix}, \tag{255}$$

[65] found that the FSI secularity condition reads

$$\lim_{s\to\pm i\lambda_k}\left(\partial_T + \sqrt{s}\langle\boldsymbol{\mathcal{E}}\boldsymbol{\Phi}_{\lambda_k}(Z) - \frac{\boldsymbol{\mathcal{J}}_{\lambda_k}(Z,s)}{s^2}, \boldsymbol{\Phi}_{\lambda_k}(Z)\rangle\right) A_{\pm\lambda_k}(T) = 0. \tag{256}$$

807 This leads to the FSI slow-time attenuation amplitude

$$A_{\lambda_k}(T) = e^{-\sqrt{i\lambda_k}\frac{T}{\mathcal{T}_{\lambda_k}}}, \tag{257}$$
$$\mathcal{T}^{-1}_{\lambda_k} = \langle\boldsymbol{\mathcal{E}}\boldsymbol{\Phi}_{\lambda_k}(Z) + \frac{\boldsymbol{\mathcal{J}}_{\lambda_k}(Z, s=i\lambda_k)}{\lambda_k^2}, \boldsymbol{\Phi}_{\lambda_k}(Z)\rangle, \tag{258}$$

808 More explicit (and rather cumbersome) computation of $\mathcal{T}_{\lambda_k}$ are detailed in [65]'s
809 Appendix. [65] found that the limit $\nu_s \to 0$ of (258) tends to (193). This FSI
810 theoretical prediction has been compared to experimental results as well as
811 non-FSI attenuation in [65]. More precisely, the pressure signature is compared
812 at two distinct locations in Figure 15 from ([99])'s data set. The special case
813 $\nu_s \to 0$ or that of ([95]) is again depicted. Each analytical solutions exhibits
814 excellent agreement for both amplitude and phase for every considered pipe's

Table 2: Physical and geometrical properties for the analysis of the reservoir pipe anchored valve system. ($\star$) refers to unavailable data in the original article. They were estimated in [65] based up available properties of pure copper tube and water.

Article	**Density** $(kg \cdot m^{-3})$	**Elasticity** $(10^9 Pa)$	ν_f $(m^2 \cdot s^{-1})$	ν_s	**Geometry** (m)
([107])	$\rho^*_{f_0} = 998.3$ $\rho^*_{s_0} = 8935.0$	$\mathcal{K}^*_f = 2.1$ $E^* = 127.0$	$3.967 \cdot 10^{-5}$	$0.34^\star$	$R = 0.0127$ $e = 0.001651$ $L = 36.088$
([99])	$\rho_{f_0} = 1000.0$ $\rho_{s_0} = 8890.0$	$\mathcal{K}_f = 2.1$ $E = 120.0$	$9.493 \cdot 10.0^{-7.0}$	0.35	$R = 0.008$ $e = 0.001$ $L = 98.11$
([98])	$\rho^*_{f_0} = 1000.0$ $\rho^*_{s_0} = 8960.0$	$\mathcal{K}^*_f = 2.1$ $E^* = 130.0$	$1.182 \cdot 10^{-6.0}$	$0.3^\star$	$R = 0.01105$ $e = 0.00163$ $L = 37.23$
([168])	$\rho^*_{f_0} = 1000.0$ $\rho^\star_{s_0} = 8960.0$	$\mathcal{K}^*_f = 2.1$ $E^* = 130.0$	$10^{-6.0}$	$0.3^\star$	$R = 0.01$ $e = 0.001$ $L = 15.22$

locations with experimental observations. No parameter fit is used. The variety of observed patterns of the pressure signal depicted in Figure 15 and the surprisingly precise predictions provided by the theory results from the complex mode decomposition $\mathbf{\Phi}_{\lambda_k}(Z)$, each with its own phase. In Figure (15a), a deeper analysis of the pressure signature reveals that ([95])'s theory leads to a better agreement with experimental data in the early times, i.e. $\tau \ll O\left(1/\delta\right)$. At longer times, both models correctly describe the attenuation, ([95])'s theory under–attenuating, whilst the hereby developed one slightly over–attenuating. In Figure (15b) however, the present analysis shows excellent agreement with experimental data at long time, ([95])'s theory again under–attenuating. It is worth noting that these differences are minor in both configurations as the (FSI) coupling has little influences in this experimental data set.

To deepen the analysis of the new prediction for (FSI) damping, Figures (16a)–

(16d) then focus on the damping envelope of the first exponential mode. A comparison with four sets of experiments is provided. For each experiment, the pressures of the envelope peaks are extracted, non–dimensionalized, and compared with the theoretical damping trend. Figures (16a)–(16d) reveal a very good agreement between the predictions and experiments for laminar and transitional Reynolds numbers. As the first mode damping is dominant over others at long time, the match between predictions and observations becomes better with time, as expected.

Last, but not least, the asymptotic analysis of the FSI water-hammer wave [65] has permitted to derive the FSI transient wall shear-stress which indeed differs from the non-FSI one (181). In frequency domain, both transient shear-rate and wall-shear stress have been found equal to

$$\tilde{\tau}_f^0 = \partial_y \tilde{w}^0 = -\sqrt{s}\left[\frac{1}{s}\partial_Z \tilde{P}^0 + s\alpha\tilde{\zeta}^0\right] e^{-\sqrt{s}y}, \tag{259}$$

$$\tilde{\tau}_w^0 = -\sqrt{s}\left[\frac{1}{s}\partial_Z \tilde{P}^0 + s\alpha\tilde{\zeta}^0\right]. \tag{260}$$

where $\tilde{\zeta}^0$ is the leading order longitudinal solid displacement at the fluid-solid interface $R=1$ whose relation with $\mathbf{P}^0 = \begin{pmatrix} P^0 \\ \sigma_{zz}^0 \end{pmatrix}$ components (and their Laplace transform) are

$$\frac{\alpha\mathcal{C}_s^2}{\mathcal{D}}\partial_Z\tilde{\zeta}^0 = \tilde{\sigma}_{zz}^0 - \frac{2\nu_s}{\alpha(2+\alpha)}\tilde{p}^0 \tag{261}$$

Comparing (260) with (181) reveals that a supplementary FSI term associated with the solid longitudinal displacement should be included in the wall shear stress. [65] also found that re-writing (260) in time-domain in a form similar with Zielke's one in [109] leads to

$$\tau_w^0 = \frac{1}{\sqrt{\pi}}\int_0^\tau \frac{\partial_{\tau'}\left[W^0 - \alpha\partial_{\tau'}\zeta^0\right]}{\sqrt{\tau-\tau'}}d\tau'. \tag{262}$$

(262) shows that the supplementary FSI term leads to consider the *relative* acceleration of the fluid to that of the pipe's wall, rather than the fluid acceleration only (chosen by Zielke in [109]) as previously suggested in [44]. This result with simple physical interpretation however necessitates to solve for the FSI problem

in order to find the wall longitudinal acceleration. This has been solved in [65] where the relative FSI contribution to the wall shear-stress has been analyzed as illustrated in figure (19) and (20). Figure (19) displays the time variations of the transient wall shear-stress, showing huge peaks synchronized with the wave front's passages. When comparing the FSI and non-FSI results for two distinct density ratio $\mathcal{D}$, one finds that the FSI relative contribution increases as $\mathcal{D}$ rises to $O(1)$ (more precisely [65] have analyzed the case $\mathcal{D} = 1$). Figure 20 analyzed further the relative FSI contribution to the wall shear-stress. It shows that this relative contribution can become as large as 50% for a relative wall thickness of 10% and Poisson modulus $\nu_s = 0.3$. These results suggest that for the in-vivo biomedical context of blood pressure pulse wave propagation within vascular network, the FSI contribution to transient wall-shear stress cannot be ignored.

4.4. Theoretical analysis of junction coupling within complex networks

This section covers how wave propagation within networks can be formulated within a pipe network described by a graph. Most of the content of this section discusses the success toward an "algebraic" (a wording to be clarified later on in section 4.4.2) formulation of water-hammer wave propagation within graphs.

Section 4.4.1 discuss the frequency domain approach whereas section 4.4.2 reviews time-domain one. In the following we denote usual graphs $G(\mathcal{V}, \mathcal{E})$ having vertex set $\mathcal{V}$ and edge one $\mathcal{E}$ the cardinal of which are respectively denoted V and E. The graph adjacency matrix is denoted $\mathbf{A}$. In section 4.4.2 the concept of metric graph denoted $\mathcal{G}(\mathcal{V}, \mathcal{E})$ will also be introduced.

4.4.1. Discrete graph-wave solutions for wave propagation within networks

One of the first generalizations of the TM method to networks has first been performed into simple networks such as those analyzed by S. Kim 21. The looped network along with its spectrum, i.e. linear network admittance system for [169, 170]'s analysis is depicted in Figure 21. [171] develop a frequency-domain network admittance formulation (from Laplace transform) to solve the first order coupled hyperbolic pressure/velocity problem (82) (expressed as a

pressure/flux in [171]) within general water distribution networks. A series impedance approach leads to a graph-node spatial discretization of the one-dimensional gradients, and also to some analytical node-to-node relation along each pipe-line similar to TMM's solutions (47)-(48) (except for being related to pressure/flux vector rather than pressure/stress since (47)-(48) are related to FSI's TMM). More explicitly following [172, 173], the Laplace transform of (82) for each network link e_{ij} joining nodes i and j, parametrized by dimensionless coordinate Z, leads to a parametric linear relation between the pressure p_{ij}, the flux $q_{ij}$and their gradients

$$Z_{ij}(Z,s)q_{ij}(Z) = -\partial_Z p_{ij}(Z) \quad , \quad Y_{ij}(Z,s)p_{ij}(Z) = -\partial_Z q_{ij}(Z), \tag{263}$$

defining the shunt admittance per unit-length Y_{ij} related to the compressibility in the flow produced by pressure variations, and Z_{ij} the impedance per unit length. These quantities permit to evaluate the "propagation operator" $\Gamma_{ij} = \sqrt{Y_{ij}Z_{ij}}$ [172, 173]. [171] has found the frequency-domain graph admittance matrix $\mathfrak{Y}$ related to the adjacency matrix $\mathbf{A}$ as

$$\mathfrak{Y}_{ij} = -\delta_{ij}\left(\sum_{m\in\mathfrak{N}(i)} A_{im}\frac{1}{Z_{ij}(s)\tanh(\Gamma_{\mathrm{ij}}(\mathrm{s}))}\right) + A_{ij}\frac{1}{Z_{ij}(s)\sinh(\Gamma_{ij}(s))}. \tag{264}$$

Introducing the pressure field at each node of the network as vector ϕ whose components are ϕ_j for j in the vertex set of the graph, i.e $j \in [1, V]$, Matrix $\mathfrak{Y}$ relates each pressure/flux at network's nodes as

$$\mathfrak{Y}(s)\phi = \mathbf{Q}. \tag{265}$$

In [171] (265) is used to build a frequency domain network transfer matrix for transient computation inside network, when including boundary conditions. [174] consider the extension of [171]'s framework, supplementing the "passive" graph nodes with "compound nodes" for which a dynamical behavior with non-linear (more precisely quadratic non-linearities) relations between input/output is specified. These "compound nodes" are modeling complex hydraulic components —such as junctions, air vessels, valves — in water distribution networks.

There are taken care-off in [174] from an expansion of the graph nodes with supplementary nodes associated with the new degree of freedom of each "compound nodes". When linearizing the "compound nodes" [174] provides an extension of [171] from generalizing the frequency-domain graph admittance matrix $\mathfrak{Y}$ (264). [174] also provides direct comparison between time-domain numerical computation of the complete non-linear transient problem solved with the MOC method and the frequency-domain graph admittance matrix method. The numerical results of [174] illustrate that the higher the pressure, the higher the error associated with non-linearities, as expected. They also suggest that, for realistic pressure range of water-hammer within water distribution networks, neglecting the compound nodes's non-linearities does not produce a large error. This observation should obviously be strengthened in order to more precisely know under which precise conditions these non-linearities have to be taken into account.

[176, 175] have developed a numerical Inverse Laplace Transform (NILT) procedure allowing a time-domain numerical evaluation of the previously described frequency-domain network admittance formulation for networks, as illustrated in Figure 22. Figure 22 shows that the low-frequency components of the pressure signal can be well approximated by the (NILT) method. [177] recently used the NILT method [176, 175] to investigate the transient behavior of an Y-pipe experimental setup. In the following section, we now describe how time-domain graph's solutions can also be developed.

4.4.2. Spectral quantum graph method for solving wave propagation within networks

Quantum graphs is the name for operators equipping a metric graph, i.e a graph whose one-dimensional edges have a physical length. This theoretical concept has been used to study vibrations and spectrum structure of metric graphs [178], quantum chaos e.g [179, 180], wave scattering [181, 182], and more recently wave propagation in networks [183, 184, 185]. Even if the application of this method for water-hammer propagation modeling is still very recent, since it is a promising one (because it opens future theoretical advances to be

made into wave's propagation within complex networks, where most previous investigations could only address them from direct numerical simulation, —e.g with MOC method—), it is hereby discussed in more details following the time-domain approach proposed in [185]. The interest of quantum graph method over traditional numerical modeling already discussed in section 2.2.2 is that the wave solution is searched as a decomposition onto a continuous base defined over the entire metric graph. Each element of the base is denoted $\mathbf{\Psi}_\lambda$. It generalizes into a network the eigenfunction of the Laplacian operator previously considered in (58). On the contrary to traditional approaches this base, does not need to be discretized along each edge e_{ij} joining vertex i and j of the graph since it displays an analytical shape along those, i.e it is a spectral base. Such spectral discretization along each network's edge can save a huge numerical cost for large networks as discussed in [184]. The approach is nevertheless yet restricted to address linear wave operators solutions. Furthermore on the contrary to traditional numerical discrete approaches, a quantum graph formulation permits to establish general results, as the ones found in [185], that numerical computations can only illustrate. Before describing more theoretically this concept, let-us first illustrate it on a simple 3-star graph depicted in figure 23. Figure 24 shows the first two eigenmodes $\mathbf{\Psi}_{\lambda_1}$ and $\mathbf{\Psi}_{\lambda_2}$ onto the 3-star metric graph of figure 23. One can observe in figure 24 that each eigenmode is continuous along each internal node of the graph (i.e in this example, only node O), and also that the sum of the derivatives on each node is zero, which is precisely why these modes are called Kirchhoff eigenmodes. Let-us now provide more information about eigenmode $\mathbf{\Psi}_\lambda$, denoting $\Psi_{ij}(x)$ its component along each edge e_{ij} of length ℓ_{ij}joining vertex i and j of the graph. Each $\Psi_{ij}(x)$ fulfills to be an eigenfunction of the one dimensional Laplacian

$$-\frac{d^2}{dx^2}\Psi_{ij}(x) = \lambda^2 \Psi_{ij}(x). \tag{266}$$

Furthermore, inside any vertex, there is a Dirichlet continuity at vertex i and j

$$\Psi_{ij}(0) = \phi_i \qquad \Psi_{ij}(\ell_{ij}) = \phi_j. \tag{267}$$

Denoting A_{ij} the components of the graph adjacency matrix $\mathbf{A}$, boundary conditions at each vertex i reads

$$-\sum_{j<i} A_{ij} \frac{d}{dx} \Psi_{ij}(\ell_{ij}) + \sum_{j>i} A_{ij} \frac{d}{dx} \Psi_{ij}(0) = h_i \phi_i. \tag{268}$$

Condition (268) is called a Kirchhoff-Robin condition. For $h_i = 0$, it degenerates into a Kirchhoff condition. In the limit $h_i \to \infty$, it provides a Dirichlet condition at vertex i where it imposes $\phi_i = 0$. Given continuity conditions (267), the spectral base $\Psi_{ij}(x)$ is

$$\Psi_{ij}(x) = \frac{A_{i,j}}{\sin(\lambda \ell_{ij})} \left(\phi_i \sin(\lambda(\ell_{ij} - x)) + \phi_j \sin(\lambda x) \right). \tag{269}$$

The restriction of Ψ_λ over the vertex set $\mathcal{V}$ i.e $\Psi_\lambda|_\mathcal{V}$ defines a V-component vector denoted ϕ_λ having ϕ_j amplitudes with $j \in [1, V]$ where V is the cardinal of $\mathcal{V}$. Furthermore parameter λ not yet specified, needs to be set so that the operator boundary conditions (268) at each vertex are satisfied. It can be shown (Cf [186, 187, 188, 189, 185] for more information) that specific values of λ called the quantum graph operator spectrum permits these conditions to arise. Defining secular matrix $\mathfrak{A}$ as

$$\mathfrak{A}_{ij}(\lambda, \mathbf{h}) = -\delta_{ij} \left(\sum_{m \in \mathfrak{N}(i)} A_{im} \mathrm{cot}(\lambda \ell_{\mathrm{im}}) + \frac{\mathrm{h_i}}{\lambda} \right) + A_{ij} \frac{1}{\sin(\lambda \ell_{ij})}. \tag{270}$$

where $\mathfrak{N}(i) = \{m \backslash A_{im} \neq 0\}$ being the neighbors of vertex i associated with non-zero components of adjacency matrix $\mathbf{A}$. The analogy between the secular time-domain matrix (270) and the frequency domain one (264) should be pointed out. Matrix $\mathfrak{A}$ is built so that (268) is equivalent to

$$\sum_{j=1}^{V} \mathfrak{A}_{ij} \phi_j = \mathfrak{A} \phi_\lambda = 0, \tag{271}$$

where, again, ϕ_λ is the V-component vector of amplitudes ϕ_j. (271) can have a non-trivial solution different from zero when the so-called secular condition is met

$$\mathrm{det}\mathfrak{A}(\lambda, \mathbf{h}) = 0. \tag{272}$$

(272) provides an algebraic formulation for the wave's spectrum. It is very nice to observe that this condition generalizes to any metric graph the one used for a single pipe for FSI TMM solutions (56) or the time-domain ones (69). There is indeed a deep mathematical reason for this, since the associate operator having linear boundary conditions, they can be expressed as resulting from the action of a matrix acting on the field value (and possibly its gradient). It results in the common feature that the discrete possible frequencies called the spectrum is found from an algebraic zero determinant condition. (272) provides the spectrum of (infinite) discrete set of values of positive ordered λ such that $0 \leq \lambda_1 < \lambda_2 \ldots$. Let-us illustrate more precisely this concept on the 3-star graph illustrated in figure 23 whose adjacency matrix is

$$\mathbf{A} = \begin{bmatrix} 0 & 1 & 0 & 0 \\ 1 & 0 & 1 & 1 \\ 0 & 1 & 0 & 0 \\ 0 & 1 & 0 & 0 \end{bmatrix}. \tag{273}$$

Using definition (270) the secular matrix reads in this case

$$\mathfrak{A}(\lambda, \mathbf{h}) = \begin{bmatrix} -\cot(\ell_{21}\lambda) & \frac{1}{\sin(\ell_{21}\lambda)} & 0 & 0 \\ \frac{1}{\sin(\ell_{21}\lambda)} & -\frac{h_m}{\lambda} - \cot(\ell_{21}\lambda) - \cot(\ell_{32}\lambda) - \cot(\ell_{24}\lambda) & \frac{1}{\sin(\ell_{32}\lambda)} & \frac{1}{\sin(\ell_{24}\lambda)} \\ 0 & \frac{1}{\sin(\ell_{32}\lambda)} & -\cot(\ell_{32}\lambda) & 0 \\ 0 & \frac{1}{\sin(\ell_{24}\lambda)} & 0 & -\cot(\ell_{24}\lambda) \end{bmatrix} \tag{274}$$

whose determinant is

$$\det\mathfrak{A}(\lambda, \mathbf{h}) = \left[((\frac{\mathrm{h_m}}{\lambda}\cot(\ell_{24}\lambda) - 1)\cot(\ell_{23}\lambda) - \cot(\ell_{24}\lambda))\cot(\ell_{21}\lambda) - \cot(\ell_{23}\lambda)\cot(\ell_{24}\lambda) \right]. \tag{275}$$

Numerically solving for $\det\mathfrak{A}(\lambda_\mathrm{n}, \mathbf{0}) = 0$ gives the eigenvalues λ_n of the Kirchhoff modes. This spectrum is complemented with the vertex vector ϕ_{λ_n} of quantum graph modes n (269) obtained from computing the one dimensional null-space of matrix $\mathfrak{A}(\lambda_n, \mathbf{0})$ (here a 4-vector) which then sets $\mathbf{\Psi}_{\lambda_n}$. [185] provides tables with λ_n and ϕ_{λ_n} values of the first twenty Kirchhoff modes. Figure 24 illustrates the first two Kirchhoff mode $\mathbf{\Psi}_{\lambda_1}$ and $\mathbf{\Psi}_{\lambda_2}$, showing as expected an increasing

number of minimum and maximum as λ_n increases. The spectral base of the quantum graph then permits to find the time-domain pressure-wave solution as decomposed into it. In [185] the two-time scale analysis has furthermore been used to analyze the damped wave pressure problem (83) within the entire network. Following the very same steps as in section 4.1, the pressure solution is decomposed into

$$\mathbf{P}_{\mathcal{G}} = \mathbf{P}^0_{\mathcal{G}} + \delta \mathbf{P}^1_{\mathcal{G}} + \dots \tag{276}$$

912 In [185] each term of the expansion (276) is then decomposed into an homoge-
913 neous and a particular solution similarly as (162) and (186)

$$\begin{aligned} \mathbf{P}^0_{\mathcal{G}} &= \sum_{n\in\mathbb{N}} \left(A_n(T) a_n e^{i\lambda_n \tau} + A_n(T)^\star a_n^\star e^{-i\lambda_n \tau} \right) \mathbf{\Psi}_{\lambda_n} + \mathbf{P}_p \\ \mathbf{P}^0_{\mathcal{G}} &= \sum_{n\in\mathbb{N}} \left(A_n(T) a_n e^{i\lambda_n \tau} + cc \right) \mathbf{\Psi}_{\lambda_n} + \mathbf{P}_p, \end{aligned} \tag{277}$$

where cc stands for complex-conjugate, and where $\mathbf{\Psi}_{\lambda_n}$ is the Kirchoff quantum-graph base for which the vertex boundary condition (268) is a Kirchoff one, i.e $h_i = 0$ for every vertex $i \in V$. The Kirchoff spectrum given by condition (272) results from the intrinsic graph structure of the network. Furthermore, the particular solution $\mathbf{P}_p$ has been computed in [185] for a given time-domain triggering event arising at a given origin vertex v_O of the graph where a closure law $P_O(t)$ is imposed so that there is locally a non-zero flow acceleration (typically related to a valve opening or closure) leading to

$$\sum_{e_k} \frac{\partial \mathbf{P}^0_{\mathcal{G}}}{\partial x}(\mathbf{x}_{v_O}, \tau) = P_O(\tau), \tag{278}$$

[185] found that the particular solution $\mathbf{P}_p$ can also be decomposed into a distinct quantum graph base being a Kirchoff-Robin-Fourrier one denoted $\mathbf{\Psi}^p_{\lambda_m}$ that will not be detailed here. At first order one gets (83)

$$\left(\frac{\partial^2}{\partial \tau} - \frac{\partial^2}{\partial x^2} \right) p^1_k = 2 \left(\frac{\partial \tau^0_w}{\partial x} - \frac{\partial}{\partial T} \frac{\partial}{\partial \tau} p^0_k \right), \tag{279}$$

where within each edge, the pressure leading order and first order are respectively denoted p^0_k and p^1_k for $k \in E$. Since, the first order problem is then

decomposed into the Laplacian eigenfunctions

$$\mathbf{P}^1_{\mathcal{G}} = \sum_{n\in\mathbb{N}} [a^1_n(\tau) + cc]\mathbf{\Psi}_{\lambda_n} + \sum_{m\in\mathbb{N}} [a^{1p}_m(\tau) + cc]\mathbf{\Psi}^p_{\lambda_m}. \tag{280}$$

From (277), one can evaluate the right-hand-side of (279) in the Laplace domain which reads, using the Laplace transform of the wall-shear-stress (243)

$$\begin{aligned} 2\left(\frac{\partial \tilde{\tau}^0_w}{\partial x} - \frac{\partial}{\partial T} s\tilde{\mathbf{P}}^0_{\mathcal{G}}\right) &= 2\left(\sum_{n\in\mathbb{N}} [\frac{a^0_n}{s-i\lambda_n}(A^0_n\frac{\sqrt{s}}{s}\lambda^2_n - s\frac{\partial A^0_n}{\partial T}) + cc]\mathbf{\Psi}_{\lambda_n}\right. \\ &\left. + \sum_{m\in\mathbb{N}} [\frac{a^{0p}_m}{s-i\lambda^p_m}(A^0_m\frac{\sqrt{s}}{s}\lambda^{p2}_m - s\frac{\partial A^{0p}_m}{\partial T}) + cc]\mathbf{\Psi}_{\lambda^p_m}\right) \end{aligned} \tag{281}$$

Writing (279) in Laplace domain whilst using (281), the first-order problem written on $\mathcal{G}$ reads

$$\begin{aligned} \left(s^2 - \Delta_{\mathcal{G}}\right)\mathbf{P}^1_{\mathcal{G}} &= 2\left(\sum_{n\in\mathbb{N}} [\frac{a^0_n}{s-i\lambda_n}(A^0_n\frac{\sqrt{s}}{s}\lambda^2_n - s\frac{\partial A^0_n}{\partial T}) + cc]\mathbf{\Psi}_{\lambda_n} + \right. \\ &\left. \sum_{m\in\mathbb{N}} [\frac{a^{0p}_m}{s-i\lambda^p_m}(A^{0p}_m\frac{\sqrt{s}}{s}\lambda^{p2}_m - s\frac{\partial A^{0p}_m}{\partial T}) + cc]\mathbf{\Psi}_{\lambda^p_m}\right). \end{aligned} \tag{282}$$

Projecting (282) over $\mathbf{\Psi}_{\lambda_n}$ permits to find the secularity solution to cancel the resonant double poles, [185] found

$$\begin{aligned} \lim_{s\to i\lambda_n}\left(A_n\frac{\sqrt{s}}{s}\lambda^2_n - s\frac{\partial A_n}{\partial T}\right) = 0, \\ \lim_{s\to -i\lambda_n}\left(A^\star_n\frac{\sqrt{s}}{s}\lambda^2_n - s\frac{\partial A^\star_n}{\partial T}\right) = 0, \end{aligned} \tag{283}$$

leading to the same consistent secularity solution

$$A_n(T) = e^{-\sqrt{-i\lambda_n}T} = e^{-(\frac{1-i}{\sqrt{2}})\sqrt{\lambda_n}T}, \tag{284}$$

Now, using (284) in (277) leads to the damped leading-order solution for the wave solution

$$\begin{aligned} \mathbf{P}^0_{\mathcal{G}} = &\sum_{n\in\mathbb{N}} e^{-\sqrt{\frac{\lambda_n}{2}}T}\left(a^0_n e^{i\sqrt{\frac{\lambda_n}{2}}T}e^{i\lambda_n t} + cc\right)\mathbf{\Psi}_{\lambda_n} \\ &+ \sum_{m\in\mathbb{N}} e^{-\sqrt{\frac{\lambda^p_m}{2}}T}\left(a^{p0}_m e^{i\sqrt{\frac{\lambda^p_m}{2}}T}e^{i\lambda^p_m t} + cc\right)\mathbf{\Psi}_{\lambda^p_m}. \end{aligned} \tag{285}$$

It is noteworthy to mention that (285) generalizes for a network the damping analysis described in section 4.1 and 4.3 for a single pipe. Nevertheless, one

deep relation between the presented results is that the homogeneous spectrum results from the applied boundary conditions.

5. Conclusion and perspectives

This review dedicated to the mechanics underpinning water-hammer waves has provided both a short historical survey as well as the author's state-of-the-art of the current understanding of this complex topic. Since water-hammer involves both wave propagation within the solid and the fluid, it does involve FSI at the liquid-solid interface and necessitates to take into account both the influence of non-stationary boundary layers and inlet/outlet FSI boundary conditions.

The first two sections of this review have emphasized and summarized the crucial role of three couplings (Poisson, junction, friction) as already stressed in previous reviews [12, 13, 15, 16, 18]. This review has not only covered the established sets of equations for water-hammer modeling, their possible derivation from first principles, but also, their possible theoretical solutions. This viewpoint is perhaps the most original stance since previous ones most often discussed water-hammer's numerical computation.

Furthermore recent developments related to the influence of visco-elastic properties of the pipe's wall, asymptotic analysis of water-hammer, as well as the theoretical analysis of wave propagation within networks have also been discussed. Concerning the visco-elastic solid, this review has emphasized that even though Kelvin-Voigt models for the creep-functions are widespread in the literature (and indubitably operational) it is interesting to consider rheological visco-elastic models for providing an intrinsic description which does not depend on the specific water-hammer test (since, as opposed to Kelvin-Voigt models, visco-elastic models do not depend on the water-hammer test detail, i.e closure law, pipe thickness, length, diameter, etc...).

In the future the rheological visco-elastic parameters might possibly be estimated from Dynamical Mechanical Analysis (DMA) independently of the water

hammer test, so that one could try to model visco-elastic water-hammer without parameter fitting (as opposed to the traditional Kelvin-Voigt model's approach). This is indeed an interesting perspective to mention.

Concerning the asymptotic analysis of water-hammer this review has tried to emphasize the relationship between previous contributions in the literature addressing traditional boundary layer asymptotic matching, two-time scale analysis, or both. Recent advances have permitted the asymptotic perturbative derivation of the four equation FSI model. They have also permitted to bring to the fore that some distinct asymptotic regimes could happen, as emphasized in this review. In the future, some further developments could maybe permit a deeper understanding of the couplings between the steady-state flow and the water-hammer wave, perhaps leading to the derivation of a quasi-steady shear stress model alternative to the quasi-steady Darcy-Weisbach model. The use of asymptotic analysis might also be useful in the future to approximate reflection/transmission coefficients resulting from the presence of singularities (e.g sudden diameter changes, blockages, etc.) within networks in order to provide improved long-wavelength approximation models for water-hammer waves.

Last but not least, this review has covered the theoretical analysis of water-hammer propagation within networks. This topic is stimulating since a modern viewpoint recently brought new concepts and results in this interesting area. Among those, the notion that the wave spectrum within networks can be found from an algebraic condition related to the secular matrix (which is related to the graph adjacency matrix) has been emphasized. There is much to develop in this area, in order to progress along water-hammer modeling in complex networks. We believe this research topic will grow in the future. It might also impact the related growing topic of transient-based defect detection methods.

Acknowledgments

The author has no competing interests to declare. The author which to thanks A. Bayle for sharing part of his PhD's figures.

References

[1] R. Guibert, A. Bayle, F. Plouraboué, Geolocalization of water-waves origin within water distribution networks using time reversal of first event detection, Water Res. 230 (2023).

[2] L. Allievi, Teoria del colpo d'ariete, Tipografia della R. Accademia dei Lincei, 1913.

[3] C. Camichel, D. Eydoux, M. Gariel, étude théorique et expérimentale des coups de bélier., Annales de la Faculté des sciences de Toulouse : Mathématiques 9 (1917) 1–145.

[4] H. Résal, Note sur les petits mouvements d'un fluide incompressible dans un tuyau élastique., Journal de Mathematiques Pures et Appliquées 2 (1876) 342–344.

[5] J. Michaud, Coups de bélier dans les conduites. Étude des moyens employés pour en atténuer les effects, Bulletin de la Société Vaudoise des Ingénieurs et des Architects 4 (3) (1878) 4.

[6] D. Korteweg, Ueber die Fortpflanzungsgeschwindigkeit des Schalles in elastischen Rohren, On the speed of sound propagation in elastic tubes, Annalen der Physik 241 (12) (1878) 525–542.

[7] N. Joukowsky, Uber den hydraulischen Stoss in Wasserleitungsro hren. (on the hydraulic hammer in water supply pipes) Mémoires de l'Académie Impériale des Sciences de St.-Petersbourg., English translation, partly, by Simin 9 (5) (1904).

[8] C. Bacon, Separation of waves propagating in an elastic or viscoelastic hopkinson pressure bar with three-dimensional effects, INTERNATIONAL JOURNAL OF IMPACT ENGINEERING 22 (1) (1999) 55–69.

[9] H. Zhao, G. Gary, On the use of shpb techniques to determine the dynamic behavior of materials in the range of small strains, Int. J. Solids Struct. 33 (23) (1996) 3363–3375.

[10] R. Skalak, An extension of the theory of waterhammer, J. Fluids Eng. Trans. ASME 78 (1956) 105–116.

[11] R. Skalak, AN EXTENSION OF THE THEORY OF WATER HAMMER, Ph.D. thesis, Columbia University (1954).

[12] A. S. Tijsseling, Fluid-structure interaction in liquid-filled pipe systems: a review, J. Fluids Struct. 10 (2) (1996) 109–146.

[13] M. S. Ghidaoui, M. Zhao, D. A. McInnis, D. H. Axworthy, A review of water hammer theory and practice, Applied Mechanics Reviews 58 (1) (2005) 49–76.

[14] H. Bergant, A. R. Simpson, A. Tijsseling, Water hammer with column separation: A historical review, J. Fluids Struct. 22 (2006) 135–171.

[15] S. Li, B. W. Karney, G. Liu, FSI research in pipeline systems – A review of the literature, J. Fluids Struct. 57 (2015) 277–297.

[16] H.-F. Duan, B. Pan, M. Wang, L. Chen, F. Zheng, Y. Zhang, State-of-the-art review on the transient flow modeling and utilization for urban water supply system (UWSS) management, J. Water Supply: Res. Technol. - AQUA 69 (8) (2020) 858–893. doi:10.2166/aqua.2020.048.

[17] D. Ferras, P. A. Manso, A. J. Schleiss, D. I. C. Covas, One-Dimensional Fluid–Structure Interaction Models in Pressurized Fluid-Filled Pipes: A Review, Appl. Sci. 8 (10) (2018) 1844. doi:10.3390/app8101844.

[18] F. N. Van De Vosse, N. Stergiopulos, Pulse wave propagation in the arterial tree, Annu. Rev. Fluid Mech. 43 (2011) 467–499.

[19] A. Tijsseling, Fluid-structure interaction in case of waterhammer with cavitation, Ph.D. thesis, Delft University of Technology (1993).

[20] E. M. Wahba, Non-newtonian fluid hammer in elastic circular pipes: Shear-thinning and shear-thickening effects, J. Non-Newton. Fluid Mech. 198 (2013) 24–30.

[21] T. G. Beuthe, Review of two-phase water hammer, Tech. rep., Proceedings of the 18th Annual CNS Conference, Toronto, Ontario, Canada (1997).

[22] A. Abebe, Y. Tadesse, A. Beyene, Conversion of thermally amplified hydraulic shock for power generation: Modeling and experimental analyses, J. Energy Resour. Technol. 145 (2) (2023).

[23] G. Touya, T. Reess, L. Pecastaing, A. Gibert, P. Domens, Development of subsonic electrical discharges in water and measurements of the associated pressure waves, J. Appl. Phys. 39 (24) (2006) 5236–5244.

[24] L. F. Menabrea, Note sur les effets du choc de l'eau dans les conduites, Mallet-Bachelier, 1858.

[25] A. Tijsseling, A. Anderson, A. Isebree Moens and D.J. Korteweg: On the speed of propagation of waves in elastic tubes, in: 11^{th} International Conferences on Pressure Surges, BHR Group, 2012, pp. 227–245.

[26] A. Bayle, Modélisation des ondes de pression transitoires dans les réseaux de distribution d'eau, Ph.D. thesis, Institut Polytechnique de Toulouse (2023).

[27] D. Wiggert, A. Tijsseling, Fluid transients and fluid-structure interaction in flexible liquid-filled piping, Applied Mechanics Reviews 54 (5) (2001) 455–481. doi:10.1115/1.1404122.

[28] H. Lamb, On the velocity of sound in a tube, as affected by the elastic of the walls., Memoirs of the Manchester Literary and Philosophical Society, Manchester, (UK) 42 (9) (1898) 1–16.

[29] W. Flügge, Stresses in Shells, Springer Berlin, Heidelberg, 1960. doi:10.1007/978-3-662-01028-0.

[30] M. P. Paidoussis, Fluid-Structure Interactions, Volume 2: Slender Structures and Axial Flow, Elsevier, 2003.

[31] D. Covas, I. Stoianov, J. F. Mano, H. Ramos, N. Graham, C. Maksimovic, The dynamic effect of pipe-wall viscoelasticity in hydraulic transients. Part II model development, calibration and verification, J. Hydraul. Res. 43 (1) (2005) 56–70.

[32] T. Lin, G. W. Morgan, Wave propagation through fluid contained in a cylindrical, elastic shell, J. Acoust. Soc. Am. 28 (1956) 1165–1176.

[33] A. R. D. Thorley, Pressure Transients in Hydraulic Pipelines, J. Basic Eng. 91 (3) (1969) 453–460. doi:10.1115/1.3571153.

[34] R. P. DeArmond, W. T. Rouleau, Wave Propagation in Viscous, Compressible Liquids Confined in Elastic Tubes, J. Basic Eng. 94 (4) (1972) 811–816. doi:10.1115/1.3425565.

[35] D. J. Williams, Waterhammer in Non-Rigid Pipes Precursor Waves and Mechanical Damping, J. Mech. Eng. Sci. 19 (6) (1977) 237–242. doi:10.1243/JMES_JOUR_1977_019_051_02.

[36] S. Rubinow, J. Keller, Wave Propagation in a Fluid-Filled Tube, Journal of the Acoustical Society of America 50 (1971) 198–223. doi:10.1121/1.1912620.

[37] S. I. Rubinow, J. B. Keller, Wave propagation in a viscoelastic tube containing a viscous fluid, J. Fluid Mech. 88 (1) (1978) 181–203.

[38] W. Bürmann, Water hammer in coaxial pipe systems, J. Hydraul. Div. 101 (6) (1975) 699–715. doi:10.1061/JYCEAJ.0004372.

[39] G. Kuiken, Approximate dispersion equations for thin-walled liquid-filled tubes., Appl. Sci. Res. 41 (1984) 37–53.

[40] G. Kuiken, Wave propagation in a thin-walled liquid-filled initially-stressed tube, J. Fluid Mech. 141 (1984) 289–308.

[41] G. Kuiken, Wave propagation in initially stressed orthotropic compliant tubes containing a compressible, viscous and hear-conducting fluid, Ph.D. thesis, Delft University of Technology (1984).

[42] O. Thual, Introduction à la Mécanique des milieux continus déformables, Cépadués-Editions, 1997.

[43] A. Tijsseling, Water hammer with fluid-structure interaction in thick-walled pipes, Comput. Struct. 85 (2007) 844–851.

[44] D. D. Budny, D. C. Wiggert, F. J. Hatfield, The Influence of Structural Damping on Internal Pressure During a Transient Pipe Flow, J. Fluids Eng. 113 (3) (1991) 424–429. doi:10.1115/1.2909513.

[45] S. Li, B. W. Karney, G. Liu, FSI research in pipeline systems – A review of the literature, J. Fluids Struct 57 (2015) 277–297.

[46] A. S. Tijsseling, Exact solution of linear hyperbolic four-equation system in axial liquid-pipe vibration, J. Fluids Struct. 18 (2) (2003) 179–196.

[47] L. Zhang, A. Tijsseling, A. Vardy, FSI analysis of liquid-filled pipes, J. Sound Vib. 224 (1) (1999) 69–99. doi:10.1006/jsvi.1999.2158.

[48] Q. S. Li, K. Yang, L. Zhang, Analytical Solution for Fluid-Structure Interaction in Liquid-Filled Pipes Subjected to Impact-Induced Water Hammer, J. Eng. Mech. 129 (12) (2003) 1408–1417.

[49] H. K. Aliabadi, A. Ahmadi, A. Keramat, Frequency response of water hammer with fluid-structure interaction in a viscoelastic pipe, Mech. Syst. Signal Process. 144 (2020).

[50] A. Bayle, F. Plouraboué, Spectral properties of Fluid Structure Interaction pressure/stress waves in liquid filled pipes, Wave motion 116 (2023) 103081.

[51] E. Wylie, V. Streeter, Fluid Transients in Systems, Prentice-Hall Inc., Englewood Cliffs, New Jersey, USA., 1993.

[52] M. Chaudhry, Applied Hydraulic Transients 2nd edn., Van Nostrand Reinhold Co., New York, USA., 1987.

[53] A. Bayle, F. Plouraboué, Laplace-domain fluid–structure interaction solutions for water hammer waves in a pipe, J. Hydraul. Eng. 150 (2) (2024) 04023062.

[54] L. Gongmin, L. Yanhua, Vibration analysis of liquid-filled pipelines with elastic constraints, J. Sound Vib. 330 (13) (2011) 3166–3181.

[55] Q. Li, K. Yang, L. Zhang, N. Zhang, Frequency domain analysis of fluid–structure interaction in liquid-filled pipe systems by transfer matrix method, Int J Mech. Sci. 44 (2002) 2067–2087.

[56] Y. Y. Huang, G. Zeng, F. Wei, A new matrix method for solving vibration and stability of curved pipes conveying fluid, J. Sound Vib. 251 (7) (2002) 215–225.

[57] M. El-Raheb, Vibrations of three-dimensional pipe systems with acoustic coupling, J. Sound Vib. 78 (1) (1981) 39–67.

[58] H. Duan, P. J. Lee, M. S. Ghidaoui, Y. Tung, Extended Blockage Detection in Pipelines by Using the System Frequency Response Analysis, J. Water Resour. Plan. Manag. 138 (1) (2012) 55–62. doi:10.1061/(ASCE)WR.1943-5452.0000145.

[59] K. Yang, Q. S. Li, L. Zhang, Longitudinal vibration analysis of multi-span liquid-filled pipelines with rigid constraints, J. Sound Vib. 273 (1-2) (2004) 125–147. doi:10.1016/S0022-460X(03)00422-X.

[60] G. Koo, B. Yoo, Vibration characteristics of pipe element containing moving medium by a transfer matrix, Int. J. Presse. Vessels Pip. 77 (2000) 679–689.

[61] H. L. Dai, L. Wang, Q. Qian, J. Gan, Vibration analysis of three-dimensional pipes conveying fluid with consideration of steady combined

force by transfer matrix method, Appl. Math. Comput. 219 (5) (2012) 2453–2464. doi:10.1016/j.amc.2012.08.081.

[62] A. Keramat, B. Karney, M. S. Ghidaoui, X. Wang, Transient-based leak detection in the frequency domain considering fluid-structure interaction and viscoelasticity, Mech Syst Signal Process 153 (2021) 107500. doi:10.1016/j.ymssp.2020.107500.

[63] A. Keramat, H. F. Duan, Spectral based pipeline leak detection using a single spatial measurement, Mech. Syst. Signal Process. 161 (2021) 107940.

[64] N. Joukowsky, Über den hydraulischen stoss in wasserleitungsröhren, Mémoires de l'Académie Impériale des Sciences de St.-Pétersbourg 8 (9(5)) (1900) 1–71.

[65] A. Bayle, F. Plouraboué, Low–mach number asymptotic analysis of Fluid–Structure-Interaction (FSI) pressure waves inside an elastic tube, Eur. J. Mech. B Fluids 101 (2023).

[66] D. Wiggert, R. Otwell, F. Hatfield, The effect of elbow restraint on pressure transients, J. Fluids. Eng. 107 (2) (1985) 402–406.

[67] A. Tijsseling, A. Vardy, D. Fan, Fluid-structure interaction and cavitation in a single-elbow pipe system, J. Fluids Struct. 10 (4) (1996) 395–420. doi:10.1006/jfls.1996.0025.

[68] M. Shimada, J. Brown, A. Vardy, Estimating friction errors in MOC analyses of unsteady pipe flows, Comput. Fluids. 36 (7) (2007) 1235–1246. doi:10.1016/j.compfluid.2006.11.005.

[69] K. Urbanowicz, I. Haluch, A. Bergant, A. Deptula, P. Sliwinski, Initial investigation of wave interactions during simultaneous valve closures in hydraulic piping systems, Water Resour. Manag. 37 (13) (2023) 5105–5125.

[70] H. Cao, I. Nistor, M. Mohareb, Effect of Boundary on Water Hammer Wave Attenuation and Shape, J. Hydraul. Eng. 147 (3) (2020) 04020001.

[71] N. Nassif, F. Pini, Semi-discrete and fully discrete finite-element methods with penalty for the numerical-solution of the water-hammer problem, SIAM J. Numer. Anal . 18 (1) (1981) 111–128.

[72] U. Lee, J. Kim, Dynamics of branched pipeline systems conveying internal unsteady flow, J. Vib. Acoust. 121 (1999) 114–122.

[73] X. Zhang, Parametric studies of coupled vibration of cylindrical pipes conveying fluid with the wave propagation approach., Comput Struct. 80 (2002) 287–295.

[74] L. Zhang, W. Huang, Analysis of nonlinear dynamic stability of liquid-converying pipes, Applied Mathematics and Mechanics 23 (2002) 1071–1080.

[75] Y. Zhang, D. Gorman, J. Reese, A finite element method for modelling the vibration of initially tensioned thin-walled orthotropic cylindrical tubes conveying fluid., J. Sound Vib. 245 (2002) 93–112.

[76] J. Kochupillail, N. Ganesan, C. Padmanabhan, A new finite element formulation based on the velocity of flow for water hammer problems, Int. J. Press. Vessel. 82 (1) (2005) 1–14.

[77] R. Szymkiewicz, M. Mitosek, Analysis of unsteady pipe flow using the modified finite element method, Commun. numer. methods eng. 21 (4) (2005) 183–199.

[78] V. Guinot, Riemann solvers for water hammer simulations by Godunov method, Int J Numer Methods Eng. 49 (7) (2000) 851–870.

[79] M. Zhao, M. Ghidaoui, Godunov-type solutions for water hammer flows, J. Hydraul. Eng. 130 (4) (2004) 341–348.

[80] C. Bourdarias, S. Gerbi, A conservative model for unsteady flows in deformable closed pipes and its implicit second-order finite volume discretisation, Comput. Fluids. 37 (10) (2008) 1225–1237.

[81] M. Ioriatti, M. Dumbser, U. Iben, A comparison of explicit and semi-implicit finite volume schemes for viscous compressible flows in elastic pipes in fast transient regime, Z Angew Math Mech 97 (11) (2017) 1358–1380.

[82] F. Daude, P. Galon, A finite-volume approach for compressible single- and two-phase flows in flexible pipelines with fluid-structure interaction, J. Comput. Phys 362 (2018) 375–408.

[83] J. Lu, G. Wu, L. Zhou, J. Wu, Finite volume method for modeling the load-rejection process of a hydropower plant with an air cushion surge chamber, Water 15 (4) (2023).

[84] R. Zanganeh, E. Jabbari, A. Tijsseling, A. Keramat, Fluid-Structure Interaction in Transient-Based Extended Defect Detection of Pipe Walls, J. Hydraul. Eng. 146 (4) (2020) 04020015. doi:10.1061/(ASCE)HY.1943-7900.0001693.

[85] S. Pal, P. R. Hanmaiahgari, B. W. Karney, An Overview of the Numerical Approaches to Water Hammer Modelling: The Ongoing Quest for Practical and Accurate Numerical Approaches, Water 13 (11) (2021) 1597. doi:10.3390/w13111597.

[86] F. Kerger, P. Archambeau, S. Erpicum, B. J. Dewals, M. Pirotton, An exact riemann solver and a godunov scheme for simulating highly transient mixed flows, J. Comput. Appl. Math. 235 (8) (2011) 2030–2040.

[87] S. Bova, G. Carey, A symmetric formulation and supg scheme for the shallow-water equations, Adv. Water Resour. 19 (3) (1996) 123–131.

[88] A. E. E. Vardy, On sources of damping in water-hammer, Water 15 (3) (2023).

[89] R. Courant, K. O. Friedrichs, Supersonic Flow and Shock Waves, Vol. 21, Springer New York, NY, 1999.

[90] A. F. D'Souza, R. Oldenburger, Dynamic Response of Fluid Lines, J. Basic Eng. 86 (3) (1969) 589–598. doi:10.1115/1.3653180.

[91] E. B. Wylie, V. L. Streeter, L. Suo, Fluid Transients in Systems, Vol. 1, Prentice Hall Englewood Cliffs, NJ, 1993.

[92] K. Urbanowicz, Fast and accurate modelling of frictional transient pipe flow, J. Appl. Math. Mech. 98 (5) (2018) 802–823. doi:10.1002/zamm.201600246.

[93] M. H. Chaudhry, Applied Hydraulic Transients, 3rd Edition, Springer-Verlag, 2014. doi:10.1007/978-1-4614-8538-4.

[94] N. M. C. Martins, B. Brunone, S. Meniconi, H. M. Ramos, D. I. C. Covas, CFD and 1D Approaches for the Unsteady Friction Analysis of Low Reynolds Number Turbulent Flows, J. Hydraul. Eng. 143 (12) (2017) 04017050. doi:10.1061/(ASCE)HY.1943-7900.0001372.

[95] C. C. Mei, H. Jing, Pressure and wall shear stress in blood hammer – Analytical theory, Math. Biosci. 280 (2016) 62–70.

[96] G. O. Brown, The History of the Darcy-Weisbach Equation for Pipe Flow Resistance, in: Environmental and Water Resources History Sessions at ASCE Civil Engineering Conference, 2002, pp. 34–43.

[97] A. E. Vardy, K. Hwang, A characteristics model of transient friction in pipes, J. Hydraul. Res. 29 (5) (1991) 669–684.

[98] A. Bergant, A. Ross Simpson, J. Vìtkovski, Developments in unsteady pipe flow friction modelling, J. Hydraul. Res. 39 (3) (2001) 249–257. doi:10.1080/00221680109499828.

[99] A. Adamkowski, M. Lewandowski, Experimental Examination of Unsteady Friction Models for Transient Pipe Flow Simulation, J. Fluids Eng. Trans. ASME 128 (6) (2006) 1351–1363. doi:10.1115/1.2354521.

[100] J. W. Daily, J. Hankey, R. W. Olive, J. Jordaan, Resistance Coefficients for Accelerated and Decelerated Flows Through Smooth Tubes and Orifices, Tech. rep., MASSACHUSETTS INST OF TECH CAMBRIDGE (1955).

[101] J. P. Vítkovský, A. Bergant, A. R. Simpson, M. F. Lambert, Systematic Evaluation of One-Dimensional Unsteady Friction Models in Simple Pipelines, J. Hydraul. Eng. 132 (7) (2006) 696–708. doi:10.1061/(ASCE)0733-9429(2006)132:7(696).

[102] B. Brunone, U. Golia, M. Greco, Some remarks on the momentum equation for fast transients, in: Proc. Int. Conf. on Hydr. Transients With Water Column Separation, 1991, pp. 201–209.

[103] J. Vitkovsky, M. Lambert, A. Simpson, A. Bergant, Advances in unsteady friction modelling in transient pipe flow, in: 8^{th} Int. Conf. on Pressure Surges, BHR Group, 2000, pp. 471–482.

[104] H. Ramos, D. Covas, A. Borga, D. Loureiro, Surge damping analysis in pipe systems: modelling and experiments, J. Hydraul. Res. 42 (4) (2004) 413–425.

[105] P. Storli, T. K. Nielsen, Transient Friction in Pressurized Pipes. II: Two-Coefficient Instantaneous Acceleration–Based Model, J. Hydraul. Eng. 137 (6) (2011) 679–695. doi:10.1061/(ASCE)HY.1943-7900.0000358.

[106] A. E. Vardy, J. M. B. Brown, Transient, turbulent, smooth pipe friction, J. Hydraul. Res. 33 (4) (1995) 435–456. doi:10.1080/00221689509498654.

[107] E. L. Holmboe, W. T. Rouleau, The Effect of Viscous Shear on Transients in Liquid Lines, J. Basic Eng. 89 (1) (1967) 174–180. doi:10.1115/1.3609549.

[108] W. Zielke, FREQUENCY DEPENDENT FRICTION IN TRANSIENT PIPE FLOW, phdthesis, The University of Michigan (1966).

[109] W. Zielke, Frequency-Dependent Friction in Transient Pipe Flow, J. Basic Eng. 90 (1) (1968) 109–115. doi:10.1115/1.3605049.

[110] D. J. Wood, J. E. Funk, A Boundary-Layer Theory for Transient Viscous Losses in Turbulent Flow, J. Basic Eng. 92 (4) (1970) 865–873. doi:10.1115/1.3425158.

[111] A. S. Tijsseling, Discussion of "effect of boundary on water hammer wave attenuation and shape" by huade cao, ioan nistor, and magdi mohareb, J. Hydraul. Eng. 147 (10) (2021) 07021011.

[112] P. A. Martin, Going round the bend: reflection and transmission of long waves by waveguide corners and labyrinths, Proc. R. Soc. A: Math. Phys. Eng. 479 (2280) (2023).

[113] A. E. Vardy, K. Hwang, A weighting function model of transient turbulent pipe friction, J. Hydraul. Res. 31 (4) (1993) 533–548. doi:10.1080/00221689309498876.

[114] H. Artl, Experimented Untersuchungen uber das instationare, turbulente Reibungsverhalten bei aufgepragten Druckimpulsen in einer Rohrleitung mit kreisquerchnitt (Experimented investigations on the unsteady, turbulent friction behaviour with applied pressure pulses in a circular cross-section pipeline), Tech. rep., Mitteilung Nr 102, Institut fur Wasserbau und Wasserwirtschaft, Technische Universitat Berlin (1993).

[115] J. Laufer, The structure of turbulence in fully developed pipe flow, Tech. rep., NTRS - NASA Technical Reports Server (1953).

[116] M. Ohmi, T. Usui, Pressure and velocity distributions in pulsating turbulent pipe flow part 1 theoretical treatments, Bulletin of JSME 19 (129) (1976) 307–313. doi:10.1299/jsme1958.19.307.

[117] A. E. Vardy, J. M. B. Brown, Transient turbulent friction in smooth pipe flows, J. Sound Vib. 259 (5) (2003) 1011–1036.

[118] J. M. Vardy, M. B. Brown, S. He, C. Ariyaratne, S. Gorji, Applicability of frozen-viscosity models of unsteady wall shear stress, J. Hydraul. Eng. 141 (1) (2015) 04014064.

[119] A. E. Vardy, J. M. B. Brown, Transient turbulent friction in fully rough pipe flows, J. Sound Vib. 270 (1-2) (2004) 233–257.

[120] M. S. Ghidaoui, S. G. S. Mansour, M. Zhao, Applicability of Quasisteady and Axisymmetric Turbulence Models in Water Hammer, J. Hydraul. Eng. 128 (10) (2002) 917–924.

[121] O. Abdeldayem, D. Ferras, S. Zwan, M. Kennedy, Analysis of Unsteady Friction Models Used in Engineering Software for Water Hammer Analysis: Implementation Case in WANDA, Water 13 (4) (2021) 495. doi:10.3390/w13040495.

[122] A. Adamkowski, M. Lewandowski, Unsteady friction modelling in transient pipe flow simulation, Transactions of the Institute of Fluid-Flow Machinery 115 (2004) 83–97.

[123] H. F. Duan, S. Meniconi, P. J. Lee, B. Brunone, M. S. Ghidaoui, Local and Integral Energy-Based Evaluation for the Unsteady Friction Relevance in Transient Pipe Flows, J. Hydraul. Eng. 143 (7) (2017) 04017015. doi:10.1061/(ASCE)HY.1943-7900.0001304.

[124] A. Ferrari, O. Vento, Influence of Frequency-Dependent Friction Modeling on the Simulation of Transient Flows in High-Pressure Flow Pipelines, J. Fluids. Eng. 142 (8) (2020) 081205. doi:10.1115/1.4046623.

[125] P. Flaud, D. Geiger, C. Oddou, D. Quemada, Ecoulements pulsés dans les tuyaux visco-élastiques. application à l'étude de la circulation sanguine., J. de Physique 35 (1974) 869–882.

[126] S. Čanić, C. J. Hartley, D. Rosenstrauch, J. Tambaca, G. Guidoboni, A. Mikelić, Blood Flow in Compliant Arteries: An Effective Viscoelastic Reduced Model, Numerics, and Experimental Validation, Annu. Rev. Biomed. Eng 34 (4) (2006) 575–592.

[127] D. Bessems, C. Giannopapa, M. Rutten, F. Van De Vosse, Experimental validation of a time-domain-based wave propagation model of blood flow in viscoelastic vessels, J. Biomech. 41 (2) (2008) 284–291.

[128] N. Duraiswamy, R. T. Schoephoerster, M. R. Moreno, J. E. Moore, Jr., Stented artery flow patterns and their effects on the artery wall, Annu. Rev. Fluid Mech 39 (2007) 357–382.

[129] E. Rieutord, A. Blanchard, Influence d'un comportement viscoélastique de la conduite dans le phénomène du coup de bélier, C. R. Acad. Sci. Ser. 274 (1972) 1963–1966.

[130] M. Gally, M. Güney, E. Rieutord, An investigation of pressure transients in viscoelastic pipes, J. Fluids Eng. 101 (4) (1979) 495–499.

[131] E. Rieutord, A. Blanchard, Pulsating viscoelastic pipe flow - water-hammer, J. Hydraul. Res. 17 (3) (1979) 217–229.

[132] R. P. Sawatzky, M. B., On the propagation of pressure pulses through a viscous fluid contained in a visco-elastic tube, Q. J. Mech. Apppl. Math. 41 (1) (1988) 33–50.

[133] L. Suo, E. B. Wylie, Complex Wavespeed and Hydraulic Transients in Viscoelastic Pipes, J. Fluids. Eng. 112 (4) (1990) 496–500.

[134] N. Kizilova, Pressure Wave Propagation in Liquid-Filled Tubes of Viscoelastic Material, Fluid Dyn. 41 (2006) 434–446.

[135] A. Bayle, F. Rein, F. Plouraboué, Frequency varying rheology-based fluid-structure-interactions waves in liquid-filled visco-elastic pipes, J. Sound Vib. 562 (2023).

[136] B. Bahrar, E. Rieutord, R. Morel, Influence de la viscoélasticité de la paroi sur les phénomènes classiques de coup de bélier, Houille blanche 1 (3) (1998) 26.

[137] D. Covas, I. Stoianov, H. Ramos, N. Graham, C. Maksimovic, The dynamic effect of pipe-wall viscoelasticity in hydraulic transients. Part I Experimental analysis and creep characterization, J. Hydraul. Res. 42 (2004) 517–532.

[138] K. Weinerowska-Bords, Viscoelastic Model of Waterhammer in Single Pipeline–Problems and Questions, Arch. Hydroengineering Environ. Mech. 53 (4) (2006) 331–351.

[139] A. K. Soares, D. Covas, L. F. Reis, Analysis of PVC Pipe-Wall Viscoelasticity during Water Hammer, J. Hydraul. Eng. 134 (9) (2008) 1389–1394.

[140] S. Meniconi, B. Brunone, M. Ferrante, Water-hammer pressure waves interaction at cross-section changes in series in viscoelastic pipes, J. Fluids Struct. 33 (2012) 44–58. doi:10.1016/j.jfluidstructs.2012.05.007.

[141] K. Urbanowicz, M. Firkowski, Z. Zarzycki, Modelling water hammer in viscoelastic pipelines: short brief, J. Phys. Conf. Ser. 760 (2016) 012037.

[142] K. Urbanowicz, D. Huan-Feng, A. Bergant, Transient flow of liquid in plastic pipes, J. Mech. Eng. Res. 66 (2) (2020) 77–90.

[143] Z. Duan, T. Li, Comprehensive application analyses of elastic models and viscoelastic models in transient flows in polymeric pipelines, J. Hydroinformatics 24 (5) (2022) 1020–1052.

[144] K. Weinerowska-Bords, Alternative approach to convolution term of viscoelasticity in equations of unsteady pipe flow, J. Fluids Eng. 137 (5) (2015) 054501.

[145] A. Keramat, A. Tijsseling, Q. Hou, A. Ahmadi, Fluid–structure interaction with pipe-wall viscoelasticity during water hammer, J. Fluids Struct. 28 (2011) 434–455.

[146] R. S. Hosseini, A. Ahmadi, R. Zanganeh, Fluid-structure interaction during water hammer in a pipeline with different performance mechanisms of viscoelastic supports, J. Sound Vib. 487 (2020) 115527.

[147] D. A. Monteiro, R. Freitas, F. Bastos, A. Tijsseling, Fluid transients in viscoelastic pipes via an internal variable constitutive theory, Appl. Math 114 (2023) 846–869.

[148] M. T. Shaw, W. J. MacKnight, Introduction to polymer viscoelasticity, 4^{th} edition, John Wiley & Sons, 2018.

[149] D. Covas, I. Stoianov, H. Ramos, N. G., C. Maksimović, D. Butler, Water hammer in pressurized polyethylene pipes: conceptual model and experimental analysis, Urban Water J. 1 (2) (2004) 177–197.

[150] M. Mitosek, M. Chorzelski, Influence of visco-elasticity on pressure wave velocity in polyethylene MDPE pipe, Arch. Hydroengineering Environ. Mech. 50 (2003) 127–140.

[151] J. Lemaitre, Introduction to Elasticity and Viscoelasticity, Handbook of Materials Behavior Models, Elsevier, 2001, Ch. 2.1, pp. 71–74.

[152] J. M. Carcione, F. Poletto, D. Gei, 3-D wave simulation in anelastic media using the Kelvin–Voigt constitutive equation, J. Comput. Phys. 196 (1) (2004) 282–297.

[153] A. Eringen, Mechanics of Continua, R. E. Krieger Publishing Company, 1980.

[154] D. Bland, The Theory of Linear Viscoelasticity, Dover Books on Physics, Dover Publications, 2016.

[155] D. Annie, On a Theory of Thermoviscoelastic Materials with Voids, J. Elast. 104 (2011) 369–384.

[156] J. Sharma, M. I. Othman, Effect of rotation on generalized thermo-viscoelastic Rayleigh–Lamb waves, Int. J. Solids Struct. 44 (13) (2007) 4243–4255.

[157] F. Barez, W. Goldsmith, J. L. Sackman, Longitudinal waves in liquid-filled tubes—I: Theory, Int. J. Mech. Sci. 21 (4) (1979) 213–221.

[158] M. Prek, Analysis of wave propagation in fluid-filled viscoelastic pipes, Mech. Syst. Signal Process. 21 (2007) 1907–1916.

[159] E. Yao, G. Kember, D. Hansen, Analysis of water hammer attenuation in the Brunone model of unsteady friction, Quart. Appl. Math. 72 (2) (2014) 281–290. doi:10.1090/S0033-569X-2014-01354-6.

[160] E. Yao, G. Kember, D. Hansen, Water Hammer Analysis and Parameter Estimation in Polymer Pipes with Weak Strain-Rate Feedback, J. Eng. Mech. 142 (8) (2016) 04016052. doi:10.1061/(ASCE)EM.1943-7889.0001104.

[161] M. Zhao, M. S. Ghidaoui, A. A. Kolyshkin, Perturbation dynamics in unsteady pipe flows, J. Fluid Mech. 570 (2007) 129–154.

[162] A. Corli, I. Gasser, M. Lukáčová-Medvid'ová, A. Roggensack, U. Teschke, A multiscale approach to liquid flows in pipes I: The single pipe, Appl. Math. Comput. 219 (3) (2012) 856–874. doi:10.1016/j.amc.2012.06.054.

[163] C. C. Mei, H. Jing, Effects of thin plaque on blood hammer - an asymptotic theory, Eur. J. Mech. B Fluids 69 (2018) 62–75.

[164] J. Lighthill, WAVES IN FLUIDS, Cambridge university press, 2001.

[165] F. Gaultier, J. Gilbert, J. Dalmont, R. Picó, Wave propagation in a fluid filled rubber tube: Theoretical and experimental results for Korteweg's wave, Acta Acust. United Ac. 93 (2007) 333–344.

[166] J. S. Walker, J. W. Phillips, Pulse Propagation in Fluid-Filled Tubes, J. Appl. Mech. 44 (1) (1977) 31–35. doi:10.1115/1.3424009.

[167] M. H. Chaudhry, Applied Hydraulic Transients, 3rd Edition, Springer-Verlag, 2014. doi:10.1007/978-1-4614-8538-4.

[168] P. Puntorieri, G. Barbaro, N. Martins, D. Covas, V. Fiamma, Hydraulic Transient Experimental Study in a Copper Pipe, in: Proceedings of the Multiphase Flow 2017, 2017, pp. 27–33. doi:10.2495/MPF170041.

[169] S. Kim, Hydraulic transient evaluation via fabricable impedance matrix for pipe networks, J. Hydraul. Res. 60 (2) (2022) 326–340.

[170] S. Kim, Impedance matrix method for transient analysis of complicated pipe networks, J. Hydraul. Res. 45 (6) (2007) 818–828.

[171] A. C. Zecchin, A. R. Simpson, M. F. Lambert, L. B. White, J. P. Vitkovsky, Transient modeling of arbitrary pipe networks by a laplace-domain admittance matrix, J. Eng. Mech. 135 (6) (2009) 538–547.

[172] F. Brown, The transient response of fluid lines, J. Basic Eng. 84 (3) (1962) 547–553.

[173] J. S. Stecki, D. C. Davis, Fluid transmission-lines distributed parameter models. 1. a review of the state-of-the-art. part a, Proc. Inst. Mech. Eng. 200 (4) (1986) 215–228.

[174] A. C. Zecchin, M. F. Lambert, A. R. Simpson, L. B. White, Frequency-domain modeling of transients in pipe networks with compound nodes using a laplace-domain admittance matrix, J. Hydraul. Eng. 136 (10) (2010) 739–755.

[175] A. C. Zecchin, M. F. Lambert, A. R. Simpson, Inverse laplace transform for transient-state fluid line network simulation, J. Eng. Mech. 138 (1) (2012) 101.

[176] A. Zecchin, Laplace-Domain Analysis of Fluid Line Netwoks with Applications to Time-Domain Simulation and System Parameter Identification, Ph.D. thesis, University of Adelaide (2010).

[177] C. Capponi, M. Ferrante, A. C. Zecchin, J. Gong, Experimental validation of the admittance matrix method on a Y-system, J. Hydraul. Res. 56 (4) (2018) 439–450. doi:10.1080/00221686.2017.1372818.

[178] S. Yalouz, V. Pouthier, C. Falvo, Exciton-phonon dynamics on complex networks: Comparison between a perturbative approach and exact calculations, Phys. Rev. E 96 (2) (2017).

[179] T. Kottos, U. Smilansky, Quantum chaos on graphs, Phys. Rev. Lett. 79 (1997) 4794–4797.

[180] Y. Dabaghian, Periodic orbit theory and the statistical analysis of scaling quantum graph spectra, Phys. Rev. E. 75 (5, 2) (2007).

[181] U. Smilansky, Delay-time distribution in the scattering of time-narrow wave packets. (i), J. Phys. A Math. Theor. 50 (21) (2017) 215301.

[182] U. Smilansky, H. Schanz, Delay-time distribution in the scattering of time-narrow wave packets (ii)-quantum graphs, J. Phys. A Math. Theor. 51 (7) (2018).

[183] S. Gnutzmann, D. Waltner, Stationary waves on nonlinear quantum graphs: General framework and canonical perturbation theory, Phys. Rev. E. 93 (3) (2016).

[184] M. Brio, J. G. Caputo, H. Kratitz, Spectral solutions of pde's on networks, Applied Numerical Mathematics 172 (2022) 99–117.

[185] F. Plouraboué, Quantum graph waves external triggering : energy transfer and damping, Phys. Rev. E 109 (5) (2024) 054310.

[186] P. Kuchment, Quantum graphs: I. some basic structures, Waves Random Complex Media 14 (1) (2004) S107–S128.

[187] G. Berkolaiko, P. Kuchment, Dependence of the spectrum of a quantum graph on vertex conditions and edge length, in: Spectral Geometry Proceedings of Symposia in Pure Mathematics, NordiCHI, American Mathematical Society, Providence, 2017, pp. 117–139.

[188] G. Berkolaiko, J. B. Kennedy, P. Kurasov, D. Mugnolo, Surgery principles for the spectral analysis of quantum graphs, Trans Am Math Soc 372 (7) (2019) 5153–5197.

[189] A. Kairzhan, D. Noja, D. E. Pelinovsky, Standing waves on quantum graphs, J. Phys. A: Math. Theor 55 (24) (2022).

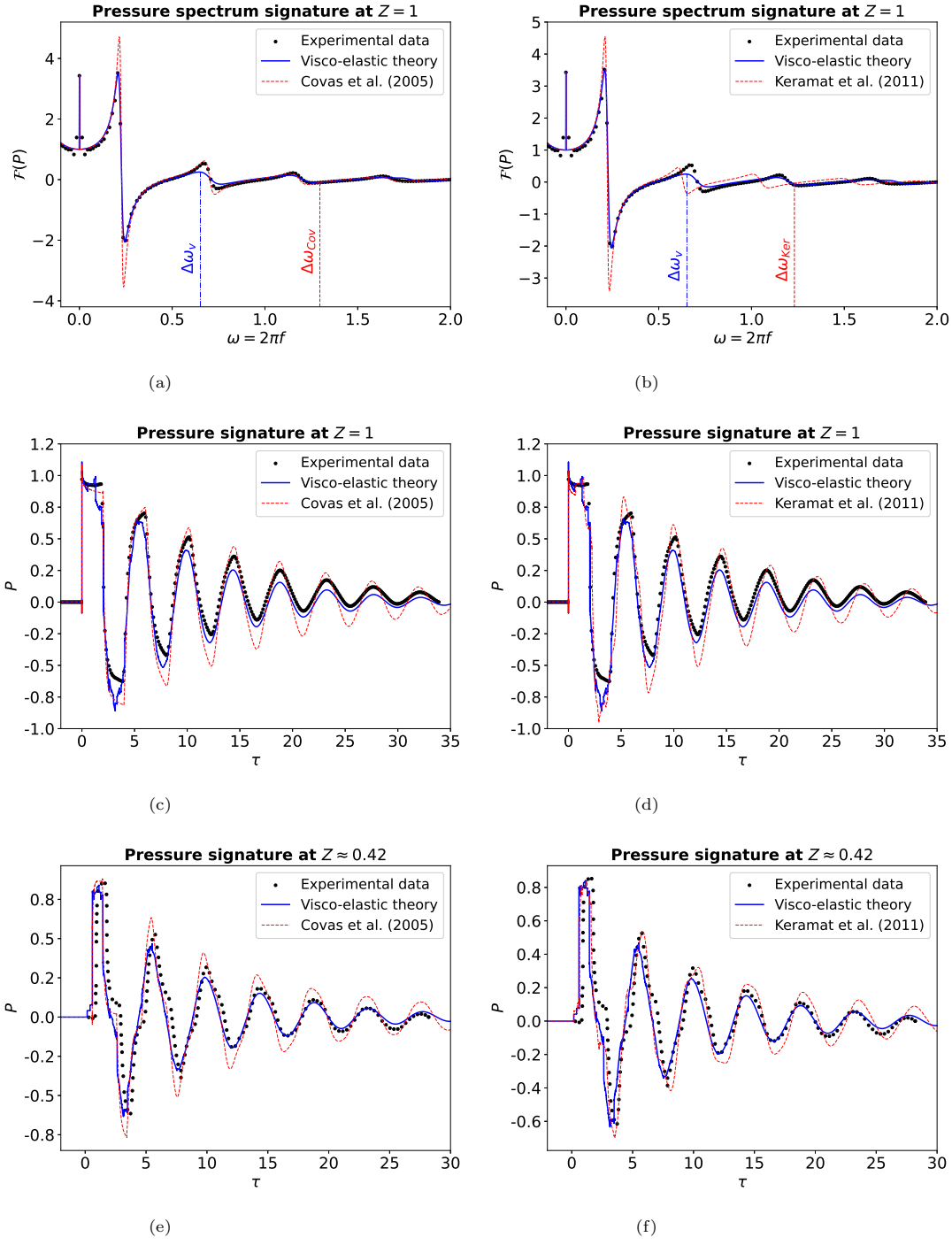

Figure 13: Comparison between the rheology-based model of [65] (referred to as "Visco-elastic theory") and [31] and [145] ones for the pressure signal at various location for the reservoir-pipe-anchored valve configuration. Dimensionless pulsation $\omega = \omega^* L^*/c^*_{p,T}$ using (35) have been used in (a) and (b), dimensionless time $\tau = t^* c^*_{p,T}/L^*$ in (c), (d), (e) and (f).

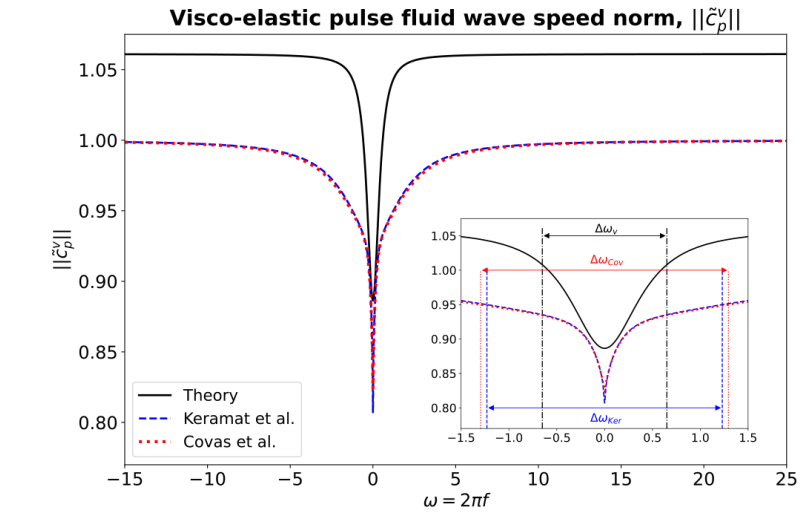

(a)

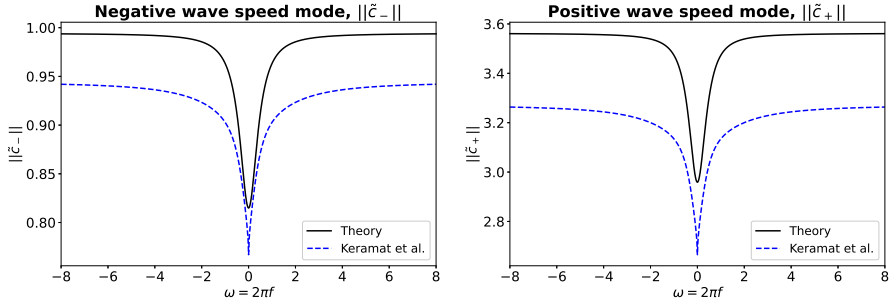

(b) (c)

Figure 14: Comparison of frequency domain dependence of dimensionless visco-elastic velocities obtained from fitting parameters to the experimental data of [137, 31]. (a) $\tilde{c}_p^v(\omega)$ (153), (b) $\tilde{c}_+$ (154), (c) $\tilde{c}_-$ (154). Dimensionless pulsation $\omega = \omega^* L^*/c_{p,T}^*$ have been used.

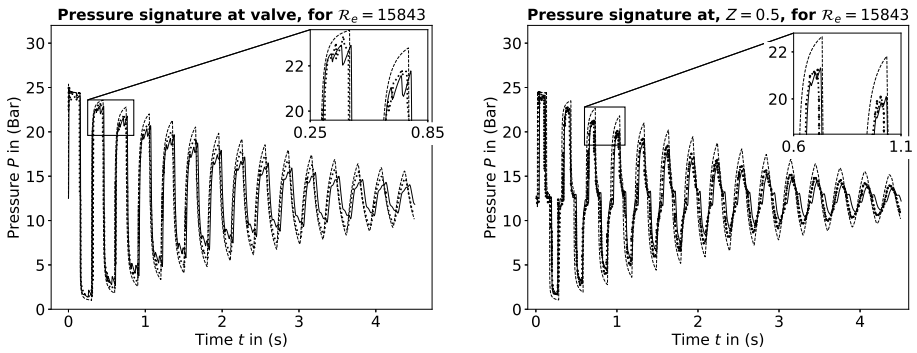

(a) (b)

Figure 15: Pressure signature compared with experimental data of ([99]). Experimental data are depicted with black dotted lines while theoretical results from [65] are depicted with continuous lines. ([95])'s solution (no-FSI) is provided with dashed line. Dimensionless numbers are $\mathcal{M} = 7.2 \cdot 10^{-4}$, $\epsilon = 8.2 \cdot 10^{-5}$, $\alpha = 0.125$, $\delta = 3.3 \cdot 10^{-2}$ and $\mathcal{D} = 0.11$.

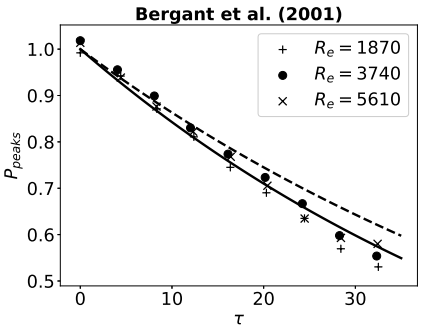

(a) $\mathcal{M} = [7.65^{(+)}, 15.3^{(\bullet)}, 23^{(\times)}] \cdot 10^{-5}$, $\epsilon = 3 \cdot 10^{-4}$, $\alpha = 0.146$, $\delta = 1.7 \cdot 10^{-2}$

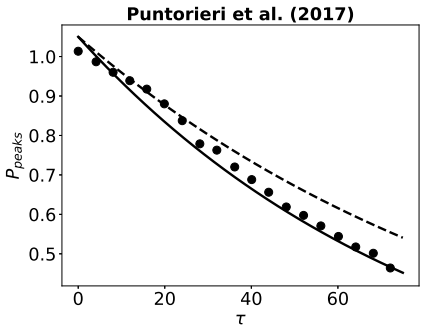

(b) $\mathcal{M} = 1.53 \cdot 10^{-4}$, $\epsilon = 6.57 \cdot 10^{-4}$, $\alpha = 0.1$, $\delta = 1.1 \cdot 10^{-2}$

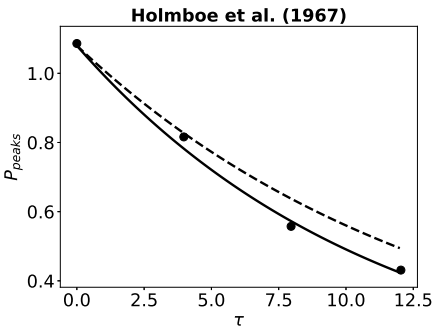

(c) $\mathcal{M} = 1.88 \cdot 10^{-4}$, $\epsilon = 3.5 \cdot 10^{-4}$, $\alpha = 0.13$, $\delta = 8.2 \cdot 10^{-2}$

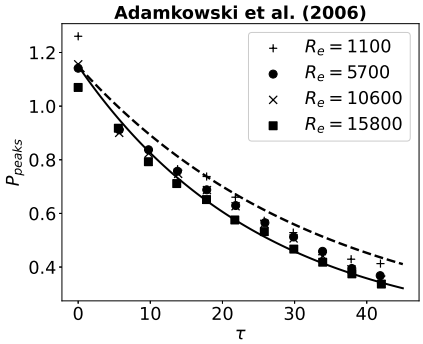

(d) $\mathcal{M} = [5.05^{(+)}, 26.0^{(\bullet)}, 48.3^{(\times)}, 72.0^{(\blacksquare)}] \cdot 10^{-5}$, $\epsilon = 8.2 \cdot 10^{-5}$, $\alpha = 0.125$, $\delta = 3.3 \cdot 10^{-2}$

Figure 16: First exponential damping mode comparison with experimental dimensionless pressure peaks, P_{peaks}. The present theory is depicted with a continuous line while ([95])'s theory ($\nu_s \to 0$) is depicted by a dashed line.

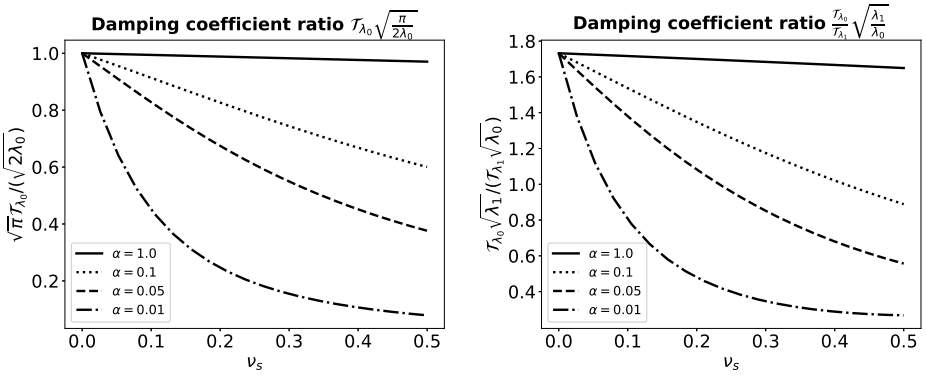

(a) (b)

Figure 17: Exponential damping coefficient analysis: (a) Analysis of $\mathcal{T}_0\sqrt{\frac{\pi}{2\lambda_0}}$, (b) Analysis of $\frac{\mathcal{T}_0}{\mathcal{T}_1}\sqrt{\frac{\lambda_1}{\lambda_0}}$. Iso–$\alpha$ lines are represented based on ([99])'s data from Table 2.

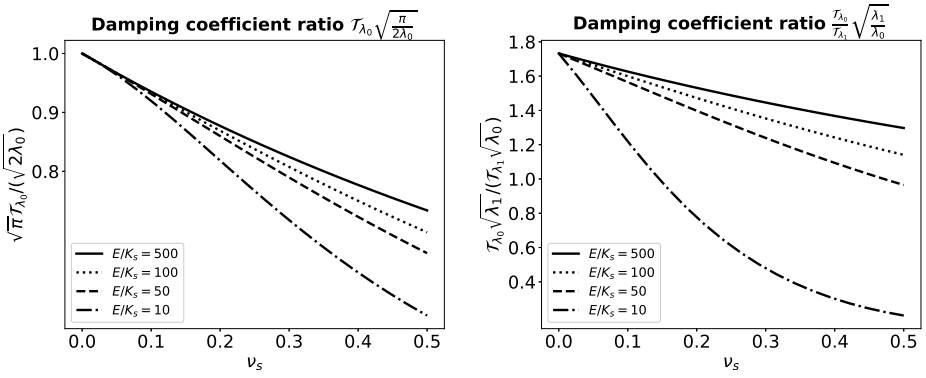

(a) (b)

Figure 18: Exponential damping coefficient analysis: (a) Analysis of $\mathcal{T}_0\sqrt{\frac{\pi}{2\lambda_0}}$, (b) Analysis of $\frac{\mathcal{T}_0}{\mathcal{T}_1}\sqrt{\frac{\lambda_1}{\lambda_0}}$. Iso–$E$ lines are represented based on ([99])'s data from Table 2.

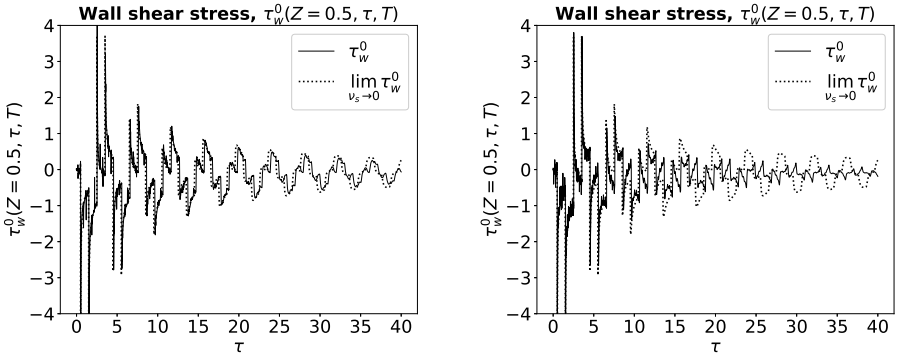

(a) $\alpha = 0.125$, $\mathcal{D} = 0.11$

(b) $\alpha = 0.125$, $\mathcal{D} = 1$

Figure 19: Dimensionless fluid wall shear stress τ_w^0 at middle's pipe location. ([99])'s data from Table 2 are used with (a) $\mathcal{D} = 0.11$, (b)$\mathcal{D} = 1$.

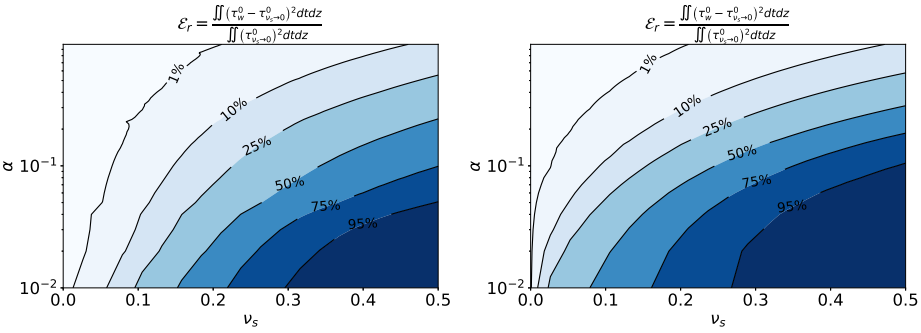

(a) $\mathcal{D} = 0.11$

(b) $\mathcal{D} = 1$

Figure 20: Relative difference $\mathcal{E}_r$ between (FSI) and no–(FSI) ($\nu_s \to 0$) fluid wall shear rate. ([99])'s data from Table 2 are used with (a) density ratio $\mathcal{D} = 0.11$, (b) $\mathcal{D} = 1$.

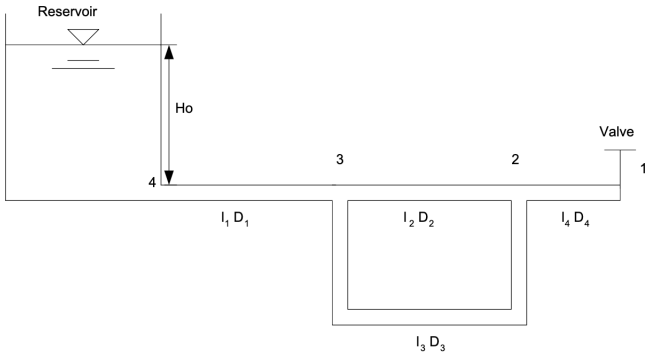

$$\begin{bmatrix} Z_{c2}\sinh\gamma_2 l_2 & 0 & 0 & 0 & 1 & 0 \\ \cosh\gamma_2 l_2 & 0 & -1 & 0 & 0 & 0 \\ 0 & Z_{c3}\sinh\gamma_3 l_3 & 0 & 0 & 1 & 0 \\ 0 & \cosh\gamma_3 l_3 & 0 & -1 & 0 & 0 \\ 1 & 1 & 0 & 0 & 0 & 0 \\ 0 & 0 & 1 & 1 & 0 & -1 \end{bmatrix} \cdot \begin{bmatrix} Q_{3l_2}/Q_{3l_1} \\ Q_{3l_3}/Q_{3l_1} \\ Q_{2l_2}/Q_{3l_1} \\ Q_{2l_3}/Q_{3l_1} \\ H_2/Q_{3l_1} \\ Q_{2l_4}/Q_{3l_1} \end{bmatrix} = \begin{bmatrix} Z_3\cosh\gamma_2 l_2 \\ Z_3\sinh\gamma_2 l_2/Z_{c2} \\ Z_3\cosh\gamma_3 l_3 \\ Z_3\sinh\gamma_3 l_3/Z_{c3} \\ 1 \\ 0 \end{bmatrix}$$

Figure 21: Hydraulic looped network and its associated network admittance linear system studied by S. Kim [170].

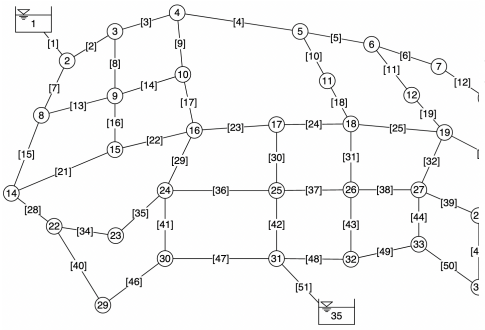

(a) 51-pipes test network studied by Zechin et al.[175]

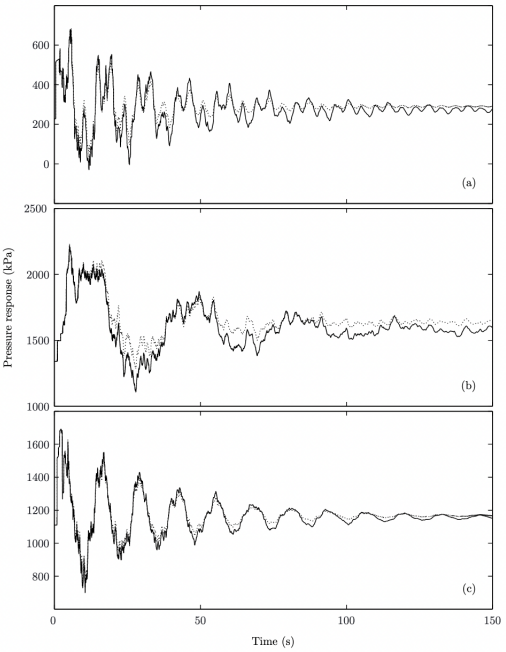

(b) Example of pressure signature for the (NILT) method, in dotted line, compared with the Method Of Characteristic (MOC) predictions, in continuous lines.

Figure 22: Investigation of the pressure dynamic within a complex network using the numerical inverse Laplace transform (NILT) procedure from Zechin et al. [176, 175]

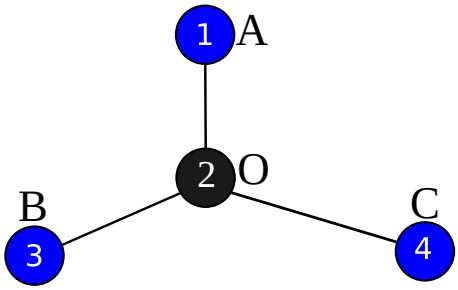

Figure 23: 3-star metric graph having length $\ell_{21} = 2.211$, $\ell_{23} = 3.111$ and $\ell_{24} = 4.711$.

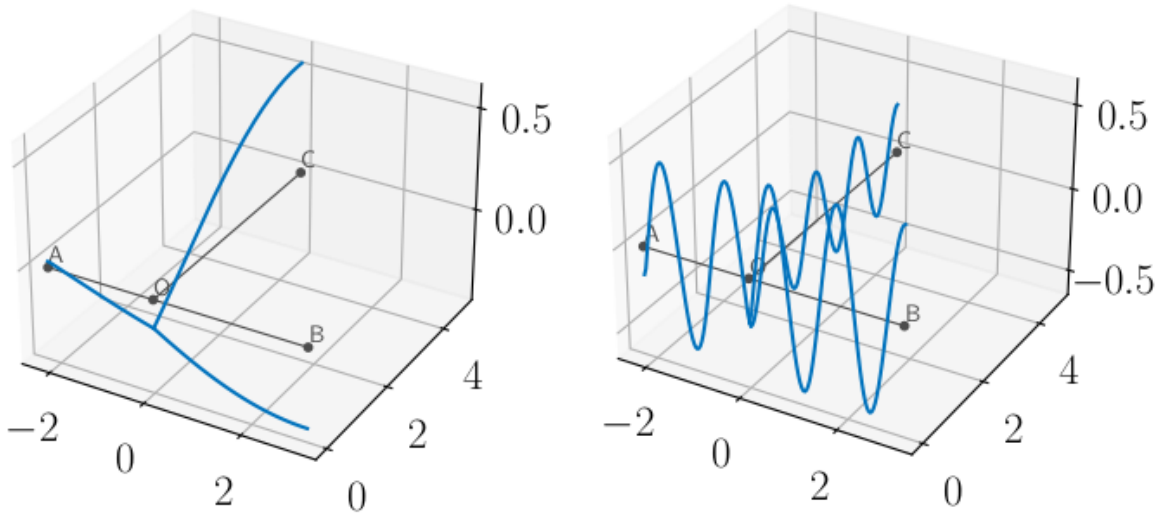

(a) Kirchhoff mode $\mathbf{\Psi}_{\lambda_1}$.

(b) Kirchhoff mode $\mathbf{\Psi}_{\lambda_2}$.

Figure 24: First two Kirchhoff eigenmode of the 3-star graph 23.